

“A memory of RPS25 loss drives resistance phenotypes”

Authors

Alex G. Johnson^{1,2}, Ryan A. Flynn³, Christopher P. Lapointe¹, Yaw Shin Ooi⁴, Michael L. Zhao², Shizuka B. Yamada⁵, Julien Couthouis⁵, Aaron D. Gitler⁵, Jan E. Carette⁴, and Joseph D. Puglisi¹

Affiliations

¹ Department of Structural Biology, Stanford University School of Medicine, Stanford, CA 94305

² Department of Chemical and Systems Biology, Stanford University School of Medicine, Stanford, CA 94305

³ Department of Chemistry, Stanford University, Stanford, CA 94305

⁴ Department of Microbiology & Immunology, Stanford University, Stanford, CA 94305

⁵ Department of Genetics, Stanford University, Stanford, CA 94305

Correspondence: algejohn@stanford.edu, puglisi@stanford.edu

Abstract

In order to maintain cellular protein homeostasis, ribosomes are safeguarded against dysregulation by myriad processes. Remarkably, many cell types can withstand the genetic disruption of numerous ribosomal protein genes, indicating that select ribosome variants can sustain cellular life. Genetic alterations of ribosomal protein genes have been further linked to diverse cellular phenotypes and human disease, yet the direct and indirect consequences of sustained alterations in ribosomal protein levels are poorly understood. To address this knowledge gap, we studied *in vitro* and cellular consequences that follow genetic knockout of the small subunit ribosomal proteins RPS25 or RACK1 in a human haploid cell line. To our surprise, we found that multiple cellular phenotypes previously assumed to result from a direct effect on translation were instead caused by indirect effects. During characterization of ribosomes isolated from the RPS25 knockout cell line, we discovered a partial remodeling of the large subunit via the ribosomal protein paralog eL22L1. Upon further examination, we found that RPS25 knockout clones display irreversible rewiring of viral- and toxin-resistance phenotypes, suggesting that the cells had undergone a stable transition to a new cell state. This new state appears to drive pleiotropic phenotypes and is characterized by a dramatically altered transcriptome and membrane proteome. By homology-directed repair of a RPS25 knockout cell line, we demonstrate that even when RPS25 expression is rescued at the native genomic locus, cells fail to correct for the phenotypic hysteresis. Our results illustrate how the elasticity of cells to a ribosome perturbation can manifest as specific but indirect phenotypic outcomes.

INTRODUCTION

The eukaryotic ribosome is comprised of four strands of rRNA and ~80 ribosomal proteins (RPs), most of which are essential for life. To ensure accurate and efficient protein synthesis, cells have evolved numerous measures to control and protect the cellular ribosome pool. The existence of genetic knockouts of select RPs in yeast and human cell lines nevertheless indicates that cells are elastic to severe ribosome compositional alterations (Blomen et al., 2015; Steffen et al., 2012). The presence of ribosomes with substoichiometric RP levels in unperturbed cells further suggests the possibility that certain alterations might represent direct, regulated control of protein synthesis by RPs (Shi et al., 2017; Van De Waterbeemd et al., 2018). However, just as compositional heterogeneity might be a product of functional selection, it could also represent ribosomes that have escaped from imperfect cellular quality control measures. While not eliciting cell death, the latter alteration might be sensed by the cell and lead to a host of indirect outcomes. Thus, RP loss or disruption may be expected to drive either or both direct effects on translation and indirect effects as cells sense and adapt to ribosome irregularities. While genetic RP loss is linked to numerous cellular phenotypic changes and human disease, the mechanistic basis by which these alterations arise remains unclear (McCann and Baserga, 2013).

For RP composition of the ribosome to control protein synthesis directly, specific molecular interactions between ribosome-bound RPs and mRNA transcripts could occur, such that RP levels would select or filter for the translation of certain transcripts (Gilbert, 2011; Mauro and Edelman, 2002; Xue and Barna, 2012). Additionally, the presence or absence of a RP on the ribosome could allosterically interfere with a conformational change or otherwise alter interactions with ribosome-associated factors to drive mRNA specificity. Although physically indirect, we will here define these allosteric effects as direct since they act at the level of translation, rather than through another cellular process. RP-mediated selection of mRNAs could occur early in the initiation phase, by directly affecting ribosome recruitment, or otherwise alter the translation efficiency of specific transcripts at later steps. To study the direct effects of RPs on protein synthesis, our laboratory has previously leveraged the non-essentiality of two RPs, RPS25 and RACK1, to engineer human ribosomes for biophysical measurements (Fuchs et al., 2015; Johnson et al., 2019). An added benefit was that these proteins are non-essential for ribosomal RNA (rRNA) maturation and proximal to ribosome-bound viral RNAs in cryo-EM-based models (**Figure 1A** and **Figure 1—FigS1F-G**) (Larburu et al., 2016; O'Donohue et al., 2010; Robledo et al., 2008). Henceforth we use the term eS25 (by the modern RP nomenclature (Ban et al., 2014)) to describe the protein product of the human RPS25 gene, while the RACK1 protein and gene names are the same. Given the association of these proteins with diverse translational processes and cellular phenotypes, we became intrigued by the biochemical basis for these RP's effects on translation and sought to apply our cellular and biophysical tools to the problem.

RPS25 is the sole RP for which *in vitro* and *in vivo* experiments converge to support a ribosome filtering model in at least one case. Yeast ribosomes lacking eS25 have reduced affinity *in vitro* for the Cricket paralysis virus intergenomic region internal ribosome entry site (CrPV IGR IRES) RNA, and the cells from which these ribosomes are isolated have strongly reduced translational reporter activity *in vivo* (Landry et al., 2009; Muhs et al., 2011). These results are explained by structural analyses of CrPV IGR IRES-ribosome complexes, wherein eS25 forms direct interactions with the viral RNA near the E site region of the ribosome (Fernández et al., 2014; Nishiyama et al., 2007; Pisareva et al., 2018) (**Figure 1A**, left panel). eS25 also directly contacts the Hepatitis C virus (HCV) IRES RNA within ribosome-IRES complexes (**Figure 1A**, right panel), and reporter assays concluded that eS25 is also required for this IRES to function in HeLa cells (Landry et al., 2009). Further studies have broadly linked eS25 to the mechanism of other IRESs and specialized translation initiation events (Hertz et al., 2013; Shi et al., 2016), and the recent observation that eS25 is substoichiometric in cellular ribosomes suggests that eS25-mediated translational control could be physiologically relevant (Shi et al., 2017).

Receptor for Activated C kinase 1 (RACK1) is another eukaryote-specific RP that is implicated in diverse translational and cell signaling processes. RACK1 was first isolated based on interactions with protein kinase C (PKC) and subsequent studies defined it as a ribosome “scaffold” for numerous other signaling proteins (Nielsen et al., 2017). More recently, RACK1 has been implicated in translational

processes including ribosome-associated quality control, reading frame maintenance, and IRES-mediated translation (Juszkiewicz and Hegde, 2017; Majzoub et al., 2014; Sundaramoorthy et al., 2017; Wang et al., 2018). The effects of RACK1 and RPS25 on signaling and translation have been mainly inferred from depletion experiments using siRNA knockdowns or genetic knockouts in yeast or human cells. Like eS25, reduction in cellular levels of RACK1 interferes with HCV IRES-mediated translation (Majzoub et al., 2014), but RACK1 does not form direct interactions with IRES RNAs on the ribosome or control ribosome recruitment *in vitro* (Johnson et al., 2019). In contrast to eS25, RACK1 is stoichiometric on most cellular ribosomes and currently very little biochemical data directly links RACK1 composition on the ribosome to a mRNA selection step, though a recent *in vitro* analysis of yeast ribosomes lacking the yeast homolog Asc1p observed a defect in elongation (Tesina et al., 2019).

The targeted disruption of cellular RP levels is perhaps the most accessible and rapid technique to examine RP function, yet such techniques come with limitations. Chief among them is the inability of the assays to distinguish direct versus indirect effects. Both partial knockdown or full genetic knockout is expected to cause immediate, direct effects on translation and long-term, indirect consequences on cell biology. In the former case, immediate effects might be obscured by the long lifetime of the ribosome (half-life of 5-7 days) and/or coordinated changes in overall ribosome levels in response to the loss of single RPs (Cheng et al., 2019; Dice and Schimke, 1972; Khajuria et al., 2018; Mills and Green, 2017). Certain direct effects may be preserved in genetic knockouts, where there is a wealth of data from genome-wide screens, but they may also become muted due to cellular adaptation. The potential mechanisms for adaptation to RP loss are vast and might include things such as the activated expression of a paralog gene, altered chaperone levels and degradation pathways to correct for proteotoxic challenges, or the remodeling of entire cellular compartments. Further, alterations in ribosome biogenesis may lead to the well-documented p53 stabilization by orphan RPs and MDM2 in mammals (Liu et al., 2016), but as shown by studies in yeast (which lack p53), may arise through other sources (Tye et al., 2019). The adaptation itself, rather than the RP's normal function, could foreseeably lead to phenotypes that arise in genetic screens, thereby resulting in false positives. Additionally, though knockdown experiments may be timed to minimize indirect effects from cellular adaptation, some effects may be unavoidable, and there is a lack of simple methods for performing the crucial rescue experiments enabled by genetic KOs. Thus, many types of properly controlled experiments are necessary to distinguish the short-term causes and long-term consequences of RP deficiency.

Here, we describe a series of experiments characterizing the direct and indirect effects that follow RP loss in a haploid human cell line. With the aim of analyzing direct effects, we commenced with biochemical and compositional analysis of ribosomes isolated from RPS25 or RACK1 KO cells. Prompted in part by the unexpected observation of an independent ribosome remodeling event, we turned our focus towards cellular analysis. We found that loss of RPS25 or RACK1 leads to partially overlapping, yet distinct sets of phenotypic outcomes. While reintroduction of the RACK1 cDNA in the a RACK1 KO rescues phenotypes, several phenotypes resulting from RPS25 loss were irreversible. Collectively, our findings uncover a host of indirect effects that may accompany RP loss and have implications for the mechanistic interpretation of genetic alterations in the translational apparatus.

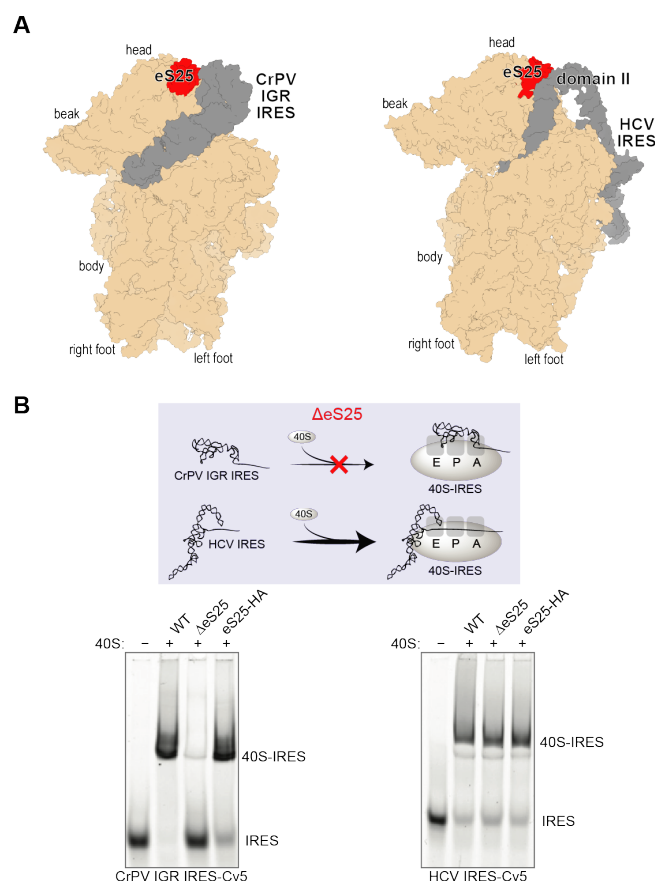
RESULTS

eS25 mediates direct 40S recruitment to the CrPV IGR IRES but not the HCV IRES.

We first sought to recapitulate in a human system the prior results from studies in yeast that demonstrated the *in vitro* requirement of eS25 for efficient ribosome recruitment to the CrPV IGR IRES (Landry et al., 2009; Muhs et al., 2011). We purified human 40S and 60S ribosomal subunits from wild type (WT) and RPS25 knockout (KO) HAP1 cells (Fuchs et al., 2015), and *in vitro* transcribed and fluorescently labeled CrPV IRES and HCV IRES RNAs (Johnson et al., 2019). To make an addback (AB) cell line, RPS25 KO cells were transduced with lentivirus to express a C-terminally HA-tagged RPS25 cDNA (RPS25-HA), and these cells were used for ribosome purifications. The incorporation of the tagged protein (eS25-HA) into polysomes and purified ribosomal subunits was confirmed by immunoblotting (**Figure 1—FigS1A-B**).

We next determined the relative affinities of CrPV IRES to the different 40S subunits using native gel analysis (**Figure 1—FigS1C**). Human eS25-deficient (Δ eS25) ribosomes had decreased affinity to the IRES, as shown in yeast (Landry et al., 2009), and affinity was recovered in eS25-HA AB 40S subunits (**Figure 1B**). In contrast, the HCV IRES, an IRES that is inactive in yeast and therefore not previously tested, showed no dependency on eS25 for ribosome recruitment (**Figure 1B** and **Figure 1—FigS1D**). Moreover, eS25 did not affect magnesium-driven 80S complex formation on the HCV IRES (**Figure 1—FigS1E**) (Lancaster et al., 2006), suggesting that the previously-reported requirement on eS25 by the HCV IRES might occur at a different step (Landry et al., 2009). The lack of eS25-dependence on 40S recruitment to the HCV IRES is perhaps unsurprising given that eS25 makes direct contacts with domain II of the IRES—a domain that when removed reduces IRES activity without affecting ribosome affinity (Otto and Puglisi, 2004). This result is further in line with our previous observations with Δ RACK1 ribosomes, which showed no deficiency in recruitment to the HCV IRES (Johnson et al., 2019).

Figure 1 (half page width). Loss of eS25 impairs direct 40S recruitment to the CrPV IGR IRES, but not the HCV IRES. **A.** Structural models of the Cricket Paralysis Virus Intergenic Region internal ribosome entry site (CrPV IGR IRES, PDB 4v92, left) and Hepatitis C virus IRES (HCV IRES, PDB 5a2q, right). **B.** Native gel electrophoresis of WT, Δ eS25, and eS25-HA 40S ribosomal subunits binding to fluorescently labeled CrPV IGR IRES (left) or HCV IRES (right). Binding reactions were carried out with 30 nM labeled RNAs and 60 nM indicated 40S ribosomal subunits and resolved on acrylamide-agarose composite gels.

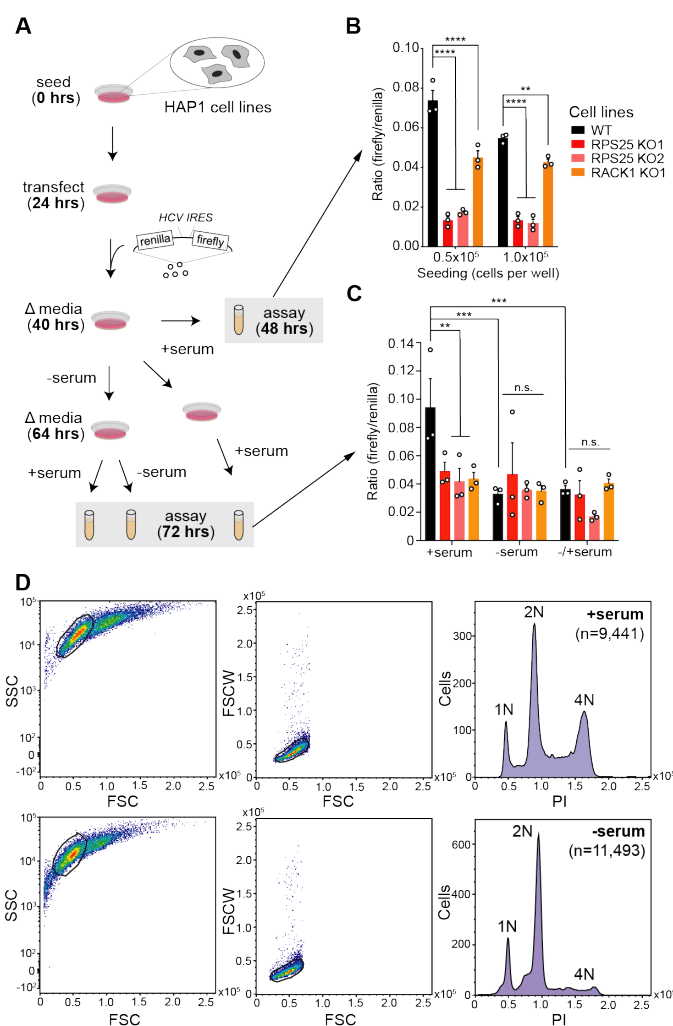


Collectively, these *in vitro* experiments demonstrate that the direct role of eS25 on ribosome recruitment by the CrPV IGR IRES is robust yet likely limited to a single IRES type. Unlike the CrPV IGR IRES, which mimics an elongation complex and utilizes no initiation factors, the HCV IRES mediates translation initiation with select but minimal factor requirements (Johnson et al., 2017). Rather than through 40S recruitment, eS25 and RACK1 could act directly on HCV-IRES-mediated translation by influencing later steps of initiation in concert with initiation factors. For instance, in the 80S-IRES-eIF5B-Met-tRNAi-GMPPNP cryo-EM-based model, domain II of the HCV IRES is reoriented in the vicinity of eS25, and further reorientations are expected during the transition into elongation (**Figure 1-FigS1F-G**) (Yamamoto et al., 2014). Further, in a mass spectrometry analysis of ribosomes isolated by an HCV IRES pull-down of HeLa cell lysate, eS25 was at an altered methylation state versus native ribosomes, further raising the possibility of a functional interaction (Yu et al., 2009). We reasoned that this possibility, coupled with our ability to form 40S- and 80S-IRES complexes with Δ eS25 and Δ RACK1 ribosomes, might be a unique gateway into structural and mechanistic analyses of HCV IRES initiation complexes. Since the requirements for eS25 and RACK1 in HCV IRES-mediated translation had previously been concluded by siRNA knockdown experiments, we felt that a reanalysis of this dependence in cellular experiments was first warranted.

The HCV IRES does not strictly require eS25 or RACK1 for its activity

To demonstrate the essentiality of eS25 for HCV IRES-driven translation, Landry *et al.* depleted eS25 by siRNA knockdown in HeLa cells. They then measured HCV IRES-driven translation of a firefly luciferase relative to that of a cap-dependent Renilla luciferase from a dicistronic reporter construct (Landry *et al.*, 2009). Knockdown was verified by northern blot analysis, and a reduction to ~25-50% IRES activity was observed in two experiments. Similarly, knockdown of RACK1 was shown to reduce HCV IRES translation by ~50% using mono-luciferase reporters in Huh7.5.1 cells (Majzoub *et al.*, 2014). In a previous experiment from our laboratory using a dicistronic HCV IRES reporter, RPS25 KO HAP1 cells were also shown to have reduced but non-zero IRES activity and this was rescued by reintroduction of the RPS25 cDNA fused with a C-terminal SNAP tag (Fuchs *et al.*, 2015).

Figure 2 (half page width). Cell cycle synchronization abolished differences in HCV IRES reporter activity between wild-type and RP KO cells. **A.** Experimental scheme for cell cycle synchronization by serum-starvation and subsequent luciferase assays. **B.** Results from dual-luciferase assays of WT and KO cells at 24 hours post-transfection at two seeding densities. **C.** Results from dual-luciferase assays of WT and KO cells at 48 hours post-transfection at the low seeding density (0.5×10^5 cells/well), under different perturbations of serum conditions. Error bars in B-C represent the standard error of the mean (SEM) from three biological replicates. The cell lines and conditions were analyzed by two-way ANOVA and to maximize sensitivity in the comparisons between pairwise conditions, a Fisher's LSD test was used to determine statistical significance, without taking into account multiple comparisons. This exact experiment was performed on a single occasion, while individual perturbations using the same reporter were performed on separate occasions with similar results. P-values: ≥ 0.05 (n.s.), 0.001-0.01 (**), 0.0001-0.001 (***), and <0.0001 (****). **D.** Example propidium iodide (PI) FACS-based assay to verify cell cycle arrest under serum-starvation conditions. Single cells were identified by manually drawing a window on a plot of Side Scatter (SSC) versus Forward Scatter height (FSC) (left panels), followed by on a plot of Forward Scatter Width (FSCW) versus FSC. Histograms of the single cell intensity from the BluFL2 PMT are shown, from *n* cells in +serum and -serum conditions.



When repeating the analysis with RPS25 KO HAP1 cells, we observed large day-to-day variations in similar experiments coupled with poor expression and ribosome incorporation of eS25-SNAP, as well as an altered growth behavior of the KO cell line. Since HCV IRES dicistronic reporter activity can vary by cell cycle and cellular 40S ribosome levels (Honda *et al.*, 2000; Huang *et al.*, 2012), we designed an experiment to control for confounding variables (**Figure 2A**). We utilized two independent RPS25 KO clones—one isolated following CRISPR/Cas9 mutagenesis (KO1) and another following gene trap insertional mutagenesis and selection (KO2) (Fuchs *et al.*, 2015; Marceau *et al.*, 2016). Additionally, we included a RACK1 KO HAP1 cell line isolated by CRISPR/Cas9 mutagenesis (Jha *et al.*, 2017). WT and KO HAP1 cells were grown by regular passaging and at day 0, cells were harvested, live cells were counted, and then two cell concentrations were seeded into wells of several 24-well culture plates. At 24 hours post-seeding, cells were transfected with the HCV IRES dicistronic reporter plasmid. The next morning, the

media was replaced in wells either with serum-containing medium or media without serum in order to induce cell cycle arrest. A first batch of +serum cells were analyzed 8 hours later, wherein we observed the expected reduction in HCV IRES activity in KO cell lines (**Figure 2B**). Nonetheless, the reporter activity varied between WT cells depending on the seeding concentration, illustrating the potential variability of the assay.

Following 24 hours of serum starvation, cells were either switched back into serum-containing media for 8 hours of growth or left as is. Serum-manipulated cells were then assayed versus cells grown continuously in the presence of serum (**Figure 2C**). Strikingly, while the unmanipulated cells demonstrated a similar trend to that observed the previous day, the apparent reduction in HCV IRES activity in mutant cells was abolished in cells deprived of serum or deprived and replenished. This effect was consistent with cells from both seeding concentrations (**Figure 2—FigS1A**). We confirmed that serum starvation arrested cells at G1 phase of the cell cycle (**Figure 2D and Figure 2—FigS1C**). Notably, while the HAP1 cell line is known to become diploid after continued growth (Olbrich et al., 2017), and we observed a mixture of haploid and diploid cells in our cell lines, there was no clear association between ploidy and HCV IRES reporter results.

Together, the above results indicate that the effect of eS25 or RACK1 depletion on HCV IRES-mediated translation were variable and dependent on the cell cycle. Thus, the previously observed reduction of HCV infectivity in eS25- and RACK1-depleted cells (Landry et al., 2009; Majzoub et al., 2014) may not be due to defects in IRES-mediated translation and may be accompanied by indirect effects. For RACK1 this notion was supported by two recent reports (Gallo et al., 2018; Lee et al., 2019), and we note that neither of these RPs emerged in genome-wide CRISPR/Cas9 or siRNA screens for resistance to HCV infection and replication (Li et al., 2009; Marceau et al., 2016; Tai et al., 2009). In light of potential broad phenotypic consequences of RP loss, these results dampened our previous rationale for mechanistic analyses of RP deletion on HCV IRES function, and catalyzed our pursuit of the cellular consequences of RP loss.

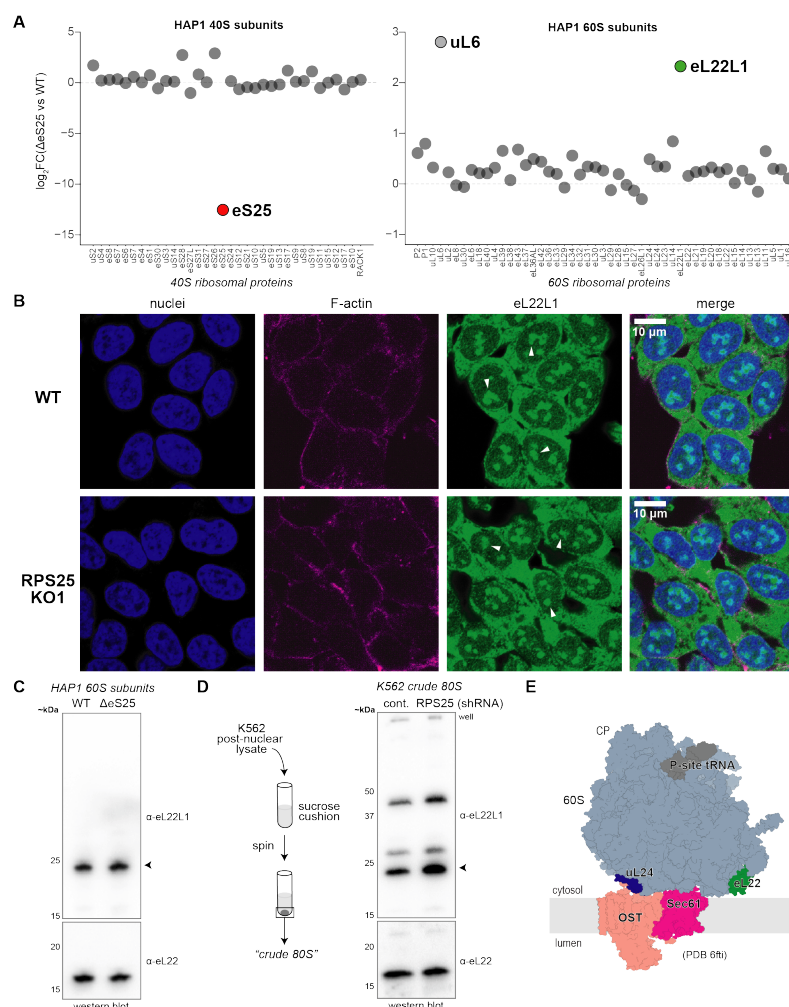
RPS25 loss leads to an unexpected remodeling of the large ribosomal subunit

Given the evidence for indirect effects on translation in RP KO cells, we analyzed WT and KO ribosomes to determine whether cellular adaptations might have altered their composition. We used label-free quantitative (LFQ) LC-MS/MS and compared samples by their LFQ intensities to assess the relative abundance of proteins. We first examined the ribosomes used above, which were purified by a standard high-salt and puromycin splitting protocol in tandem with a paired WT control. RPs were readily detected in ribosomal samples, and each 40S and 60S sample was enriched for small and large subunit RPs, respectively (**Figure 3—FigS1A-D**). We observed the expected reduction of eS25 and RACK1 levels in 40S subunits isolated from KO cell lines (**Figure 3A and Figure 3—FigS1E**). Unexpectedly, in a similar analysis of purified 60S subunits, we detected an increase in the relative ratio of the RP paralog eL22L1 in subunits isolated from eS25 KO but not RACK1 KO cell lines (**Figure 3A and Figure 3—FigS1E**). We also observed an increase in uL6, which we did not further validate, as we were most struck with the RP paralog irregularity at eL22 given literature implicating eL22L1 in diverse aspects of cell biology (discussed below). While most ribosomal protein paralogs are quite similar at the sequence level and therefore challenging to detect, human eL22 and eL22L1 are only 70% identical and therefore distinguishable by LC-MS/MS (**Figure 3—FigS2A**).

eL22L1 expression is unusual in mammals; in mice, RPL22 knockout leads to a compensatory upregulation of eL22L1 (O’Leary et al., 2013), and RPL22L1 is a recurrent hit in synthetic lethal screens of cancer cell lines (Chan et al., 2019; Ghandi et al., 2019; McDonald et al., 2017). In zebrafish, RPL22L1 has been implicated in extraribosomal regulation of pre-mRNA splicing and thus researchers often interpret it as functioning within the nucleus (Zhang et al., 2017). Consequently, the identification of eL22L1 on cytoplasmic human ribosomes was even more surprising. To probe the localization of eL22L1 within HAP1 cell lines, we examined WT and RPS25 KO cell lines by immunofluorescent (IF) staining for eL22L1 (**Figure 3B**). In line with the incorporation of eL22L1 in ribosomes, we observed staining throughout the cytoplasm as well as the expected subnuclear regions (likely nucleoli) (**Figure 3B and Figure 3—FigS3**). To further understand this antibody’s sensitivity, we examined HAP1 60S subunits by immunoblotting and

detected a ~23 kDa product that was present in both WT and KO ribosomes (**Figure 3C**). This indicated that the elevation observed by mass spectrometry was subtle, which was in further agreement with results from RT-qPCR (**Figure 3—FigS2C**). The observed molecular weight (MW) was unexpected given that the expected MW for eL22L1 is ~15 kDa, and might indicate the presence of a post-translation modification for which there is precedence in *Drosophila* (Kearse et al., 2013). There are currently no commercial antibodies verified for western blotting eL22L1, and therefore new reagents and experiments are needed to conclusively verify such a finding.

Figure 3 (2/3 page width). Ribosomal subunit mass spectrometry reveals a remodeled large subunit in the RPS25 KO. **A.** Plot of the log₂ fold-change (log₂FC) in LFQ intensities between ΔeS25 and WT ribosomal subunits. eL41 was not detected in this experiment. **B.** Confocal images of fixed and stained WT and RPS25 KO1 HAP1 cells. Cells were stained with an antibody against eL22L1 alongside staining of nuclei with Hoescht and F-actin with Phalloidin 660. White arrows point to likely nucleolar structures. **C.** Western blot analysis of HAP1 60S subunits for eL22L1 and other large subunit RPs. Arrow points to the antibody-sensitive band at ~23 kDa, which is larger than expected for the protein product (~15 kDa). **D.** Model for the purification of “crude 80S” ribosomes from K562 cells and subsequent use for immunoblotting analysis. Arrow points to expected full-length eL22L1 as in (D), and other bands are expected to arise from post-translational modifications or be non-specific. **E.** Structural model for the position of eL22 within the ER-bound 60S-Sec61-OST complex (PDB 6fti). Gray rectangle represents the ER membrane with OST and Sec61 translocon complexes spanning. Select RPs of the 60S ribosomal subunit (eL22 and uL24—the target of ufmylation) are indicated, as well as P-site tRNA and the central protuberance (CP).



Depletion of eS25 in the K562 cell line has previously been shown to mediate ricin toxin resistance (Bassik et al., 2013), and in unpublished RNA-seq and ribo-seq analysis of these cell lines RPL22L1 was also significantly elevated (G Hess, M Bassik, and N Ingolia, personal communication). To confirm this upregulation, we next purified “crude 80S” from K562 cell lines harboring shRNA targeting RPS25 or a non-targeting shRNA (**Figure 3D**). These ribosomes represent those that result from the first step prior to the splitting reactions used in our purification of ribosomal subunits and thus represent required less material and steps to acquire. Consistent with the expectation, we detected elevated levels of eL22L1 in the RPS25-targeting samples (**Figure 3D**), suggesting that this ribosome irregularity may be a common response to sustained reductions in eS25 levels. Like the HAP1 60S subunits, these crude ribosomes also have an eL22L1 antibody-sensitive band at ~23 kDa, as well as bands at even higher MWs (~27 and ~45

kDa). Given that the ~23 kDa band appears at elevated levels, and this was the same MW observed in the HAP1 ribosomes, we propose that this band is specific. Further, the higher MW bands are also elevated in the RPS25-targeting sample, suggesting that they may represent further modified eL22L1.

eL22L1 is upregulated in transformed cell lines (**Figure 3—FigS2B**), and eL22L1 expression also arises as a result of a mutation in an UFMylation pathway (UFSP2 KO, **Figure 3—FigS2D**) (Walczak et al., 2019). Loss of function mutations in the UFMylation pathway are related to endoplasmic reticulum (ER) stress, and the primary target of UFMylation is uL24 (RPL26), and both it and eL22L1 are proximal to the ER membrane in translocon-bound 60S complexes (**Figure 3E**). These observations raised the possibility that the ribosome irregularity at eL22L1 is a signature of a proteostatic remodeling event related to ER stress in the RPS25 KO that is distinct from the loss of RACK1.

Thus, the eL22L1 irregularity hinted at the existence of cellular remodeling that was KO-specific, may be related to ER and/or nucleolar stress, and potentially linked to phenotypes associated with loss-of-function RPS25 mutations. We therefore hypothesized that a specific proteostatic rewiring of the RPS25 KO, rather than direct effects on translation, might explain certain phenomena. Although we will return to the eL22L1 alteration, we reasoned that first exploring robust phenotypes associated with RPS25 loss might clarify the biological context of such an alteration.

RPS25 loss is protective against flavivirus infection and this correlates with resistance to an ER toxin

RPS25 was the fourth top hit in a genome-wide haploid genetic screen for dengue virus (DENV) host factors and was also identified in a screen of the closely-related Zika virus (ZIKV) (Marceau et al., 2016; Ooi et al., 2019). siRNA studies in other cell lines have further implicated both RPS25 and RACK1 as host factors for DENV propagation (Hafirassou et al., 2017), and RPS25 but not RACK1 was shown to be important for the propagation of the yellow fever virus (YFV), another flavivirus (Petrova et al., 2019). Flaviviruses are positive-sense RNA viruses, and DENV and ZIKV have capped genomic RNAs (gRNAs) implying that their translation could share a common mechanism with canonical cellular capped mRNAs. Given the prior connection of RPS25 to IRES-mediated translation events, one interpretation from the potent DENV resistance phenotype of RPS25-deficient cells is that DENV utilizes a specialized translation mechanism despite the presence of a cap on its gRNA (Hafirassou et al., 2017). Such an interpretation may be supported by the observation that DENV translation can operate under cellular conditions where cap-dependent translation is inhibited (Edgil et al., 2006), and the recent suggestion that the DENV and ZIKV 5' untranslated regions harbor certain IRES properties (Song et al., 2019).

To first test the reported flavivirus resistance phenotype of the RPS25 KO, we performed viral infection experiments using a small panel of viruses on HAP1 cell lines. Utilizing a crystal violet assay, we found that the protection against DENV- and ZIKV-mediated cell death was observed for both RPS25 KOs, and specific for flaviviruses as shown by the lack of protection against a picornavirus (Coxsackievirus B3, CV-B3) and an alphavirus (Chikungunya virus, CHIKV) (**Figure 4A**). Strikingly, both eS25-HA AB clones failed to rescue the WT sensitivity to DENV or ZIKV, despite our confirmation that eS25-HA expresses well and functionally incorporates into ribosomes (**Figure 1B**, **Figure 1—FigS1A-B**, and **Figure 4—FigS1A**). To enable more high-throughput analysis, we employed a DENV infectious clone encoding a Renilla luciferase sequence before the structural proteins (DENV-luc) (Marceau et al., 2016), and performed infections on additional cell lines for multiple durations (**Figure 4B** and **Figure 4—FigS1B**). As predicted by the crystal violet assays, the protection against DENV-luc in both RPS25 KOs was clear and significant, and the eS25-HA AB failed to rescue sensitivity. We observed a reduction in DENV-luc signal in two independent RACK1 KO clones, and found that expression of a C-terminally FLAG-tagged RACK1 (RACK1-FLAG) in the RACK1 KOs rescued this defect (**Figure 4B** and **Figure 4—FigS1B**). Stable expression of eS25-HA or RACK1-FLAG in WT cells did not drastically alter DENV-luc signal, arguing against a dominant-negative effect from expressing the tagged proteins. Unlike our previous dual-luciferase assays, we found that the DENV-luc effect was robust for the RPS25 KOs, with a reproducible reduction of 1-2 log₁₀RLU versus WT. However, given that these luciferase assays are performed with a mono-luciferase virus and such assays cannot be easily normalized, we expect that some of the reduction in signal could be related to factors including altered growth profiles between cell lines.

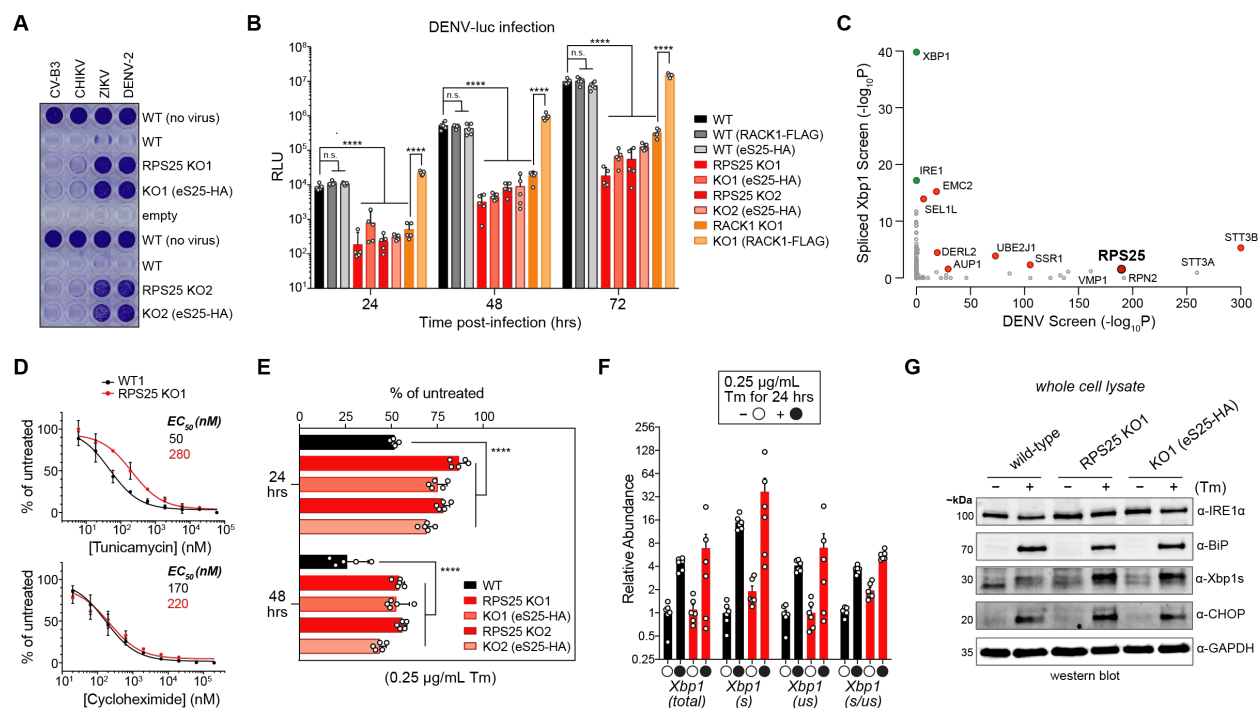


Figure 4 (full page width). RPS25 loss rewires HAP1 cells and drives altered phenotypes related to ER homeostasis. **A.** HAP1 RPS25 KOs demonstrate specific resistance to flavivirus infection. The cell killing effect of four viruses was assayed with crystal violet assays. Cell lines were infected with the Coxsackie B3 virus (CV-B3, MOI=1), Chikungunya virus (CHIKV, MOI=1), Zika virus (ZIKV, MOI=25), and DENV serotype 2 (DENV-2, MOI=25). Similar results were observed in three independent experiments. **B.** The RPS25 KOs demonstrate robust resistance to DENV-luc infection that cannot be rescued by RPS25-HA genetic complementation (eS25-HA AB). The DENV-luc infection experiment was performed with MOI=0.018 with various cell lines and assayed at 24, 48, and 72 hours post-infection. Renilla luciferase activity was represented by relative light units (RLUs) and error bars represent the 95% confidence interval (CI) of n=5 biological replicates. Statistical significance represents the results of a one-way ANOVA for each time point, correcting for multiple comparisons with a Tukey test. **C.** Intersection of published genetic screen results demonstrates shared regulators of DENV resistance and ER stress (via Xbp1 splicing) in HAP1 cells. The -log₁₀ FDR-corrected P-value (-log₁₀P) of the spliced Xbp1 screen (Brockmann et al., 2017) was plotted against DENV screen results (Marceau et al., 2016). The Xbp1 screen was a FACS-based assay and identified both positive and negative regulators of the pathway, while the DENV screen was a live/dead screen and therefore mutations in significant hits provide resistance to DENV-mediated cell death. Green colored dots represent top positive regulators that validate the Xbp1 screen. Red colored dots represent shared hits between the two screens. All shared hits are negative regulators in the Xbp1 screen. **D.** RPS25 KO1 cells demonstrates dose-dependent resistance to Tm-mediated cell death. Cells were assayed with a MTT proliferation assay 48 hours after drug treatment and the absorbance at 570 nm for treated cells was normalized to untreated cells. Error bars represent the 95% CI of three biological replicates. **E.** Resistance to Tm-mediated cell death is a common and irreversible phenotype associated with RPS25 loss in HAP1 cells. As in (D), HAP1 cells were assayed by an MTT assay, but using a single Tm concentration (0.25 µg/mL) and normalized to an untreated control for two time points post drug treatment. Error bars represent the 95% CI of n=5 biological replicates. Similar results were observed in two independent experiments. P-values: ≥ 0.05 (n.s.) and <0.0001 (****). **F.** RT-qPCR assay of Xbp1 splicing in WT and RPS25 KO1 cells following low dose Tm treatment for 24 hours. Error bars represent the SEM of n=6 biological replicates. Relative abundance is normalized to WT Xbp1(us) at 1. No statistical difference was observed by one-way ANOVA and therefore none shown, despite a reproducible increase in Xbp1(s/us) observed in two independent experiments. **G.** Western blot of cell lysates from WT, RPS25 KO1, and eS25-HA AB cells treated with or without a low dose of Tm (0.25 µg/mL) for 24 hours.

To examine more deeply the robustness of viral infection defect in the RP KOs, we tested a series of additional controls. First, the protection against DENV was not predicted by the haploid genetic screen, and we have previously observed that the RACK1 KO has a reduced growth rate (Johnson et al., 2019). We therefore tested another HAP1 KO clone with a growth defect (eIF3H KO) and this demonstrated a reduction in DENV-luc infection, albeit with a lower magnitude (**Figure 4—FigS1B**). By performing an infection with a CV-B3 virus encoding Renilla luciferase, which has much more rapid infection kinetics than DENV, we also found that all KOs and ABs showed an infection defect at early but not late time points supporting the lack of resistance in crystal violet assays (**Figure 4—FigS1C** and **Figure 4B**). To further verify that the RPS25 KO authentically reduced viral infection levels, we next infected WT and KO cells with DENV and checked the expression of DENV proteins by immunoblotting analysis, while performing a plaque assay in parallel to measure the production of new infectious particles. At 48 hours post-infection, we observed strong reductions in both structural (envelope and capsid) and non-structural (NS1 and NS3) DENV proteins as well as a significant reduction in plaque forming units from both RPS25 KOs (**Figure 4—FigS1D**). Notably, reduced levels of nearly all viral proteins were still visible from the KOs indicating that some translation did occur from infectious virus, meaning that RPS25 loss does not completely abolish viral infection or translation. Altogether, the results from the above infection assays indicate that the RPS25 KO viral resistance is robust, flavivirus-specific, and apparently irreversible.

RPS25 is a hit in numerous published genetic screens exploring apparently unrelated phenotypes (**Figure 4—FigS2A**) (Brockmann et al., 2017). Given our prior results pointing towards ER stress in the RPS25 KO, we intersected the results from the DENV resistance screen with that from a spliced Xbp1 (Xbp1s) screen as a proxy for ER stress (**Figure 4C**) (Brockmann et al., 2017; Marceau et al., 2016). DENV and ZIKV conduct much of their lifecycle in specialized vesicles derived from ER membrane (Neufeldt et al., 2018), and genome-wide screens for host factors have consistently uncovered subunits of ER-resident protein complexes, including oligosaccharyltransferase (OST) subunits (STT3A, STT3B, and others), components of the ERAD pathway (UBE2J1, DERL2), and translocon-associated protein complex (TRAP) subunits (SSR1 and others). Indeed, several of the host factors that provide resistance to DENV-mediated cell death also increase cellular levels of spliced Xbp1 in response to an 8-hour treatment with 2 μ M tunicamycin (Tm) (**Figure 4C**) (Brockmann et al., 2017). While the magnitude of DENV and Xbp1s effects are not directly correlated, no DENV-resistance factors score as positive regulators of Xbp1 splicing, and the Xbp1s screen is well-validated by the appearance of XBP1 and IRE1 as strong positive regulators. The appearance of RPS25 in the Xbp1s screen, which is thus a link to ER stress, struck us as non-intuitive given that it is not directly related to ER function. However, we reasoned that appearance of RPS25 as a top hit in a ricin toxicity screen (Bassik et al., 2013), and the utilization of ERAD components for ricin toxin processing, might further suggest that secretory pathway remodeling was a common feature associated with RPS25 loss. We therefore pursued close examination of the reported DENV and ER stress phenotypes in HAP1 cells as a window into this relationship.

We queried the Xbp1 splicing phenotype to explore the relationship of RPS25 loss to ER stress. We titrated tunicamycin onto WT and RPS25 KO1 cells, and measured EC₅₀ values for growth inhibition using proliferation assays after 48 hours of treatment. We observed an increase in the EC₅₀ value for the RPS25 KO versus WT cells (**Figure 4D**), which appeared to arise from reduced cell death in the KO by visual inspection. In contrast, a titration of the translation inhibitor cycloheximide (CHX) to WT and RPS25 KO cells performed in parallel did not differentially affect the cell lines, demonstrating that the effect is toxin specific. To test the robustness of the toxin resistance, we treated both RPS25 KO clones and their respective ABs with a low dose of tunicamycin (0.25 μ g/mL) for 24 and 48 hours and assessed resistance with another proliferation assay. As with the flavivirus resistance phenotype, we found that the effect is significant for both KO clones and not reversed by eS25-HA expression (**Figure 4E**). We note that both untreated RPS25 KOs demonstrate some baseline proliferation defect in these assays, and that the RPS25 KO2 clone has the most severe defect that is modestly rescued by eS25-HA expression (**Figure 4—FigS2B**), yet still fails to rescue the flavivirus or toxin phenotypes. Tunicamycin resistance has been demonstrated to be a general response to RP KO in yeast, where this had been generally attributed to reduced ER burden through diminished protein synthesis (Steffen et al., 2012). Our observation that

cycloheximide and tunicamycin incur different outcomes in the RPS25 KO, and that the RACK1 KO does not display specific resistance to tunicamycin (**Figure 4—FigS2B**), suggest that the RPS25 KO mechanism might be more complicated.

Tunicamycin activates Xbp1 splicing and the unfolded protein response (UPR) indirectly by inhibiting an early step of glycoprotein synthesis—resistance could therefore come about through a number of mechanisms. To confirm that tunicamycin still enters KO cells and activates the UPR, we first applied a RT-qPCR assay to measure the ratio of spliced/unspliced Xbp1 and other UPR markers (Oslowski and Urano, 2011). Tunicamycin activated Xbp1 splicing and increased ATF4 levels in the RPS25 KO similar to WT, and we observed a modest but non-significant increase in baseline levels of spliced Xbp1 in the KO versus WT (**Figure 4F** and **Figure 4—FigS2C**). We further observed that this response was distinct from the RACK1 KO (which displayed weak activation of Xbp1 splicing), and there was an observable but non-significant decrease in baseline levels of ATF4 in the RPS25 KO. By immunoblotting, we observed that the low-dose tunicamycin treatment also led to increased levels of Xbp1s, BiP, and CHOP in the RPS25 KO and its respective AB (**Figure 4G**). As expected from the genetic screen result, we observed the apparent increase in the levels of Xbp1s by immunoblotting following tunicamycin treatment, although as with the RT-qPCR result, this change was subtle. To assess a broader catalog of proteins related to cellular homeostasis and stress, we further probed the same cell lysates with a panel of antibodies (**Figure 4—FigS2D**). Most notably, we observed no clear alterations in small or large subunit RP levels in the KO or AB, steady levels of the tumor suppressor p53, and no clear difference in levels of OST subunits or alterations in glycosylation of the STT3A substrate pSAP. We did, however, observe increased levels of eS6 phosphorylation in the RPS25 KO and AB relative to WT, a finding that is reminiscent of altered RPS6 kinase activity observed in RPS19 mutant cells (Heijnen et al., 2014). Thus, the RPS25 KO appears to have an intact UPR and only subtle alterations to the components measured here.

Flavivirus infection and DENV proteins have been shown to activate the UPR via splicing of Xbp1 (by the activity of the endoribonuclease and kinase IRE1 α) (Perera et al., 2017; Yu et al., 2006), and in turn the UPR has been shown to affect translation-related processes such as RP ubiquitination (Higgins et al., 2015). Furthermore, the ubiquitination of select 40S subunit RPs, including RPS10 (eS10) and RPS20 (uS10), is linked to ribosome-associated quality control of stalled ribosomes (Juszkiewicz and Hegde, 2017; Sundaramoorthy et al., 2017). We therefore asked whether artificially perturbing the UPR or RP ubiquitination could interfere with DENV infection to assess whether these might represent indirect effects that follow RPS25 loss. Following stable expression of previously-studied eS10 and uS10 lysine mutants and an IRE1 α kinase domain mutant in HAP1 cells (Lipson et al., 2008; Sundaramoorthy et al., 2017), we infected cells with DENV-luc and assayed infection over multiple time points. While the RACK1 KO showed the expected decrease in this assay (a protein also linked to RP ubiquitination), we observed only modest changes in DENV infection of these cell lines (**Figure 4—FigS1E**). Prompted by the apparent association of eL22L1 levels with ER stress described earlier, we next probed its relationship to the UPR and flavivirus resistance. By RT-qPCR, we again observed that eL22L1 transcript levels are modestly elevated in the RPS25 KO but do not respond to tunicamycin treatment (**Figure 4—FigS2C**). Given the strong increase in eL22L1 levels in K562 cells harboring an shRNA targeting RPS25 (**Figure 4D**), we additionally infected these cell lines with DENV-luc. Again, we observed only modest changes in luciferase signal, and the cells with shRNA targeting RPS25 instead demonstrated a relative increase in DENV-luc infection (**Figure 4—FigS1F**). Thus, elevated eL22L1 levels are not sufficient to protect against DENV infection, meaning that dysregulation of eL22L1 in the RPS25-deficient ribosomes are likely not causal of the RPS25 KO phenotypes. Finally, since the RPS25 KO cells display higher baseline levels of Xbp1 splicing, and sustained tunicamycin treatment in yeast is known to drive aneuploidy (Beaupere et al., 2018), we karyotyped both of the RPS25 KO clones to ensure that there were no new chromosomal abnormalities (**Figure 4—FigS2E**). While the cell lines displayed different ratios of haploid and diploid cells (discussed earlier), we observed no evidence of aneuploidy besides the expected Philadelphia chromosome and a fragment of chromosome 15 extending off of chromosome 19, observed in the parental HAP1 clone (Carette et al., 2011). Thus, the failure of the eS25-HA AB to rescue KO phenotypes is not due to aneuploidy.

Dengue virus does not require RPS25 for cell entry or initial translation

The above experiments established that RPS25 KO cells are resistant to flavivirus infection and modulations to tunicamycin-induced ER stress. Yet, we discovered no obvious culprit for these resistance phenotypes, besides their irreversible nature, and with regard to DENV it was unresolved at which stage of its lifecycle this protection acts and whether eS25-deficiency affects DENV translation. Fortunately, DENV infection kinetics enable the dissection of its lifecycle: in the first ~8 hours following infection, DENV enters cells and translates its genome, and only after this time (with sufficient viral proteins and replication compartments established) does the replication phase become dominant (Neufeldt et al., 2018). We therefore performed a short time-course infection experiment with DENV-luc and WT, RPS25 KO, and AB cells. In these experiments, we used CHX and the NS5 (RNA-dependent RNA polymerase) inhibitor MK0608 as controls to inhibit translation and replication, respectively. While the expected infection defect was observed at 24 hours post-infection for both MK0608-treated cells, RPS25 KO1, and eS25-HA AB cells, we observed only minor differences between cell lines at 4- and 8-hours post-infection (**Figure 5A** and **Figure 5—FigS1A**). We observed a similar effect with the RPS25 KO2 (**Figure 5—FigS1B**), together indicating that eS25 is not required for viral entry or initial translation (**Figure 5B**). This result is similar to that observed following siRNA knockdown of RPS25 or RACK1 in HeLa cells, where it was interpreted that these RP deficiencies might instead inhibit translation at later stages of infection when DENV has shut down aspects of host translation (Hafirassou et al., 2017). Unfortunately, there are no straightforward approaches to distinguish translation and replication at later stages, but given the failure of the eS25-HA AB to rescue the tested phenotypes, a translational alteration should not be assumed.

We next used microscopy of DENV-infected RPS25 KO cells to probe mechanisms of flaviviral resistance at late stages of infection. WT and RPS25 KO cells were infected with DENV for 24 hours before fixing, staining for structural (envelope, E) and non-structural (NS3) proteins, and imaging. In all cases, we observed specific staining for DENV proteins in infected WT and KO cells, as demonstrated by the absence of signal in uninfected cells (**Figure 5C** and **Figure 5—FigS1-S4**). The appearance of staining for E protein and NS3 was most prominent adjacent to nuclei, likely corresponding to the ER. In addition to this location, we observed E protein staining at the cell boundary, which likely corresponds to budding virions at the membrane (**Figure 5C**). The levels of DENV proteins were visually attenuated in both RPS25 KOs versus WT, yet most striking was the qualitative loss of E protein staining at the cell boundary in both KOs (**Figure 5C**, **Figure 5—FigS1C**, and **Figure 5—FigS3**). This finding raised the possibility that ultrastructural changes might be present in the RPS25 KO in the context of DENV infection, such as alterations in the ER membrane-derived replication vesicles (Welsch et al., 2009). We therefore interrogated WT and RPS25 KO cell slices by transmission electron microscopy (TEM) following 24 hours of DENV infection. To our partial surprise, we readily observed the appearance of DENV-induced vesicles in both KO clones that were absent in uninfected cells (**Figure 5D**, **Figure 5—FigS1D**, and **Figure 5—FigS5**). We also observed virions, both at the ER and at the cell periphery (**Figure 5—FigS1D**). The DENV-induced replication vesicles were not qualitatively different in size and shape between WT and KO cells, though the appearance of virions at the cell boundary was less common in the KOs, consistent with our IF data. Due to the subtlety of these changes and a small sample size that might have biases from cell sectioning, we did not quantitate them. Regardless, the imaging confirmed the flavivirus resistance of the RPS25 KO, further demonstrating that the resistance is not absolute and derives from a possibly indirect mechanism. Such a mechanism does not act to completely abolish DENV translation or the formation/utilization of ER-membrane-derived vesicles but could foreseeably interfere with other aspects of the secretory pathway.

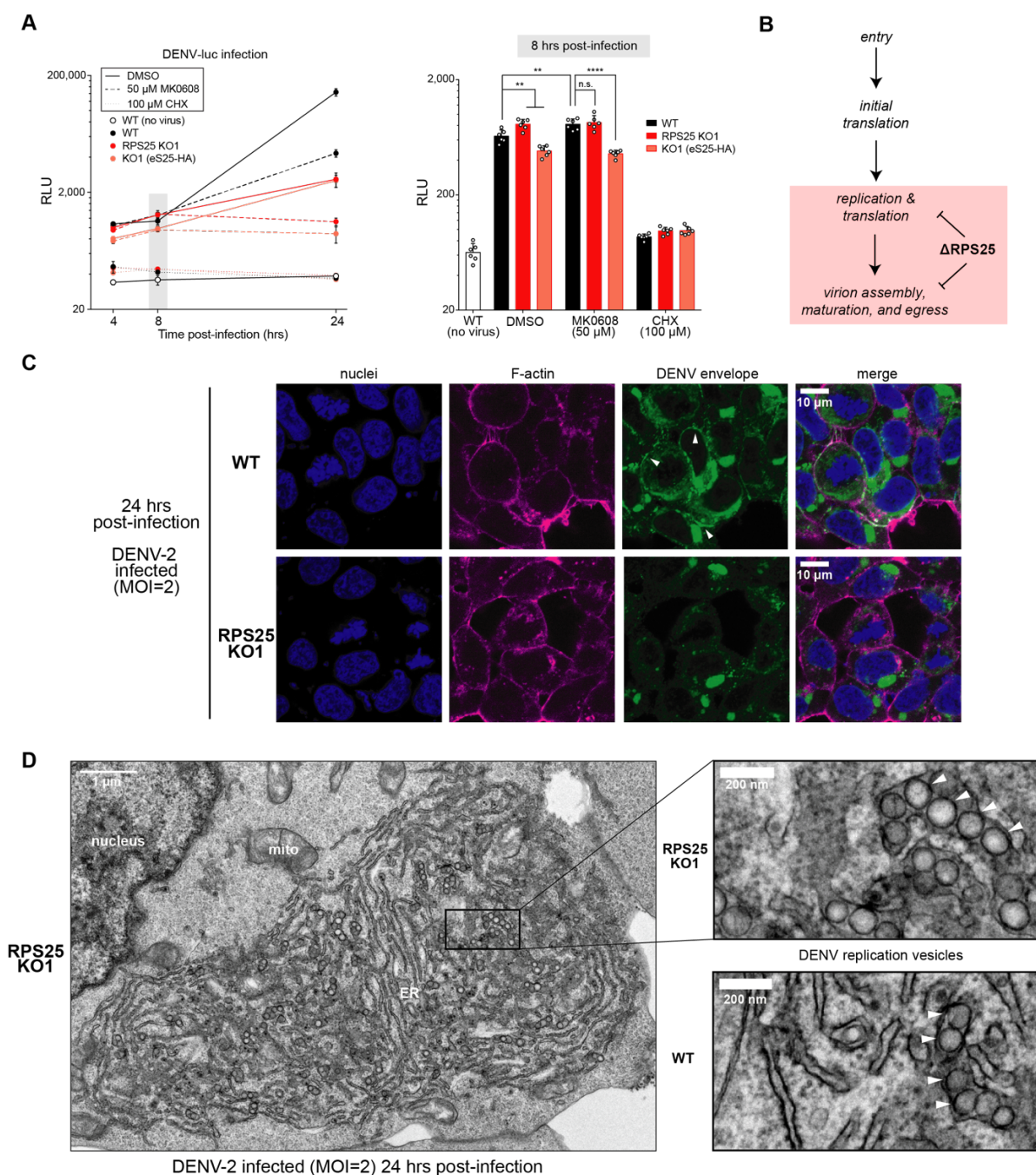


Figure 5 (full page width). Loss of RPS25 does not interfere with dengue virus entry or initial translation, but instead acts at a late stage of infection when translation and replication are coupled. **A.** Time course of DENV-luc infection in WT, RPS25 KO1, and eS25-HA AB cells. At time 0, cells were infected with MOI=0.05 DENV-luc and assayed 4, 8, and 24 hours post-infection with select drug treatments to inhibit viral replication (MK0608) or mRNA translation (CHX). Left panel shows the averages of $n=6$ biological replicates for each cell line and time point with error bars representing the 95% CI, while right panel shows the full data points for the 8-hour time point. Statistical significance was determined with a two-way ANOVA and Tukey multiple comparison test for each cell line and treatment at respective time points. Only comparisons for DMSO- and MK0608-treated cells are shown, as the differences for no virus and CHX-treated cells are visually obvious. A similar result was observed from two independent experiments. P-values: ≥ 0.05 (n.s.), 0.001-0.01 (**), and <0.0001 (****). **B.** Model for the defect in DENV infection following RPS25 loss in HAP1 cells, wherein the major effect appears >8 hours post-infection when translation and replication are

coupled. **C.** Confocal images from staining of WT and RPS25 KO1 HAP1 cells infected with DENV-2 at MOI=2. Fixed cells were stained with an antibody against the dengue envelope (E) protein alongside staining of nuclei with Hoescht and F-actin with Phalloidin 660. White arrows point to bead-like structures of the E protein within the cell periphery of infected WT cells that is largely absent from KO cells. **D.** Transmission electron microscopy (TEM) images of an RPS25 KO1 cell section prepared following infections with DENV-2 at MOI=2. ER = endoplasmic reticulum and mito = mitochondria. Right panels show the appearance of ER membrane-derived replication vesicles (white arrows). The upper right panel represents an inset of the left panel, while the bottom right panel represents an inset from a WT cell (full image in Figure 5—Figure Supplement 1).

RPS25 knockout cells are transcriptionally rewired and share a common cell state

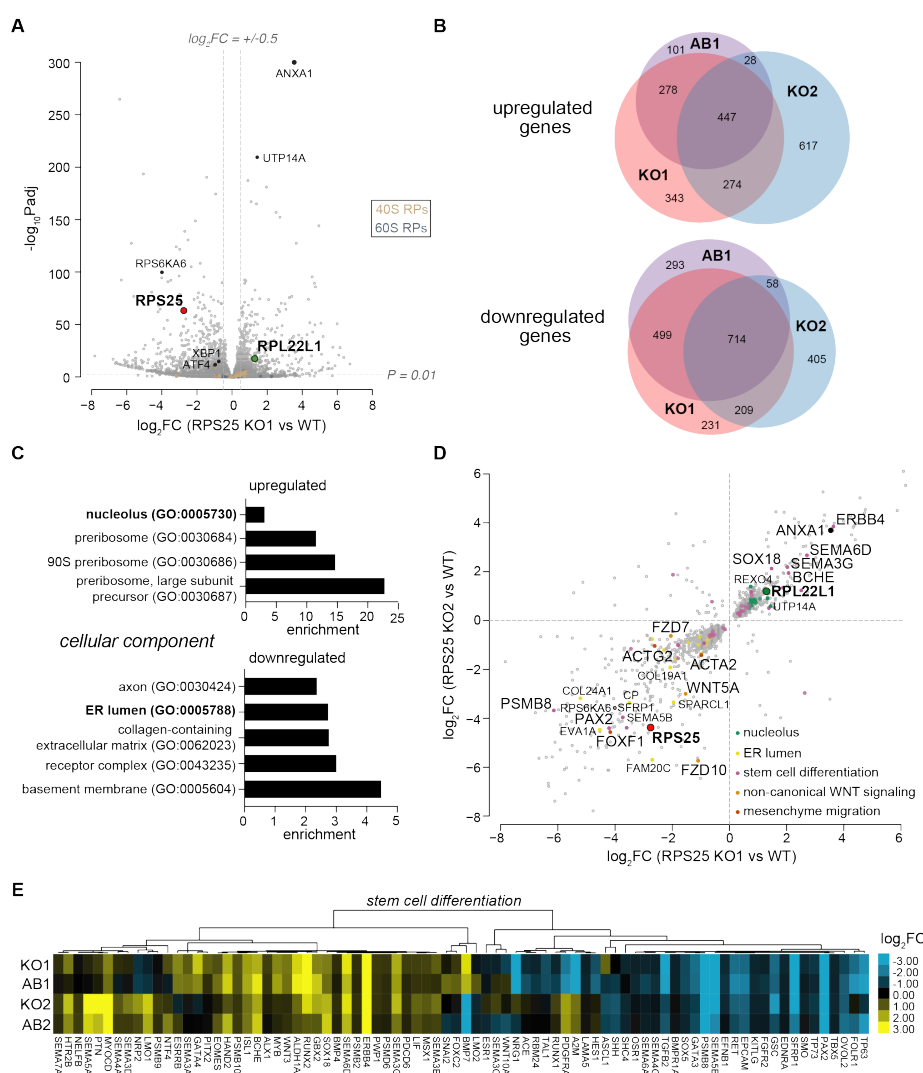
Our prior RT-qPCR and western blots uncovered meaningful changes in the RPS25 KO cell biology, yet they were inherently biased to a small subset of targeted transcripts and proteins. We remained perplexed by the failure of the eS25-HA AB to rescue multiple phenotypes and therefore hypothesized that RPS25 KO cells transitioned to a new cell state. To uncover molecular details that might explain such a state, we turned to transcriptome-wide measurements. Since the previous observations argued against a role in translation, we pursued RNA-seq of polyadenylated mRNAs as the first step to acquire a snapshot of the transcriptional state of wild-type, RPS25 KOs, and eS25-HA AB HAP1 cells. Encouragingly, by first comparing the RPS25 KO1 and WT differentially expressed genes, we found that the data supported and verified several previous observations made by RT-qPCR (**Figure 6A**). Notably, while most RP transcripts were present at similar levels, RPS25 transcripts were strongly reduced and RPL22L1 had a modest, significant increase in the RPS25 KO1. Moreover, the UPR markers XBP1 and ATF4 showed significantly reduced levels, and all but the XBP1 change was seen in a similar analysis of WT versus RPS25 KO2 (**Figure 6—FigS1A**). Potentially related to ribosome homeostasis, we also observed that both KOs displayed a decrease in the eS6 kinase RPS6KA6 and a significant increase in the ribosome biogenesis factor UTP14A. The most significantly upregulated gene in both conditions was ANXA1, encoding Annexin A1—an anti-inflammatory protein with broad cellular roles (Sheikh and Solito, 2018).

To interrogate the shared transcriptional changes, we established relatively liberal fold-change cut-offs to narrow in on differentially expressed genes with FDR-adjusted P-values (P_{adj}) <0.01. We first examined the overlap between upregulated ($\log_2FC > 0.5$) and downregulated ($\log_2FC < -0.5$) transcripts in the KO1, KO2, and AB1 conditions (**Figure 6B**). The KO1 and its AB showed a better overlap than changes for KO2, which was consistent with the principal component analysis (PCA) of RNA-seq replicates from all conditions (**Figure 6—FigS1B**). Of note, the PCA indicated that the KOs are about as dissimilar from each other as they are from WT and displayed more internal variability between replicates. Despite the many incoherent clonal differences, both KOs share common, irreversible resistance phenotypes, so we considered their divergence a benefit for our analysis. We next examined the overlap between upregulated and downregulated transcripts from all conditions using gene ontology (GO) analyses (**Figure 4—FigS1C-D**). By analysis of Cellular Component ontologies, we observed the upregulation of GOs related to events in the nucleolus, and downregulation of GOs related to the extracellular matrix, cell communication, and the ER lumen (**Figure 6C**). In a similar vein, examination of upregulated Biological Process ontologies revealed a number of categories related to ribosome biogenesis, seconded only by the stem cell differentiation GO (**Figure 6—FigS1D**). Also related to differentiation processes, we observed mesenchyme migration and non-canonical WNT signaling as some of the top downregulated Biological Process GOs.

In order to examine these common changes further, we plotted the fold-changes of KO2 versus those of KO1, clustered genes within select GOs, and visualized the results using heatmaps. Nucleolus-related genes, while generally upregulated, had only modest fold-change elevations (**Figure 6D** and **Figure 6—FigS1E**). Given the prior suggestion of nucleolar dysregulation by altered eL22L1 levels in KO ribosomes (**Figure 3**), we explored this effect by quantitative analysis of IF images from staining the protein products of altered nucleolar protein-coding transcripts (DDX21 and eL22L1, **Figure 6—FigS2**). We found that both RPS25 KOs had increased DDX21 signal in subnuclear regions without notable increases in nuclear area (**Figure 6—FigS2C**). With eL22L1, which also has a prominent extranuclear localization,

such a trend was much less clear. We further observed that infection of cells with DENV attenuates the DDX21 signal within nuclei for all cell lines (**Figure 6—FigS2A,C**), perhaps unsurprising given that DENV proteins (NS5 and capsid) are known to shuttle to the nucleolus and multiple viruses perturb nucleolar function (Boulon et al., 2010; Fraser et al., 2016; Tiwary and Cecilia, 2017). Taken together, these data support there being a common, irreversible signature of nucleolar dysregulation in the RPS25 KO cell lines that may be relevant to phenotypes including but not limited to DENV infection.

Figure 6 (2/3 page width). RPS25 KO clones are distinct at the transcriptional level but share common, irreversible alterations related to ribosome biogenesis, the secretory pathway, and cell differentiation. **A.** Volcano plot of RNA-seq fold-changes for RPS25 KO1 versus WT HAP1 cells. Y-axis represents the negative log₁₀ FDR-adjusted P-values ($-\log_{10}\text{Padj}$), while x-axis represents the log₂ fold-change ($\log_2\text{FC}$). Values are derived from the results from analysis of n=6 biological replicates for each cell line. Select genes are filled in and colored to show transcriptional changes related to translation, the UPR, and other top changes. RPs are colored as shown in the legend. To indicate value cutoffs for subsequent ontology analysis, a horizontal gray line is shown at $\text{Padj}=0.01$ and vertical gray lines are shown at $\log_2\text{FC}=\pm 0.5$. **B.** Venn diagrams of RNA-seq upregulated and downregulated genes between RPS25 KO1, RPS25-HA AB1, and RPS25 KO2 HAP1 cells. Gene lists are based on the significance and FC cutoff described in (A). **C.** GO analysis for Cellular Component from shared upregulated and downregulated genes in the RPS25 KOs and ABs. Gene lists are based on the overlap of all four conditions as in in Figure 6—Figure Supplement 1C. Only cellular components with FDR-corrected P-value<0.05 are shown with their fold enrichment. **D.** Common shared significant fold-changes for all RPS25 KOs and ABs. Showing FC for all genes with $\text{Padj}<0.01$ in RPS25 KO1 and KO2 conditions. Select genes are annotated based on categorization as indicated to highlight cellular compartments that match the ontology analysis of (C), wherein upregulated nucleolus-related or downregulated ER lumen-related genes are colored. Select differentiation-related genes are also indicated, including those from stem cell differentiation, non-canonical WNT signaling, and mesenchyme migration ontologies. **E.** Heatmap from hierarchical clustering of $\log_2\text{FC}$ s for each condition by genes within the stem cell differentiation gene ontology (GO:0048863). Only genes with $\log_2\text{FC}<-0.5$ or >0.5 in at least two conditions are shown.



We next examined a few other shared transcriptional changes from the RNA-seq dataset. First, we considered GOs related to cellular differentiation given their obvious connection to a cellular state change.

Stem cell differentiation scored as a top upregulated GO after ribosome biogenesis, so we clustered and plotted this ontology (**Figure 6E**). Though of smaller categories, we also annotated the fold-change plot for certain genes related to mesenchyme migration (ACTA2, ACTG2, and FOXF1) and non-canonical WNT signaling (WNT5A, FZDZ, and FZD10) (**Figure 6D**). Here, there was no cohesive pattern to indicate a known cellular transformation event, such as the epithelial-mesenchymal transition (EMT), though there were several differentiation-related genes that demonstrated strong, irreversible alterations (FOXF1, ERBB4, PSMB8, and PAX2). Perhaps noteworthy is the complementary evidence from published genetic screens that implicate RPS25 as a strong negative regulator of ABC-WNT signaling (Brockmann et al., 2017), which might be related to the concerted decrease in genes related to this pathway in the KOs (**Figure 4—FigS2A**). Second, consistent with the indication of ER stress in the RPS25 KOs and potential alterations in the secretory pathway, ER lumen transcripts were strongly and irreversibly downregulated (EVA1A, CP, COL24A1, and FAM20C) and upregulated (BCHE, FUCA2, PTPRN2, and PDGFD) (**Figure 4—FigS1E**). Again, such changes did not fit a clear pattern, but given their irreversibility, may correspond to meaningful aspects of the state change. Collectively, the transcriptional analysis supported and expanded previous observations related to proteostatic rewiring and reinforced the possibility that a state change occurred in the RPS25 KOs.

Membrane mass spectrometry supports a rewired cell state of the RPS25 KO and nominates Annexin A1 as a prominent biomarker

Informed by our transcriptional analyses, we fractionated and analyzed select cellular samples by LC-MS/MS to further examine whether loss of eS25 led to a new cell state. Given the prior eL22L1 observation and signatures of ribosome biogenesis dysregulation in the RNA-seq dataset, we began with an analysis of ribosomes purified under a variety of conditions to survey a broad catalogue of ribosome-associated proteins. Crude 80S ribosomes, as described earlier for K562 ribosomes (**Figure 3D** and **Figure 7—FigS1A**), were strongly depleted for eS25 levels in the two HAP1 RPS25 KO samples, which was restored in one eS25-HA AB (**Figure 7—FigS1B**), further validating the ribosome incorporation of this tagged protein. In contrast, we did not observe a strong reduction in ribosome eS25 levels in the K562 samples (**Figure 3D**), yet as predicted by the prior immunoblotting analysis, we detected elevated levels of eL22L1. Unexpectedly, we also observed altered levels of ER-related non-RPs, including the OST subunits (RPN-1, RPN-2, and STT3-A) and the signal recognition particle 72 (SRP72), in crude 80S samples from eS25-deficient HAP1 and K562 cells (**Figure 7—FigS1B**).

To assess the ribosome-associated proteome, we also analyzed monosome and polysome samples from WT, RACK1 KO, and RPS25 KO HAP1 cell lines (**Figure 7—FigS4C-H**). The monosome and polysome samples were distinct from one another (**Figure 7—FigS4D-F**), and the expected reductions in RACK1 or eS25 were clear in both samples (**Figure 7—FigS4G-H**). The monosome samples contained other large and abundant non-ribosomal complexes, such as the chaperonin TRiC, that likely sediment in the same range as monosomes without being ribosome-bound (**Figure 7—FigS4G**). Nevertheless, we also observed an increase in the ribosome biogenesis proteins NOB1, LSG1, and PNO1 within the monosome samples of both KOs relative to WT. This provides further support for dysregulated ribosome homeostasis in eS25 knockout cells, as suggested by our RNA-seq analyses and the increased ratio of monosome/polysome absorbance at 254 nm (**Figure 7—FigS4C**). Similar to the crude 80S samples, we detected relative decreases in OST subunits and other ER-related proteins in the KO mono samples. Finally, we observed elevated levels of eL22L1 in all RPS25 KO samples, but not RACK1 KO samples, which instead appeared to have a specific decrease of the ribosome-associated and stress-related protein SERBP1 in both monosome and polysome samples (**Figure 7—FigS4G-H**) (Muto et al., 2018). Taken together, the ribosome mass spectrometry results suggested broad irregularity in the proteostasis of RP KO cell lines that was both distinct and overlapping between the RP KOs. We also observed alterations in ER-related proteins, potentially supporting earlier phenotypic and transcript measurements. These observations are nevertheless only suggestive as the ribosome purifications were performed without replicates due to the low-throughput nature of the purification strategies.

To better assess the ER proteome of the RPS25 KO cell lines, we next purified and analyzed cellular membrane fractions. We followed a digitonin-based extraction protocol used previously to isolate “ER membranes” (**Figure 7—FigS2A**) (Stephens et al., 2008). To improve confidence in our measurements, we analyzed three biological replicates of each WT, RPS25 KO1, and RPS25 KO2 cell lines, finding that these were overall well-correlated (**Figure 7—FigS2C**). Encouragingly, by analysis of average LFQ intensities, we found that the membrane purification identified many known ER proteins (Calnexin, BiP, and others) and RPs at relatively high LFQ intensities (**Figure 7—FigS2B**). However, there was no obvious dysregulation of certain ER components as suggested by the above ribosome mass spectrometry, indicating that the previous observation may only be detected following sedimentation of high MW cellular components. Nevertheless, comparison of significant fold-changes between KO and WT membrane was nicely validated by the strong reduction in eS25 and increase in eL22L1 (**Figure 7A**). The 60S-binding protein eIF6 was also at elevated levels, supporting the expected ribosome dysregulation. These changes were shared with KO2, though as with the RNA-seq, the RPS25 KOs displayed several prominent and unique features for each KO. To delineate common changes, we established significance ($P < 0.05$) and FC cutoffs for upregulated ($\log_2FC > 0.5$) and downregulated ($\log_2FC < -0.5$) proteins in both KOs (**Figure 7A** and **Figure 7—FigS2D**). We plotted the FCs for KO2 versus KO1 and identified a shared set of 94 upregulated and 96 downregulated proteins (**Figure 7—FigS2E-F**). By ontology analysis, the upregulated list demonstrated elevated levels of cytosolic and mitochondrial ribosome related proteins, and a group affecting mitochondria gene expression (**Figure 7—FigS2G**). In contrast, the downregulated list illustrated potent disruption of the ER-related processes and other cellular biosynthesis and metabolism (**Figure 7—FigS2G**). The membrane proteome thus supports the existence of a common, systems-wide dysregulation of ribosome homeostasis, the endoplasmic reticulum, mitochondria, and other processes in the RPS25 KO.

Our primary aim for the proteomics was to validate the shared, irreversible changes observed by RNA-seq as a way to characterize a cellular state change. We therefore intersected the lists of differentially expressed proteins from membrane mass spectrometry with the differentially expressed genes from RNA-seq (**Figure 7B**). We identified small groups of 13 shared upregulated and 11 shared downregulated genes, which we expect to represent high-confidence alterations in the RPS25 KO. Given the prominence of ANXA1 (Annexin A1) in both data sets, its multifaceted cellular roles (Sheikh and Solito, 2018), and relationship to the secretory pathway (including the recent identification of it as a marker of microvesicles (Jeppesen et al., 2019)), we further validated this change by immunoblotting and microscopy. By western blot, Annexin A1 was unambiguously upregulated in both RPS25 KOs and their ABs, and at reduced levels in WT, RACK1 KO1 and AB1, indicating that it is not a general response to small subunit RP perturbation (**Figure 7C**). Although not necessarily causally linked to the RPS25 KO phenotypes, Annexin A1 levels may be a signature of the RPS25 KO cell state, and its upregulation likely comes about from transcriptional activation. Annexin A1 has been linked to autophagy modulations (Zhu et al., 2018), as has perturbed eS6 kinase signaling (Heijnen et al., 2014), so we blotted the same cell lysates with a couple other related markers to assess whether they display irreversibility (**Figure 7—FigS3A**). We found that the previously observed elevation in eS6 phosphorylation (eS6-P) still held for both RPS25 KOs and ABs, and we also observed an increase of eS6-P in the RACK1 KO and a partial rescue in its AB. Probing with the autophagy marker LC3B demonstrated a similar switch, wherein the RPS25 KOs display an irreversible increase in the low molecular weight LC3B-II band, which is similar in the RACK1 KO and rescued by its AB. Thus, the RPS25 KO has signs that might indicate autophagy alterations through an increase in the lipidated LC3B-II species and potentially eS6-P. Finally, imaging of Annexin A1 in fixed WT and RPS25 KO cells demonstrates elevated levels throughout the KO but not WT cells (**Figure 7D** and **Figure 7—FigS4**), though Annexin A1 appeared to not be activated in every cell of the population. The collective results serve to both validate a common, irreversible changes of the RPS25 KO and nominated Annexin A1 as a biomarker for the RPS25 KO cell state.

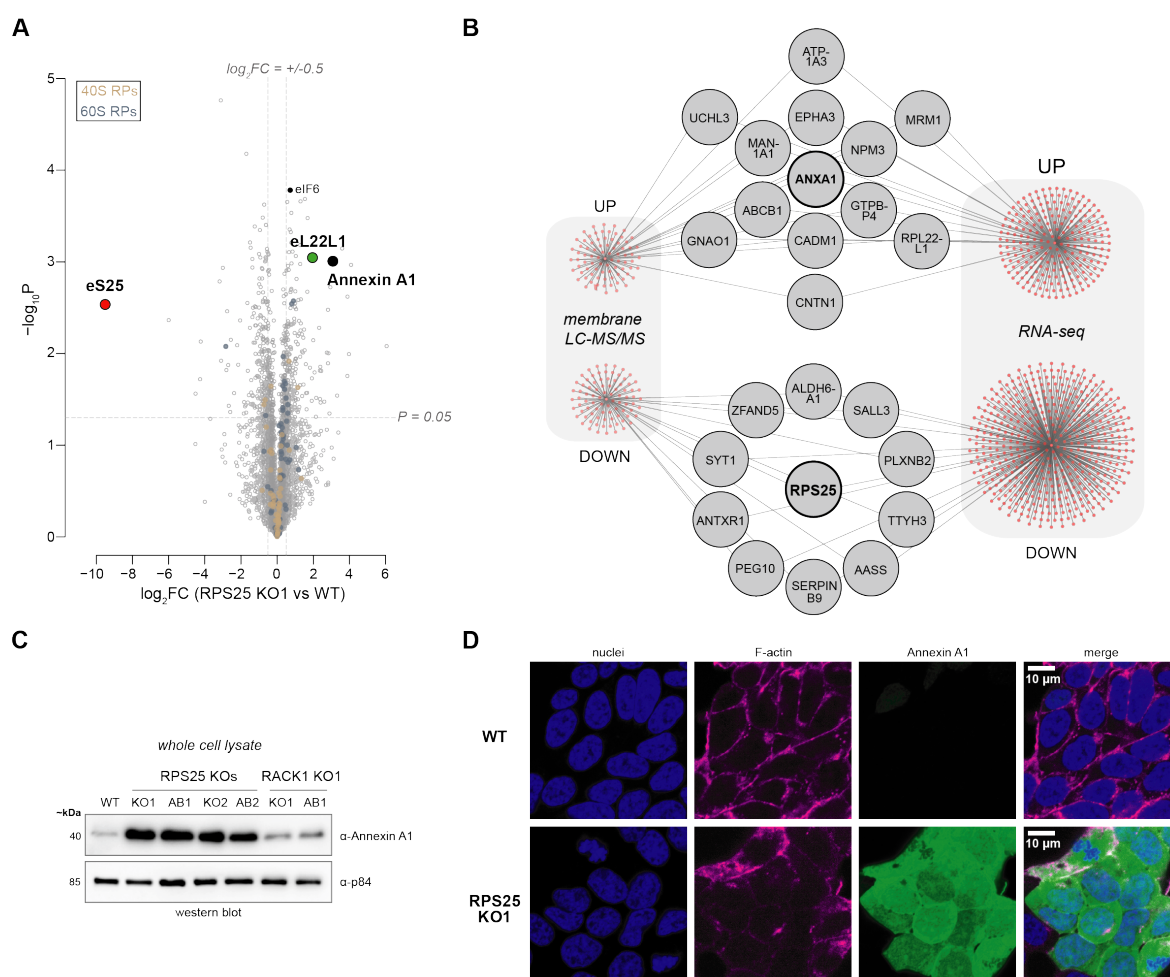


Figure 7 (full-page width). RPS25 KO cells have remodeled membrane proteomes displaying common and irreversibly high Annexin A1 levels. **A.** Volcano plot for fold-changes from LFQ intensities based on mass spectrometry of membrane fractions. Y-axis represents the negative log₁₀ P-values (-log₁₀P-value), while x-axis represents the log₂ fold-change (log₂FC). Values are derived from the results from analysis of three biological replicates for each cell line and a two-tailed heteroscedastic t-test. Select genes are filled in and colored to show top changes. RPs are colored as shown in the figure legend. Select ribosomal and non-ribosomal proteins are annotated. To indicate value cutoffs for subsequent ontology analysis, a horizontal gray line is shown at P=0.05 and vertical gray lines are shown at log₂FC = ±0.5. **B.** Network plot intersecting upregulated and downregulated genes shared between membrane LC-MS/MS and RNA-seq analyses. From the LC-MS/MS data, proteins with log₂FC<-0.5 and >0.5, and P<0.05 were compared. From the RNA-seq data, genes with log₂FC<-0.5 and >0.5, and Padj<0.01 were compared. **C.** Western blot analysis of WT and KO HAP1 cells for Annexin A1 demonstrates specificity to the RPS25 KOs. Blot was performed from whole cell lysate harvested from each cell line under even growth conditions. **D.** Confocal images from IF imaging of WT and RPS25 KO1 HAP1 cells for Annexin A1. Fixed cells were stained with an antibody against Annexin A1 alongside staining of nuclei with Hoescht and F-actin with Phalloidin 660.

Given the recent identification of RPS25 as a modulator of repeat-associated non-AUG (RAN) translation (Yamada et al., 2019), we asked whether such a phenotype might also be irreversible. WT, RPS25 KO1, and RPS25 KO1 expressing RPS25-ybbR (eS25-ybbR AB) cells were transfected with the C9orf72 66-repeat (C9-66R) expression construct and assayed in parallel. In this experiment, we used the eS25-ybbR AB instead of the eS25-HA AB to prevent signal interference between eS25-HA and the HA-tagged polyGA that is expressed from C9-66R. The ybbR tag is an 11 amino acid tag that we've previously used for enzymatic labeling (Johnson et al., 2019), and similar to eS25-HA, we have found that eS25-ybbR

functionally incorporates into ribosomes (not shown). Immunoblotting of cell lysates from each transfected cell line demonstrated a failure of the AB to rescue WT expression levels of one of the RAN translation products, polyGA (**Figure 7—FigS3B**), consistent with an irreversible state change of these cells. Since no clear differences in C9-66R mRNA stability were observed in the previous study (Yamada et al., 2019), these findings motivate future experiments to explore potential post-translational mechanisms of clearance of polyGA that might be activated in the HAP1 RPS25 KO cell line. Additionally, given that reductions in eS25 levels were shown to alter dipeptide repeat levels in yeast, other cell lines, including human iPS cells and iPS-derived motor neurons, and *Drosophila* (Yamada et al., 2019), we cannot exclude the potential role for translation in those conditions. Discerning these mechanisms will require further investigation, but at least in HAP1 cells, appears tied to an irreversible state change.

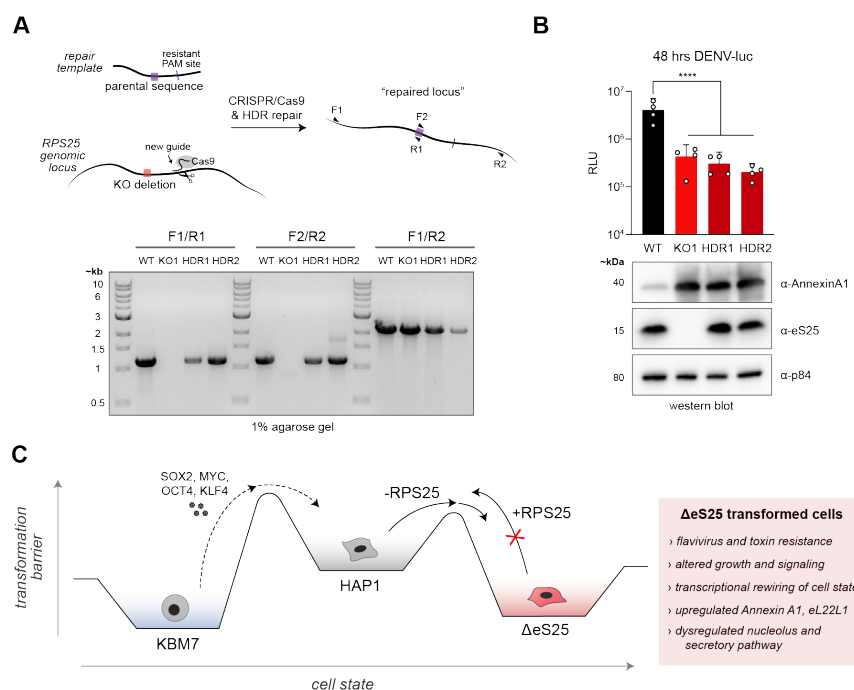
A memory of RPS25 loss cannot be corrected even by repair at the native genomic locus

The word “irreversibility” was used previously to describe the failure of the eS25-HA (or ybbR) AB to rescue cellular phenotypes or gene expression. We felt confident to use this term because of multiple experiments that demonstrated the ability of eS25-HA to express in cells, incorporate into ribosomes, and restore *in vitro* ribosome functionality (*i.e.*, binding to the CrPV IRES). Nevertheless, the HA protein tag could interfere with some but not other functions, the mRNA is expressed from a non-native promoter (CMV), and the mature mRNA is produced without splicing from pre-mRNA. To demonstrate conclusively this irreversibility, we therefore repaired the mutated genomic locus to account for all these variables at once. We designed CRISPR/Cas9 guides targeting regions of the RPS25 locus upstream and downstream of a 6-nt deletion in the RPS25 KO1 clone (**Figure 8—FigS1A,S2A**). The RPS25 KO2 clone, made by gene trap mutagenesis, cannot be as easily repaired due to the size of insertion. To engineer the RPS25 KO1 clone back to its parental sequence, we applied homology-directed repair with CRISPR/Cas9 plasmids encoding these guides, along with homology templates containing the parental RPS25 sequence. Following clone isolation, we screened clones for successful repair using PCR primers designed to specifically amplify the WT allele and identified RPS25 sequence revertants by gel electrophoresis (**Figure 8A**). We isolated revertants by both repair strategies targeting upstream (exon 1—5’UTR) or downstream (intron 1) of the 6-nt deletion. Successful expression of eS25 was identified from PCR positive clones by western blotting cell lysate for eS25, and we amplified and sequenced genomic DNA fragments from positive clones made by both strategies (HDR1 and HDR2, **Figure 8—FigS1B-S2B**). We found that these HDR clones demonstrated repair of the 6-nt deletion at the sequence level, though both left scars at the new guide strand target sites. This was unexpected as we included PAM site mutations in our homology templates, but fortunately neither of the new scars are in the RPS25 coding sequence.

We next asked whether HDR clones responded to infection with DENV-luc like WT or KO cells. We found that all of the clones failed to rescue the sensitivity to DENV-luc infection and further observed that the HDR clones express Annexin A1 at levels similar to the KO (**Figure 8B**). The KO, AB, and HDR clones are thus phenotypically indistinguishable, and this tracks perfectly with the Annexin A1 biomarker. As a result, we conclude that these and other KO phenotypes not rescued by the eS25-HA AB are the product of an irreversible state change following RPS25 loss. We suggest a model for such a state change (**Figure 8C**) and discuss its implication below.

Figure 8 (2/3 page width). RPS25

KO cells have adopted a cell state that cannot be rescued by repair of the genomic locus. **A.** Homology-directed repair (HDR) of the RPS25 KO1 HAP1 cells line. Repair schematic (top) depicts design for RPS25 locus repair by one strategy with a new guide targeting RPS25 intron 1. Agarose gel electrophoresis of PCR fragments from screening for repair clones HDR1 (2B11) and HDR2 (6G11). A 1% agarose gel was run in TAE buffer for 30 min at 150 V with equal volume of each GoTaq PCR reaction, stained with ethidium bromide, and imaged. **B.** Western blot analysis and DENV-luc assay of WT, RPS25 KO1, and RPS25 HDR repair clones. Luciferase values (top) were



DISCUSSION

We propose that a memory of RPS25 loss, as manifested through a cellular state change, drives resistance phenotypes. Such a state change is not unprecedented given that HAP1 cells were originally isolated following an attempt to make a pluripotent haploid cell line by expression of the Yamanaka factors in the near-haploid KBM7 cell line (**Figure 8C**) (Carette et al., 2011). Though not deemed pluripotent, HAP1 cells might display metaplasia similar to other cancer cell lines (Liu et al., 2019), and this cellular plasticity could be both reversible and irreversible. As exhibited by the loss of RACK1, certain genetic perturbations can be readily rescued by cDNA expression, while others such as RPS25 cannot. Remarkably, this irreversible plasticity appears to be specific to RPS25 and not simply due to the loss of any non-essential small subunit RP and associated fitness costs (**Figure 4—FigS2A**). Since RPS25 KOs made by completely different strategies (CRISPR/Cas9 and gene trap insertion) behave similarly, the state change appears to be driven by the true loss of eS25 expression, rather than other potential artifacts from CRISPR/Cas9 insertions and deletions (Tuladhar et al., 2019). The failure of homology-directed repair to rescue the ΔeS25 state change further suggests that neither eS25 protein expression nor pre-translational sensing of RPS25 loss can explain the resistance phenotypes (**Figure 8B**). The many pleiotropic phenotypes observed from RPS25 deletion further supports the existence of a state change, and other genetic mutations in HAP1 cells that give rise to similarly broad pleiotropy (such as EMC2 and DDX6) may have experienced similar transitions (see Phenosaurus resource (Brockmann et al., 2017)). We expect that the ΔeS25 state may be cell-type-

specific given that RPS25 KO have not been reported in other human cell lines, RPS25 has a high essentiality score (see DepMap resource (depmap.org)) and numerous attempts to make the KO in other cell lines (HeLa, Huh7, and HEK293T) in our laboratories have failed. Nevertheless, phenotypes associated with reductions of eS25 levels, such as resistance to ricin toxicity in K562 cells (Bassik et al., 2013), may arise by a similar etiology, especially given that K562 cells can differentiate in culture under certain treatments (Mills et al., 2016). Finally, the fact that RPS25 KO in the budding yeast *S. cerevisiae* drive unique phenotypes and gene expression argues that RPS25 may play an important and conserved role in cell biology (Cheng et al., 2019; Yamada et al., 2019).

How do cells sense RPS25 loss and remember this ribosome irregularity? Our study provides clues to the answer, although several questions still remain. Prior literature has led to an almost synonymous association of RPS25 with IRES-mediated translation (Hertz et al., 2013), and we therefore initially assumed that eS25 acts through specialized translation when its loss is associated with a phenotype. We found that the requirement of eS25 for efficient ribosome recruitment to the CrPV IGR IRES appears to hold but is not generalizable to other IRES types (**Figure 1**). As with RACK1, we found that eS25 is not required for HCV IRES-mediated translation, and we and others have found that the assays that determined this conclusion are confounded by indirect effects (**Figure 2**) (Honda et al., 2000; Huang et al., 2012). Given that the CrPV IGR IRES represents a mechanistically unique IRES type, which mimics an elongation rather than initiation state and utilizes no initiation factors (Johnson et al., 2017), dependence on eS25 should perhaps not be extrapolated to other IRESs. Instead, if eS25 has a direct regulatory role on the translation mechanism, it might be expected to instead function in elongation rather than in the initiation stage, as hinted at by eS25's demonstrated interaction with Z-site tRNA, a likely E-site tRNA ejection intermediate (Brown et al., 2018). The finding that RPS25 loss does not obviously affect flavivirus translation further argues against assuming a direct role of eS25 on specialized translation events (**Figures 4-5**). Thus, translational dysregulation and accompanying proteotoxicity from RPS25 loss may be one aspect of cellular sensing, yet other mechanisms might be given equal weight in consideration.

Is ribosomal heterogeneity a cause or consequence of translational events? The substoichiometric presence of eS25 and other RPs on cellular ribosomes tempts the possibility that such compositional alterations are selected for translational control and participate in cellular functions such as tissue diversification (Shi et al., 2017). Yet it is still unclear how and why a cell would produce such heterogeneity given the complex and energy expensive nature of ribosome biogenesis (Klinge and Woolford, 2019; Peña et al., 2017). Potentially supporting this interpretation, a recent study found that maternal ribosomes are sufficient for embryogenesis in *C. elegans* (Cenik et al., 2019), meaning that functional ribosome heterogeneity in embryonic cell types must occur after assembly and transport. Such post-synthesis heterogeneity may be selected and functional, but it has also not been ruled out whether natural ribosome deficiency of eS25 is a consequence of aberrant translation events. As others have already discussed (Ferretti and Karbstein, 2019), the tagging approach used to isolate certain RP-containing ribosome populations may artificially skew results and only be correlative. In a similar vein, we do not interpret our discovery of the RP paralog remodeling at eL22L1 in the RPS25 KO as direct causality, though it represents an unappreciated aspect of ribosomal heterogeneity that deserves further study.

One potential explanation for phenotypes that result from altered RP levels is a coordinated change in ribosome numbers (Mills and Green, 2017), which have been shown to control human hematopoiesis (Khajuria et al., 2018). The disruption of RP levels in yeast has been further demonstrated to incur cellular fitness costs and gene expression alteration that are distinct for mutations in small and large subunit RPs, which respectively reduce levels of each subunit (Cheng et al., 2019). Our observation that knockout of RPS25 and RACK1 in haploid human cells leads to partially overlapping but distinct phenotypic outcomes indicates that loss of a small subunit RP does not incur a monolithic response. Such an outcome for the RPS25 KO is paralleled by the yeast study, wherein knockout of both alleles of RPS25 led to an unusual response that cannot be explained simply by ribosome numbers (Cheng et al., 2019). Together these results support the idea of there being a unique response incurred by RPS25 loss from yeast to humans, yet it is unclear whether that is sensed through eS25 on or off the ribosome.

Since our findings have not provided strong evidence for eS25-mediated translational control, we hypothesize that the cellular sensing of RPS25 loss arises from another source. Indeed, we observed multiple signatures of dysregulated ribosome biogenesis in the RPS25 KO and no indication of drastically altered RP levels (besides eS25) (**Figure 3, 6-7** and supplements; **Figure 4—FigS2D**), which is supported by findings from the biogenesis literature. In particular, siRNA-mediated knockdown of eS25 in human cells drives a peculiar biogenesis response, wherein unlike other small subunit RP knockdowns, small subunit RP levels do not coordinately change in abundance (O’Donohue et al., 2010; Robledo et al., 2008). Moreover, eS25 is paradoxically found to assemble in early preribosomal particles and is found within the nucleolus, while not altering pre-18S rRNA maturation like other “initiation RPSs” (Kubota et al., 1999; O’Donohue et al., 2010). Similarly, knockdown of RACK1 does not drastically interfere with pre-18S rRNA maturation, though it assembles to early cytoplasmic and not nucleolar preribosomes (Larburu et al., 2016). Thus, similar to the phenotypes observed in our assays, eS25 and RACK1 display partially overlapping but distinct roles in ribosome biogenesis.

RPs do much more than chaperone rRNA maturation concordant with their assembly, and several biogenesis checkpoints exist, providing opportunities for feedback loops to sense proper assembly (Klinge and Woolford, 2019; Peña et al., 2017). The complexity of ribosome biogenesis in eukaryotes is amplified by the existence of the nucleolus—a subnuclear, membraneless organelle that is a key hub for stress sensing (Boulon et al., 2010; Yang et al., 2018). Our RNA-seq analysis highlighted the dysregulation of the nucleolus in the RPS25 KO, and our quantification of the subnuclear intensity of DDX21 supports this assessment (**Figure 6** and **Figure 6—FigS1-2**). Further, though we did not observe elevated levels of eL22L1 within RPS25 KO nuclei, eL22L1 was elevated in mass spectrometry of eS25-deficient cytoplasmic ribosomes and membranes (**Figure 3, Figure 6—FigS2**, and **Figure 7**), suggesting that eL22L1 expression might be a consequence of nuclear architecture reorganization in response to nucleolar stress (Boulon et al., 2010). Perhaps relevant to the “sensing” of cellular eS25 levels is the reported interaction between eS25 and the p53 E3 ligase MDM2, thus stabilizing and activating p53 following ribosomal stress (Zhang et al., 2013). However, we observed WT levels of p53 in the RPS25 KO and no clear indication of p53 target gene transcriptional dysregulation by RNA-seq (**Figure 4—FigS1D**). The stabilization of p53 is a common mechanism for nucleolar stress sensing by orphan RPs (Boulon et al., 2010), and given the specific outcomes of RPS25 loss versus that of other RPs even in yeast that lack p53, we expect that p53 may be only one aspect of a eS25-sensing response. One tempting possibility is that eS25 is sensed as part of a feedback loop that connects early assembly of the ribosome (and hence nucleolar role) with late assembly (and hence its non-essentiality for rRNA maturation). Loss of eS25 could thus be “remembered” through the genomic reorganization that results from a specific subnuclear stress sensing following its loss. Further analysis will be needed to unravel how cells specifically sense and remember eS25 alterations, and we hope that our datasets provides useful roadmaps for such studies.

The complex and critical activity of the ribosome for cellular life dictates that it is both a central hub of proteostasis and a challenge to study at the level of its individual parts. In this study, we set out to study the translational effects of RP loss, but quickly recognized that the primary unaddressed challenge was to decipher the direct and indirect effects that follow RP loss in a cell. We ultimately uncovered a host of indirect effects that appear linked to diverse phenotypes in cells lacking eS25 and RACK1. Our collective findings suggest that the implied role of these proteins in IRES-mediated translation should be refined and led us to rethink the importance of RP-mediated translational control more broadly. Our study of the RPS25 KO illustrates the complexity of cellular adaptation to RP loss and how pleiotropy may arise by a non-intuitive cellular rewiring mechanism. Finally, our findings have implications for gene therapy through the realization that cells can “remember” ribosome irregularities. Though mutations in RPS25 are not currently linked to any ribosomopathies, the hysteresis observed in the RPS25 KO may be a general phenomenon associated with mutations in the translational apparatus and therefore mask a host of indirect effects. If genetic mutations in RPs drive reorganization of nuclear architecture during development, rather than directly interfering with translation, gene therapy-mediated repair of such mutations in somatic cells might ultimately fail. Furthermore, the therapeutic reduction of nucleolar RPs like RPS25 may cause disease if they drive dysregulation of the nucleolus (Boulon et al., 2010; Kampen et al., 2019; Yang et al., 2018).

Altogether, our study highlights the complex cellular outcomes that follow RP loss in a cell and shows that even in the most suggestive cases, customization of the ribosome may not imply translational causality.

ACKNOWLEDGEMENTS

We thank G Hess, M Bassik, and N Ingolia for sharing unpublished data, reagents, and helpful discussions; O Brandman for insightful discussions on the project and manuscript; G Fuchs for sharing the RPS25 expression vectors; C Walczak, K Majzoub, and Puglisi, Carette, and Bertozzi labs members for input. We thank Z Qi at the UCSF Cytogenetics lab for karyotyping analysis; J Perrino and the Stanford CSIF for assistance with transmission electron microscopy (NCRR ARRA Award #1S10RR026780-01); M Weglarz and L Nichols at the Stanford FACS facility for assistance with flow cytometry; and the GSSC for high-throughput sequencing (NIH award S10OD020141). We thank the SRRC for providing computational resources and support via the Sherlock cluster. AGJ was supported by an NSF-GRF (DGE-114747); RAF and CPL are supported by Damon Runyon Cancer Research Foundation fellowships (#2286-17 and #2321-18, respectively); YSO was supported by a Stanford Dean's fellowship; MLZ is supported by a NIH predoctoral fellowship (1F31DK112570-01A1); SBY was supported by a NIHGRI training grant (2T32HG000044-21); and JC was supported by a TARGET ALS Springboard Fellowship. This work was funded by the National Institutes of Health (AI047365 and GM113078 JDP, AG064690 JDP and ADG, and AI141970 to JEC).

COMPETING INTERESTS

The authors declare no competing interests.

METHODS

Cell growth and lentiviral transductions

HAP1 cells were grown at 37°C with 5% CO₂ in Iscove's Modified Dulbecco's medium (IMDM) supplemented with 10% (v/v) heat-inactivated fetal bovine serum, 2 mM L-glutamine, and 1X penicillin/streptomycin. K562 cells were grown at 37°C with 5% CO₂ in RPMI media with 10% (v/v) fetal bovine serum, 2 mM L-glutamine, and 1X penicillin/streptomycin. HEK293FT cells were grown at 37°C with 5% CO₂ in DMEM media with 10% (v/v) fetal bovine serum, 2 mM L-glutamine, and 1X penicillin/streptomycin. Wild-type, RPS25 KO (CRISPR/Cas9 KO1 clone A8-15 (KO1), and gene trap insertion clone 45-1 (KO2)), RACK1 KO (CRISPR/Cas9 clones E3-A5 (KO1) and KO2 E3-A6 (KO2)), and eIF3H KO HAP1 cell lines were used in this study (Carette et al., 2011; Fuchs et al., 2015; Jha et al., 2017; Johnson et al., 2018). Cells lines all tested negative for mycoplasma with the MycoAlter PLUS Mycoplasma Detection Kit (Lonza cat.#LT07-703). Lentivirus packaging was conducted at the Gene Vector and Virus Core of Stanford University or performed in-house using lentiviral constructs by co-transfection with ΔVPR, VSV-G, and pAdVantage packaging plasmids into HEK293FT cells using FuGENE HD (Promega) (Campeau et al., 2009). Cells were transduced and selected as described (Johnson et al., 2018) using constructs in the pLenti CMV PURO vectors expressing RPS25-HA, RPS25-ybbr, or RACK1-FLAG, those described in the literature for expression of RPS10, RPS20, and ZNF598 mutants (gifts from E Bennett) (Sundaramoorthy et al., 2017), and the human IRE1 WT and kinase mutant (hIRE1a wt and K599A, gifts from F Urano, Addgene plasmid #20744 and #20745, respectively) (Lipson et al., 2008). The K562 cell lines bearing RPS25-targeting and control shRNA were gifts from G Hess and M Bassik. The sequence for the RPS25-targeting shRNA is ATCTGAGAGACTGAAGATTCGATAGTGA AGCTTCAGATGTATCGAATCTTCAGTCTCTCAGAG, while the negative control shRNA is ATCGC ACTTAGTAATGATTGAATAGTGAAGCTTCAGATGTATTCAATCATTACTAAGTGCGAG.

Ribosome purifications and polysome profiling

Purification of human 40S and 60S ribosomal subunits and polysome profiling was performed as described (Johnson et al., 2019). Purification of "crude 80S" ribosomes for mass spectrometry was performed by halting purification of ribosomal subunits after resuspending the ribosome pellet from the first sucrose cushion and prior to splitting subunits. For purification of "crude 80S" ribosomes from the K562 cells, the

method was identical except that the cells were pelleted from suspension culture prior to lysis rather than scraping from culture dishes. For purification of monosomes (“mono”) and polysomes (“poly”) from polysome profiles, fractions corresponding to each were pooled from two profiles per cell line. These pooled fractions were then pelleted with a low-salt sucrose cushion (100 mM KOAc, 5 mM MgOAc₂, 30 mM HEPES-KOH pH 7.5, 1 mM DTT) by centrifuging at 63,000 x g for 18 hrs at 4°C using a Type 80 Ti rotor (Beckman Coulter). Pellets were resuspended and analyzed by silver staining and mass spectrometry.

Membrane purification

Purification of cellular membranes (sometimes called “ER membranes” or “ER”) was performed roughly as described (Stephens et al., 2008). Briefly, HAP1 cell lines were grown with regular passages and seeded in single 15-cm dishes in triplicate for each cell line 48 hrs of growth before harvesting at ~80 confluency. To normalize growth conditions prior to harvest, media was removed 6 hrs prior to harvest and replenished with fresh media. Cells were harvested by aspirating media and washing cells on plate 2X with 10 mL pre-chilled PBS. Cells were scraped in residual PBS, pelleted, and then resuspended in 1 mL permeabilization buffer (110 mM KOAc, 2.5 mM MgOAc₂, 25 mM HEPES-KOH pH 7.5, 1 mM EGTA, 0.015% digitonin, 1 mM DTT) per 15-cm plate. Permeabilized cells were incubated for 5 min then centrifuge for 10 min at 1,000 xg. The supernatant was removed and saved “cytosol fraction”, and the pellet was resuspended with 5 mL wash buffer (110 mM KOAc, 2.5 mM MgOAc₂, 25 mM HEPES-KOH pH 7.5, 1 mM EGTA, 0.004% digitonin, 1 mM DTT) and re-pelleted at 1000 xg for 10 min. The wash was removed and the cytosol-vacated pellet was mixed with 250 uL lysis buffer (110 mM KOAc, 2.5 mM MgOAc₂, 25 mM HEPES-KOH pH 7.5, 1% NP-40, 0.5% sodium deoxycholate, 1 mM DTT) and incubated on ice for 5 min. Nuclei were pelleted at 7,500 xg for 10 min, and the supernatant (“membrane fraction”) was saved. Protein concentrations were determined by a Bradford assay and further characterized by mass spectrometry.

Native gel electrophoresis

Acrylamide/agarose composite gels were cast and run as described (Johnson et al., 2018). Complexes were formed with the indicated amounts of ribosomal subunits and labeled RNAs in a buffer containing 30 mM HEPES-KOH (pH 7.4), 100 mM KOAc₂, and 2 mM MgOAc₂, unless otherwise indicated. The HCV IRES RNA was fluorescently labeled at the 3’ end as described (Johnson et al., 2019), and the CrPV IGR IRES A1F construct used previously (Petrov et al., 2016) was transcribed and 3’ end labeled in a similar manner.

Immunoblotting

Except when otherwise stated, western blotting was performed as described (Johnson et al., 2018). When blotting purified 40S ribosomal subunits, an equal concentration of 40S (by A₂₆₀) was loaded into separate wells of the SDS-PAGE gel (10 pmol). When blotting either “crude 80S” ribosomes, post-nuclear cell lysate, or whole cell lysate, respective protein concentrations were determined for each sample with a Bradford assay (BioRad) such that protein concentrations could be normalized. When blotting whole cell lysates, lysate was first treated with DNase I (NEB) to mitigate genomic DNA viscosity when loading into SDS-PAGE gels. When re-probing blots, HRP-conjugated secondary antibodies were either inactivated by incubation with 0.02% sodium azide in 5% skim milk/TBST or stripped with Restore Stripping Buffer (ThermoFisher cat.#21059). Lysate blots were re-probed with anti-p84 and/or anti-GAPDH-HRP as loading controls, while ribosome blots were blotted with antibodies against other ribosomal proteins as appropriate. Most antibodies were used in a block of 5% skim milk in TBST, except the anti-eL22L1 antibodies which were used in a block of 3% BSA in TBST. A list of antibodies used for western blots is in Supplementary Table 1.

Dual-luciferase assays

A dicistronic vector encoding a 5’ cap-driven Renilla luciferase and downstream HCV IRES driven firefly luciferase was used for dual-luciferase assays (Fig. 2). The plasmid was transfected into HAP1 cell lines as described (Johnson et al., 2018) and then cells were lysed and assayed under various conditions and time points, as described in the main text and figures. Under similar conditions, cell lines were assayed with a

Propidium Iodide (PI) FACS-based assay (Abcam cat.#ab139148) to assess the ploidy of each cell line under the conditions indicated. The resulting PI assay data was analyzed in FlowJo to isolate singlets and plot histograms of PI intensity using the BluFL2 photomultiplier tube (PMT) with the 615/25 filter and B615 detector. All statistical analyses were performed in GraphPad Prism.

Mass spectrometry

Purified ribosome subunits were isolated and quantified as described above. 10 µg of protein was used as input material for each digestion. Samples were brought up to 95 µL in 50 mM Ammonium Bicarbonate (AmBic) and reduced with 5 mM DTT for 20 min at 60°C. Samples were cooled to room temperature and then alkylation was achieved by adding 30 mM iodoacetamide for 30 min at 25°C in the dark. To digest peptides, 400 ng of sequencing grade trypsin (Promega) was added for 16 hrs at 37°C. Samples were subsequently acidified by adding formic acid to a final concentration of 2.5% and incubating at 37°C for 45 min. Finally, samples were desalted using HyperSep Filter Plates with a 5-7 µL bed volume (Thermo Fisher Scientific) following the manufacturer's instructions. Samples were eluted three times in 100 µL 80% ACN in 0.2% formic acid, dried on a SpeedVac, and resuspended in 10 µL 0.2% formic acid for mass spectrometry analysis.

Cell membrane fractions from HAP1 cells were purified and quantified as described above. To prepare peptide samples, 10 µg of protein was used as input on S-trap Micro Column (Protifi) as per the manufacturer's protocol. To digest peptides on-column, 750 ng of sequencing grade trypsin (Promega) was added for 1 hr at 48°C. Digested peptides were eluted sequentially with 40 µL of 0.2% formic acid and then 50% ACN in water. Samples were dried on a SpeedVac and resuspended in 10 µL 0.2% formic acid for mass spectrometry analysis.

Samples were analysed by online nanoflow LC-MS/MS using an Orbitrap Fusion Tribrid mass spectrometer (Thermo Fisher) coupled to a Dionex Ultimate 3000 HPLC (ThermoFisher). A portion of the sample was loaded via autosampler isocratically onto a C18 nano pre-column using 0.1% formic acid in water ("Solvent A"). For pre-concentration and desalting, the column was washed with 2% ACN and 0.1% formic acid in water ("loading pump solvent"). Subsequently, the C18 nano pre-column was switched in line with the C18 nano separation column (75 µm x 250 mm EASYSpray (ThermoFisher) containing 2 µm C18 beads) for gradient elution. The column was held at 45°C using a column heater in the EASY-Spray ionization source (ThermoFisher). The samples were eluted at a constant flow rate of 0.3 µL/min using a 90 min gradient and a 140 min instrument method. The gradient profile was as follows (min:% solvent B, 2% formic acid in acetonitrile) 0:3, 3:3, 93:35, 103:42, 104:95, 109:95, 110:3, 140:3. The instrument method used an MS1 resolution of 60,000 at FWHM 400 m/z, an AGC target of 3e5, and a mass range from 300 to 1,500 m/z. Dynamic exclusion was enabled with a repeat count of 3, repeat duration of 10 s, exclusion duration of 10 s. Only charge states 2-6 were selected for fragmentation. MS2s were generated at top speed for 3 s. HCD was performed on all selected precursor masses with the following parameters: isolation window of 2 m/z, 28-30% collision energy, orbitrap (resolution of 30,000) detection, and an AGC target of 1e4 ions. Spectra were used to generate label-free quantitative (LFQ) intensities using MaxQuant and Perseus software, excluding reverse peptides and imputing missing values from a normal distribution (Cox and Mann, 2008; Tyanova et al., 2016). Data from experiments with biological replicates were analysed by a two-tailed heteroscedastic t-test in Excel, after checking that the data was log2 normal. Mass spectrometry results were analysed and plotted in RStudio, significant overlapping changes between conditions were determined and plot using BioVenn (Hulsen et al., 2008), and ontology was performed using data from the Gene Ontology Project powered by Panther (Ashburner et al., 2000; Carbon et al., 2019; Mi et al., 2017). Membrane MS and RNA-seq data was intersected using Cytoscape to produce Figure 7B (Shannon et al., 2003). Supplementary Table 3 contains processed LFQ intensities from MS analyses.

RT-qPCR

Cell lines, as indicated in the main text, were seeded into wells of a 96-well plate at 10,000 cells per well 24-48 hrs prior to lysis, reverse transcription, and amplification with the Cell-to-CT kit (ThermoFisher

cat#4402955). Real-time PCR was performed with the SYBR Green PCR master mix (ThermoFisher cat#4309155) using a CFX Connect Real-Time System (BioRad). In experiments with unperturbed cells, lysis took place 24 hrs post-seeding. In experiments with tunicamycin-treated cells, tunicamycin or DMSO was added to wells 24 hrs post-seeding, and then cells were lysed and assayed after 24 hrs in the presence of drug. Primers used for RT-qPCR are listed in Supplementary Table 2 and data was plot in GraphPad Prism.

Viral infections

All viral infections were performed under appropriate biosafety conditions using viruses titrated by standard plaque assays. The DENV-luc experiments used virus produced from BHK-21 cells, by transfection of an RNA encoding the HAP1-adapted dengue serotype 2 virus (DENV-2) with a Renilla luciferase ORF embedded at the 5' end of the DENV ORF (Marceau et al., 2016). The Coxsackie B3 luciferase (CV-B3-luc, Nancy strain) experiment used virus produced by transfection of the infectious clone pRLuc-53CB3/T7 into RD cells (Lanke et al., 2009). HAP1-adapted DENV-2 virus (clone 16681) was propagated in C6/36 cells or HAP1 cells, Chikungunya virus (CHIKV, 181/25 vaccine strain) was propagated in BHK-21 cells, and Zika virus (ZIKV, PRVABC59 (Human/2015/Puerto Rico, NR-50240)) was propagated in C6/36 cells.

For most DENV-luc infections, cells were seeded into 96-well plates at 10,000 live cells/well, infected 24 hrs after seeding, and then lysed and assayed 24, 48, and/or 72 hrs post-infection. Except when otherwise stated, cells were infected with a low MOI of 0.018. When indicated, cells were treated with the replication inhibitor MK0608 or translation inhibitor cycloheximide (CHX) at 50 μ M and 100 μ M, respectively. For adherent cells, media was directly aspirated from wells at indicated time points, followed by the addition of 100 μ L Renilla Luciferase lysis buffer (Promega cat.#E2810), and appropriate incubation. For suspension cells (K562), cells were transferred to a V-bottom well 96-well plates for low-speed centrifugation prior to aspiration and lysis. Renilla luciferase units (RLU) were measured either by the addition of 20 μ L lysate to 100 μ L Renilla luciferase assay reagent in an eppendorf tube and measuring luminescence using a GloMax 20/20 Single Tube Luminometer with 5 sec integrations, or by sequential addition of 50 μ L Renilla luciferase assay reagent into wells containing 20 μ L lysate and measuring luminescence via a 5 sec integration using a Veritas microplate luminometer in white 96-well plates (Corning cat.#3789A).

For crystal violet staining of cells upon virus infections, cells were seeded at 10,000 live cells per well in a 96-well plate and infected with viruses at the indicated MOIs. At 3 days post-infection, cells were fixed with 4% paraformaldehyde in PBS and viable cells were visualized by crystal violet staining.

To titer the production of DENV-2 infectious particles by plaque assay, HAP1 cell lines were seeded into 6-well plates in triplicate at 250,000 live cells per well. At 24 hrs post-seeding, cells were infected with DENV-2 at MOI=0.1 PFU/cell, and the infection was allowed to proceed for 48 hrs. At the end of the experiment, media from infected cells was collected, and cells were washed with PBS and then lysed on plate with RIPA buffer. The DENV-2 secreted into supernatants harvested from infected cells were subsequently tittered by plaque assays using Huh7.5.1 cells, while the cell lysate was used for immunoblotting with antibodies against DENV proteins (Ooi et al., 2019). All statistical analyses were performed in GraphPad Prism.

Proliferation assays

Proliferation assays were performed roughly as described (Johnson et al., 2018), and modified to include select drug treatments. Briefly, HAP1 cell lines from routine passages were dissociated from culture plates with trypsin and counted for live cells by trypan blue. Cells were then seeded into 96-well plates at 10,000 live cells/well with 3-10 replicates per cell line. 24 hrs after seeding cells, drugs or DMSO was added to respective wells via 2X stocks in media, and then cells were assayed over 4 days of growth using the MTT reagent (ThermoFisher). Since tunicamycin does not have a discrete molecular weight, we approximated it as 840 g/mol to facilitate ease in plotting molar concentrations in Figure 4 (e.g., 0.25 μ g/mL \approx 300 nM). Absorbance values at 570 nm were determined using a Synergy Neo2 instrument (BioTek). All statistical analyses were performed in GraphPad Prism.

Immunofluorescence imaging and analysis

Wild-type, RPS25 KO1, and RPS25 KO2 HAP1 cell line were seeded into a glass bottom 96-well plate (Corning cat.#4580) at 10,000 live cells per well and incubate under standard conditions. 24 hrs after seeding, a portion of cells were infected with HAP1-adapted DENV-2 at MOI=2. The infection was allowed to proceed for 24 hrs, at which point media was aspirated from wells and cells were fixed with 4% PFA in PBS for 15 min at room temperature. Following three washes in PBS, cells were permeabilized with 0.1% triton X-100 in PBS for 15 min, washed again 3X with PBS, and then blocked overnight at 4°C with 5% BSA in PBS. Cells were either immediately stained with antibodies or kept in PBS containing 0.02% sodium azide at 4°C until use. Cells were stained with select antibodies as indicated in the main text and figures, by first incubating in primary antibodies overnight in PBS with 2% BSA at 4°C. Following overnight incubation, cells were washed 3X with PBS, then incubated in PBS with 2% BSA for 2 hrs at 4°C, and washed 3X with PBS prior to imaging. Concurrently with secondary antibody staining, cells were stained with Hoechst 33342 (Invitrogen cat.#H3570) at 0.5 µg/mL and Phalloidin 660 (Invitrogen cat.#A22285) from a methanol stock for a final concentration of 80 nM. A list of antibodies used for immunofluorescence staining is in Supplementary Table 1.

Epi-fluorescent imaging was performed with an ImageXpress Micro XLS Widefield High-Content Analysis System (Molecular Devices) using a 20x Plan Apo objective with 2x camera binning. Confocal imaging was performed with a Nikon A1R HD25 microscope and 60X oil objective using 405, 488, 561, and 640 nm lasers as appropriate. Multiple Z-stacks were acquired for each condition by confocal, and for comparing images across conditions Z planes that transected similar regions of cells were chosen. For comparative image analysis, only images acquired with the same laser settings were compared and the antibody staining channel intensity threshold was maintained constant between conditions when preparing images for figures.

For quantitative image analysis, cellular nuclei were first segmented based on Hoechst staining. Nuclear images were converted to a mask using the minimum error thresholding method. Touching cells were then split using two steps applied in serial. The first step used a marker control watershed approach where the markers were derived from regional maximum values of the nuclear image. In the second step, the watershed image was used to further split cells in contact with their nearest neighbor(s). A custom segmentation algorithm was implemented to detect and bridge concave inflections in the perimeter of each object to separate any remaining touching cells. Resulting objects that were too small, too large, or oddly shaped were not included in further analysis. For signal measurement from each signal channel, a large radius top-hat filter was first applied to subtract the background signal. The nuclear mask image was then used to mark regions of interest to calculate the signal intensity within each cell nucleus. Nuclear immunofluorescence signals were calculated as mean nuclear intensity of the pixels in each cell nucleus. Image analysis was performed using custom scripts written in Matlab (available at https://github.com/algejo/HAP1_nuclei_analysis).

Transmission electron microscopy

Wild-type, RPS25 KO1, and RPS25 KO2 HAP1 cell lines were seeded into a 6-well plate at 500,000 live cells per well. Prior to seeding, a 10x5mm Aclar slab (Ted Pella cat.#10501-10) was deposited in wells to which cells adhered after standard incubation. 24 hrs after seeding, a portion of cells were infected at MOI=2 and the cells were returned to incubation. Following 24 hrs of infection, infected and uninfected cells were fixed by rapidly transferring Aclar slabs into Karnovsky's fixative (2% Glutaraldehyde (EMS cat.#16000) and 4% PFA (EMS cat.#15700) in 0.1M Sodium Cacodylate (EMS cat.#12300) pH 7.4) for 1 hr, chilled and delivered to Stanford's CSIF on ice. They were then post-fixed in cold 1% Osmium tetroxide (EMS cat.#19100) in water and allowed to warm for 2 hrs in a hood, washed 3X with ultra-filtered water, then all together stained for 2 hrs in 1% Uranyl Acetate at room temperature. Samples were then dehydrated with a series of ethanol washes for 10 min each at room temperature beginning at 50%, 70%, 95%, changed to 100% 2X, then Propylene Oxide (PO) for 10 min. Samples were then infiltrated with EMBED-812 resin (EMS cat.#14120) mixed 1:1, and 2:1 with PO for 2 hrs each. The samples were then placed into EMBED-

812 for 2 hrs, opened and then placed into flat molds with labels and fresh resin and placed in a 65°C oven overnight.

Sections were taken around 90nm, picked up on formvar/Carbon coated slot Cu grids, stained for 40 sec in 3.5% Uranyl acetate in 50% acetone followed by staining in 0.2% Lead Citrate for 6 min. Grids were images in a JEOL JEM-1400 120kV microscope and photos were acquired using a Gatan Orius 2k X 2k digital camera.

RNA-seq

HAP1 cell lines were seeded into the wells of 6-well plates with equal live cell counts (250,000 cells/well), grown under standard conditions, and harvested by trypsinization, pelleting and washing cells with PBS 48 hrs post-seeding. To normalize growth conditions prior to harvest, media was removed 6 hrs prior to harvest and replenished with fresh media. RNA was purified from cells pellets using the PureLink RNA mini kit (ThermoFisher cat.#12183025). Prior to library preparation, RNA concentration and sample quality by RNA integrity number (RIN) were checked using TapeStation RNA ScreenTape reagents (Agilent cat.# 5067-5576). cDNA libraries were prepared with the SureSelect Strand-Specific RNA Library Prep Kit (Agilent cat.#G9691B) on an Agilent Bravo Automated Liquid Handling Platform accordingly to the protocol (Version E0, March 2017, G9691-90030). Library concentration and integrity were checked using TapeStation D1000 ScreenTape reagents (Agilent cat.#5067-5582) and the Qubit dsDNA BR Assay Kit (Invitrogen cat.#Q32850). Sequencing was performed on an Illumina HiSeq 4000 with 2x101 base pair reads and Illumina Single Index. Reads were aligned to the hg38 reference genome using STAR v2.5.3a (Dobin et al., 2013) and differential expression between samples was computed using R v3.4.0 and the DESeq2 package (Love et al., 2014) (detailed pipeline and options available on <https://github.com/emc2cube/Bioinformatics/>). In the rare case that fold change P-values were too small for R to calculate and estimated as 0, these were imputed at 10^{-300} to facilitate logarithmic conversion. Most graphics were generated in RStudio, Venn diagrams were prepared using BioVenn (Hulsen et al., 2008) or Venny (Oliveros, 2007), and gene ontology analysis was performed using data from the Gene Ontology Project powered by Panther (Ashburner et al., 2000; Carbon et al., 2019; Mi et al., 2017). Hierarchical clustering was performed by centroid linkage in Cluster 3.0 (Eisen et al., 1998) and heatmaps were visualized in and exported from Java TreeView (Saldanha, 2004). We expect that RPS25 mRNA was at reduced levels in the KO cells due to transcript degradation by nonsense-mediated decay or premature transcriptional termination, and that the RPS25-HA transcript was not detected since our library preparation relied on polyA enrichment and the lentiviral expression instead has a WPRE. Supplementary Table 4 contains processed RNA-seq data with fold-change and P-values for each condition versus WT.

RAN translation experiments

The HA-tagged polyGA dipeptide was expressed from a C9orf72 66-repeat (C9-66R) expression construct, as previously described (Yamada et al., 2019). Briefly, WT, RPS25 KO1, and RPS25 KO1 expressing RPS25-ybbR (eS25-ybbR AB) HAP1 cells were transfected with appropriate constructs using Lipofectamine 3000 and assayed in parallel 72 hrs post-transfection. Transfected cells were lysed with radioimmunoprecipitation assay buffer containing 1X HALT protease (Pierce) and post-nuclear lysate was prepared by centrifugation at 10,000xg for 10 min at 4°C. The lysate was quantified with a BCA assay (Pierce) and equal amounts (20-25 µg) were analyzed by immunoblotting as described (Yamada et al., 2019). In this experiment, the blot was cut into three appropriate sections and blotted for each of three antibodies. Three biological replicates of the RPS25-ybbR rescue experiment were performed (two shown) each with similar results.

Homology-directed genome repair

To repair the six nucleotide deletion at the RPS25 locus in a previously-reported HAP1 knockout clone (Fuchs et al., 2015), we designed CRISPR/Cas9 guide strands targeting sequences upstream and downstream of the deletion, as well as homology templates with the parental sequence (**Figure 8-FigS1-2**). Guide strand oligos were cloned into the PX458 vector (Ann Ran et al., 2013) using digestion-ligation

with the BpiI enzyme. The repair templates were ordered as gene blocks (IDT) and PCR amplified with Phusion polymerase (NEB cat.#M0503S). The RPS25 KO1 cells were seeded into the well of a 6-well plate at 250,000 cells/well and 24 hrs post-seeding the PX458 plasmids and respective homology templates were co-transfected into the RPS25 KO cells using Lipofectamine 3000 (ThermoFisher cat.#L3000075). Transfection was performed following the manufacturer's protocol using 2 µg of each plasmid and template. Cells were dissociated from plates 48 hrs post-transfection, passed through a 70 µm strainer (Falcon cat.#352350), and single GFP-positive cells were sorted into 96-well plates containing 50% conditioned media. Clones were identified ~2 weeks after sorting and screened by genomic DNA extraction with Quickextract (Lucigen cat.#QE09050) and parental allele-specific PCR probes and GoTaq Green Master Mix (Promega cat.#M712). Clones that tested positive by PCR were further validated by western blotting for eS25, followed by amplifying genomic DNA fragments with Platinum PCR Supermix HiFi (ThermoFisher cat.#12532016) and Sanger sequencing. Validated clones were finally characterized by dengue virus infections, as previously described. All oligos used for guide strand cloning, repair template production, and genomic DNA screening are listed in Supplementary Table 2.

DATA AVAILABILITY

The RNA-seq data is being deposited at NCBI GEO and processed RNA-seq and mass spectrometry data are available in Supplementary Tables 3 and 4.

REFERENCES

- Ann Ran F, Hsu PD, Wright J, Agarwala V, Scott DA, Zhang F. 2013. Genome engineering using the CRISPR-Cas9 system. *Nature*.
- Ban N, Beckmann R, Cate JHD, Dinman JD, Dragon F, Ellis SR, Lafontaine DLJ, Lindahl L, Liljas A, Lipton JM, McAlear MA, Moore PB, Noller HF, Ortega J, Panse VG, Ramakrishnan V, Spahn CMT, Steitz TA, Tchorzewski M, Tollervey D, Warren AJ, Williamson JR, Wilson D, Yonath A, Yusupov M. 2014. A new system for naming ribosomal proteins. *Curr Opin Struct Biol*. doi:10.1016/j.sbi.2014.01.002
- Bassik MC, Kampmann M, Lebbink RJ, Wang S, Hein MY, Poser I, Weibezahn J, Horlbeck MA, Chen S, Mann M, Hyman AA, Leproust EM, McManus MT, Weissman JS. 2013. A systematic mammalian genetic interaction map reveals pathways underlying ricin susceptibility. *Cell* **152**:909–922. doi:10.1016/j.cell.2013.01.030
- Beaupere C, Dinatto L, Wasko BM, Chen RB, VanValkenburg L, Kiflezghi MG, Lee MB, Promislow DEL, Dang W, Kaeberlein M, Labunskyy VM. 2018. Genetic screen identifies adaptive aneuploidy as a key mediator of ER stress resistance in yeast. *Proc Natl Acad Sci U S A* **115**:9586–9591. doi:10.1073/pnas.1804264115
- Blomen VA, Májek P, Jae LT, Bigenzahn JW, Nieuwenhuis J, Staring J, Sacco R, Van Diemen FR, Olk N, Stukalov A, Marceau C, Janssen H, Carette JE, Bennett KL, Colinge J, Superti-Furga G, Brummelkamp TR. 2015. Gene essentiality and synthetic lethality in haploid human cells. *Science* (80-) **350**:1092–1096. doi:10.1126/science.aac7557
- Boulon S, Westman BJ, Hutten S, Boisvert FM, Lamond AI. 2010. The Nucleolus under Stress. *Mol Cell* **40**:216–227. doi:10.1016/j.molcel.2010.09.024
- Brockmann M, Blomen VA, Nieuwenhuis J, Stickel E, Raaben M, Bleijerveld OB, Altelaar AFM, Jae LT, Brummelkamp TR. 2017. Genetic wiring maps of single-cell protein states reveal an off-switch for GPCR signalling. *Nature* **546**:307–311. doi:10.1038/nature22376
- Brown A, Baird MR, Yip MCJ, Murray J, Shao S. 2018. Structures of translationally inactive mammalian ribosomes. *Elife*. doi:10.7554/eLife.40486
- Campeau E, Ruhl VE, Rodier F, Smith CL, Rahmberg BL, Fuss JO, Campisi J, Yaswen P, Cooper PK, Kaufman PD. 2009. A versatile viral system for expression and depletion of proteins in mammalian cells. *PLoS One* **4**:e6529. doi:10.1371/journal.pone.0006529
- Carette JE, Raaben M, Wong AC, Herbert AS, Obernosterer G, Mulherkar N, Kuehne AI, Kranzusch PJ, Griffin AM, Ruthel G, Cin PD, Dye JM, Whelan SP, Chandran K, Brummelkamp TR. 2011. Ebola

- virus entry requires the cholesterol transporter Niemann-Pick C1. *Nature* **477**:340–343. doi:10.1038/nature10348
- Cenik ES, Meng X, Tang NH, Hall RN, Arribere JA, Cenik C, Jin Y, Fire A. 2019. Maternal Ribosomes Are Sufficient for Tissue Diversification during Embryonic Development in *C. elegans*. *Dev Cell* **48**:811–826.e6. doi:10.1016/j.devcel.2019.01.019
- Chan EM, Shibue T, McFarland JM, Gaeta B, Ghandi M, Dumont N, Gonzalez A, McPartlan JS, Li T, Zhang Y, Bin Liu J, Lazaro JB, Gu P, Pieltz CG, Apffel A, Ali SO, Deasy R, Keskula P, Ng RWS, Roberts EA, Reznichenko E, Leung L, Alimova M, Schenone M, Islam M, Maruvka YE, Liu Y, Roper J, Raghavan S, Giannakis M, Tseng YY, Nagel ZD, D’Andrea A, Root DE, Boehm JS, Getz G, Chang S, Golub TR, Tsherniak A, Vazquez F, Bass AJ. 2019. WRN helicase is a synthetic lethal target in microsatellite unstable cancers. *Nature* **568**:551–556. doi:10.1038/s41586-019-1102-x
- Cheng Z, Mugler CF, Keskin A, Hodapp S, Chan LYL, Weis K, Mertins P, Regev A, Jovanovic M, Brar GA. 2019. Small and Large Ribosomal Subunit Deficiencies Lead to Distinct Gene Expression Signatures that Reflect Cellular Growth Rate. *Mol Cell* **73**:36–47.e10. doi:10.1016/j.molcel.2018.10.032
- Cox J, Mann M. 2008. MaxQuant enables high peptide identification rates, individualized p.p.b.-range mass accuracies and proteome-wide protein quantification. *Nat Biotechnol*. doi:10.1038/nbt.1511
- Dice JF, Schimke RT. 1972. Turnover and exchange of ribosomal proteins from rat liver. *J Biol Chem* **247**:98–111.
- Dobin A, Davis CA, Schlesinger F, Drenkow J, Zaleski C, Jha S, Batut P, Chaisson M, Gingeras TR. 2013. STAR: Ultrafast universal RNA-seq aligner. *Bioinformatics*. doi:10.1093/bioinformatics/bts635
- Edgil D, Polacek C, Harris E. 2006. Dengue Virus Utilizes a Novel Strategy for Translation Initiation When Cap-Dependent Translation Is Inhibited. *J Virol* **80**:2976–2986. doi:10.1128/jvi.80.6.2976-2986.2006
- Fernández IS, Bai XC, Murshudov G, Scheres SHW, Ramakrishnan V. 2014. Initiation of translation by cricket paralysis virus IRES requires its translocation in the ribosome. *Cell* **157**:823–831. doi:10.1016/j.cell.2014.04.015
- Ferretti MB, Karbstein K. 2019. Does functional specialization of ribosomes really exist? *Rna* **25**:521–538. doi:10.1261/rna.069823.118
- Fraser JE, Rawlinson SM, Heaton SM, Jans DA. 2016. Dynamic Nucleolar Targeting of Dengue Virus Polymerase NS5 in Response to Extracellular pH. *J Virol* **90**:5797–5807. doi:10.1128/jvi.02727-15
- Fuchs G, Petrov AN, Marceau CD, Popov LM, Chen J, O’Leary SE, Wang R, Carette JE, Sarnow P, Puglisi JD. 2015. Kinetic pathway of 40S ribosomal subunit recruitment to hepatitis C virus internal ribosome entry site. *Proc Natl Acad Sci* **112**:319–325. doi:10.1073/pnas.1421328111
- Gallo S, Ricciardi S, Manfrini N, Pesce E, Oliveto S, Mancino M, Maffioli E, Moro M, Crosti M, Bombaci M, Tedeschi G, Biffo S. 2018. RACK1 Specifically Regulates Translation through its Binding to Ribosomes. *Mol Cell Biol* **38**:e00230-18. doi:10.1128/MCB.00230-18
- Ghandi M, Huang FW, Jané-Valbuena J, Kryukov G V., Lo CC, McDonald ER, Barretina J, Gelfand ET, Bielski CM, Li H, Hu K, Andreev-Drakhlin AY, Kim J, Hess JM, Haas BJ, Aguet F, Weir BA, Rothberg M V., Paolella BR, Lawrence MS, Akbani R, Lu Y, Tiv HL, Gokhale PC, de Weck A, Mansour AA, Oh C, Shih J, Hadi K, Rosen Y, Bistline J, Venkatesan K, Reddy A, Sonkin D, Liu M, Lehar J, Korn JM, Porter DA, Jones MD, Golji J, Caponigro G, Taylor JE, Dunning CM, Creech AL, Warren AC, McFarland JM, Zamanighomi M, Kauffmann A, Stransky N, Imielinski M, Maruvka YE, Cherniack AD, Tsherniak A, Vazquez F, Jaffe JD, Lane AA, Weinstock DM, Johannessen CM, Morrissey MP, Stegmeier F, Schlegel R, Hahn WC, Getz G, Mills GB, Boehm JS, Golub TR, Garraway LA, Sellers WR. 2019. Next-generation characterization of the Cancer Cell Line Encyclopedia. *Nature*. doi:10.1038/s41586-019-1186-3
- Gilbert W V. 2011. Functional specialization of ribosomes? *Trends Biochem Sci* **36**:127–132. doi:10.1016/j.tibs.2010.12.002
- Hafirassou ML, Meertens L, Delaugerre C, Labeau A, Vidalain P-O, Dejarnac O, Umaña-Diaz C,

- Bonnet-Madin L, Kümmerer BM, Roingeard P, Amara A. 2017. A Global Interactome Map of the Dengue Virus NS1 Identifies Virus Restriction and Dependency Host Factors. *Cell Rep* **21**:3900–3913. doi:10.1016/j.celrep.2017.11.094
- Heijnen HF, van Wijk R, Pereboom TC, Goos YJ, Seinen CW, van Oirschot BA, van Dooren R, Gastou M, Giles RH, van Solinge W, Kuijpers TW, Gazda HT, Bierings MB, Da Costa L, MacInnes AW. 2014. Ribosomal Protein Mutations Induce Autophagy through S6 Kinase Inhibition of the Insulin Pathway. *PLoS Genet* **10**. doi:10.1371/journal.pgen.1004371
- Hertz MI, Landry DM, Willis AE, Luo G, Thompson SR. 2013. Ribosomal Protein S25 Dependency Reveals a Common Mechanism for Diverse Internal Ribosome Entry Sites and Ribosome Shunting. *Mol Cell Biol* **33**:1016–1026. doi:10.1128/mcb.00879-12
- Higgins R, Gendron JM, Rising L, Mak R, Webb K, Kaiser SE, Zuzow N, Riviere P, Yang B, Fenech E, Tang X, Lindsay SA, Christianson JC, Hampton RY, Wasserman SA, Bennett EJ. 2015. The Unfolded Protein Response Triggers Site-Specific Regulatory Ubiquitylation of 40S Ribosomal Proteins. *Mol Cell* **59**:35–49. doi:10.1016/j.molcel.2015.04.026
- Honda M, Kaneko S, Matsushita E, Kobayashi K, Abell GA, Lemon SM. 2000. Cell Cycle Regulation of Hepatitis C Virus Internal Ribosomal Entry Site-Directed Translation **118**:152–162.
- Huang JY, Su WC, Jeng KS, Chang TH, Lai MMC. 2012. Attenuation of 40S ribosomal subunit abundance differentially affects host and HCV translation and suppresses HCV replication. *PLoS Pathog* **8**. doi:10.1371/journal.ppat.1002766
- Jeppesen DK, Fenix AM, Franklin JL, Higginbotham JN, Zhang Q, Zimmerman LJ, Liebler DC, Ping J, Liu Q, Evans R, Fissell WH, Patton JG, Rome LH, Burnette DT, Coffey RJ. 2019. Reassessment of Exosome Composition. *Cell* **177**:428–445.e18. doi:10.1016/j.cell.2019.02.029
- Jha S, Rollins MG, Fuchs G, Procter DJ, Hall EA, Cozzolino K, Sarnow P, Savas JN, Walsh D. 2017. Trans-kingdom mimicry underlies ribosome customization by a poxvirus kinase. *Nature* **546**:651–655. doi:10.1038/nature22814
- Johnson AG, Grosely R, Petrov AN, Puglisi JD. 2017. Dynamics of IRES-mediated translation. *Philos Trans R Soc B Biol Sci* **372**:20160177. doi:10.1098/rstb.2016.0177
- Johnson AG, Lapointe CP, Wang J, Corsepis NC, Choi J, Fuchs G, Puglisi JD. 2019. RACK1 on and off the ribosome. *RNA* **25**:881–895. doi:10.1261/rna.071217.119
- Johnson AG, Petrov AN, Fuchs G, Majzoub K, Grosely R, Choi J, Puglisi JD. 2018. Fluorescently-tagged human eIF3 for single-molecule spectroscopy. *Nucleic Acids Res* **46**. doi:10.1093/nar/gkx1050
- Juszkiewicz S, Hegde RS. 2017. Initiation of Quality Control during Poly(A) Translation Requires Site-Specific Ribosome Ubiquitination. *Mol Cell* **65**:743–750. doi:10.1016/j.molcel.2016.11.039
- Kampen KR, Sulima SO, Verecke S, De Keersmaecker K. 2019. Hallmarks of ribosomopathies. *Nucleic Acids Res* **1**–16. doi:10.1093/nar/gkz637
- Kearse MG, Ireland JA, Prem SM, Chen AS, Ware VC. 2013. RpL22e, but not RpL22e-like-PA, is SUMOylated and localizes to the nucleoplasm of Drosophila meiotic spermatocytes. *Nucl (United States)* **4**. doi:10.4161/nucl.25261
- Khajuria RK, Munschauer M, Ulirsch JC, Fiorini C, Ludwig LS, McFarland SK, Abdulhay NJ, Specht H, Keshishian H, Mani DR, Jovanovic M, Ellis SR, Fulco CP, Engreitz JM, Schütz S, Lian J, Gripp KW, Weinberg OK, Pinkus GS, Gehrke L, Regev A, Lander ES, Gazda HT, Lee WY, Panse VG, Carr SA, Sankaran VG. 2018. Ribosome Levels Selectively Regulate Translation and Lineage Commitment in Human Hematopoiesis. *Cell* **173**:90–103.e19. doi:10.1016/j.cell.2018.02.036
- Klinge S, Woolford JL. 2019. Ribosome assembly coming into focus. *Nat Rev Mol Cell Biol* **20**:116–131. doi:10.1038/s41580-018-0078-y
- Kubota S, Copeland TD, Pomerantz RJ. 1999. Nuclear and nucleolar targeting of human ribosomal protein S25: Common features shared with HIV-1 regulatory proteins. *Oncogene* **18**:1503–1514. doi:10.1038/sj.onc.1202429
- Lancaster AM, Jan E, Sarnow P. 2006. Initiation factor-independent translation mediated by the hepatitis C virus internal ribosome entry site. *Rna* **12**:894–902. doi:10.1261/rna.2342306
- Landry DM, Hertz MI, Thompson SR. 2009. RPS25 is essential for translation initiation by the

- Dicistroviridae and hepatitis C viral IRESs. *Genes Dev.* doi:10.1101/gad.1832209
- Lanke KHW, van der Schaar HM, Belov GA, Feng Q, Duijsings D, Jackson CL, Ehrenfeld E, van Kuppeveld FJM. 2009. GBF1, a Guanine Nucleotide Exchange Factor for Arf, Is Crucial for Cocksackievirus B3 RNA Replication. *J Virol.* doi:10.1128/jvi.01244-09
- Larburu N, Montellese C, O'Donohue MF, Kutay U, Gleizes PE, Plisson-Chastang C. 2016. Structure of a human pre-40S particle points to a role for RACK1 in the final steps of 18S rRNA processing. *Nucleic Acids Res* **44**:8465–78. doi:10.1093/nar/gkw714
- Lee JS, Tabata K, Twu W-I, Rahman SM, Kim HS, Yu JB, Jee MH, Bartenschlager R, Jang SK. 2019. RACK1 mediates rewiring of intracellular networks induced by hepatitis C virus infection. *PLOS Pathog* **15**:e1008021.
- Li Q, Brass AL, Ng A, Hu Z, Xavier RJ, Liang TJ, Elledge SJ. 2009. A genome-wide genetic screen for host factors required for hepatitis C virus propagation. *Proc Natl Acad Sci U S A* **106**:16410–16415. doi:10.1073/pnas.0907439106
- Lipson KL, Ghosh R, Urano F. 2008. The role of IRE1 α in the degradation of insulin mRNA in pancreatic β -cells. *PLoS One.* doi:10.1371/journal.pone.0001648
- Liu Y, Deisenroth C, Zhang Y. 2016. RP-MDM2-p53 Pathway: Linking Ribosomal Biogenesis and Tumor Surveillance. *Trends in Cancer.* doi:10.1016/j.trecan.2016.03.002
- Liu Y, Mi Y, Mueller T, Kreibich S, Williams EG, Van Drogen A, Borel C, Frank M, Germain PL, Bludau I, Mehnert M, Seifert M, Emmenlauer M, Sorg I, Bezrukov F, Bena FS, Zhou H, Dehio C, Testa G, Saez-Rodriguez J, Antonarakis SE, Hardt WD, Aebersold R. 2019. Multi-omic measurements of heterogeneity in HeLa cells across laboratories. *Nat Biotechnol* **37**:314–322. doi:10.1038/s41587-019-0037-y
- Majzoub K, Hafirassou ML, Meignin C, Goto A, Marzi S, Fedorova A, Verdier Y, Vinh J, Hoffmann JA, Martin F, Baumert TF, Schuster C, Imler JL. 2014. RACK1 controls IRES-mediated translation of viruses. *Cell* **159**:1086–1095. doi:10.1016/j.cell.2014.10.041
- Marceau CD, Puschnik AS, Majzoub K, Ooi YS, Brewer SM, Fuchs G, Swaminathan K, Mata MA, Elias JE, Sarnow P, Carette JE. 2016. Genetic dissection of Flaviviridae host factors through genome-scale CRISPR screens. *Nature.* doi:10.1038/nature18631
- Mauro VP, Edelman GM. 2002. The ribosome filter hypothesis. *Proc Natl Acad Sci* **99**:12031–12036. doi:10.1073/pnas.192442499
- McCann KL, Baserga SJ. 2013. Genetics. Mysterious ribosomopathies. *Science* **341**:849–50. doi:10.1126/science.1244156
- McDonald ER, de Weck A, Schlabach MR, Billy E, Mavrikakis KJ, Hoffman GR, Belur D, Castelletti D, Frias E, Gampa K, Golji J, Kao I, Li L, Megel P, Perkins TA, Ramadan N, Ruddy DA, Silver SJ, Sovath S, Stump M, Weber O, Widmer R, Yu J, Yu K, Yue Y, Abramowski D, Ackley E, Barrett R, Berger J, Bernard JL, Billig R, Brachmann SM, Buxton F, Caothien R, Caushi JX, Chung FS, Cortés-Cros M, deBeaumont RS, Delaunay C, Desplat A, Duong W, Dwoske DA, Eldridge RS, Farsidjani A, Feng F, Feng JJ, Flemming D, Forrester W, Galli GG, Gao Z, Gauter F, Gibaja V, Haas K, Hattenberger M, Hood T, Hurov KE, Jagani Z, Jenal M, Johnson JA, Jones MD, Kapoor A, Korn J, Liu J, Liu Q, Liu S, Liu Y, Loo AT, Macchi KJ, Martin T, McAllister G, Meyer A, Mollé S, Pagliarini RA, Phadke T, Repko B, Schouwey T, Shanahan F, Shen Q, Stamm C, Stephan C, Stucke VM, Tiedt R, Varadarajan M, Venkatesan K, Vitari AC, Wallroth M, Weiler J, Zhang J, Mickanin C, Myer VE, Porter JA, Lai A, Bitter H, Lees E, Keen N, Kauffmann A, Stegmeier F, Hofmann F, Schmelzle T, Sellers WR. 2017. Project DRIVE: A Compendium of Cancer Dependencies and Synthetic Lethal Relationships Uncovered by Large-Scale, Deep RNAi Screening. *Cell* **170**:577–592.e10. doi:10.1016/j.cell.2017.07.005
- Mills EW, Green R. 2017. Ribosomopathies: There's strength in numbers. *Science (80-)* **358**. doi:10.1126/science.aan2755
- Mills EW, Wangen J, Green R, Ingolia NT. 2016. Dynamic Regulation of a Ribosome Rescue Pathway in Erythroid Cells and Platelets. *Cell Rep* **17**:1–10. doi:10.1016/j.celrep.2016.08.088
- Muhs M, Yamamoto H, Ismer J, Takaku H, Nashimoto M, Uchiumi T, Nakashima N, Mielke T,

- Hildebrand PW, Nierhaus KH, Spahn CMT. 2011. Structural basis for the binding of IRES RNAs to the head of the ribosomal 40S subunit. *Nucleic Acids Res* **39**:5264–5275. doi:10.1093/nar/gkr114
- Muto A, Sugihara Y, Shibakawa M, Oshima K, Matsuda T, Nadano D. 2018. The mRNA-binding protein Serbp1 as an auxiliary protein associated with mammalian cytoplasmic ribosomes. *Cell Biochem Funct*. doi:10.1002/cbf.3350
- Neufeldt CJ, Cortese M, Acosta EG, Bartenschlager R. 2018. Rewiring cellular networks by members of the Flaviviridae family. *Nat Rev Microbiol* **16**:125–142. doi:10.1038/nrmicro.2017.170
- Nielsen MH, Flygaard RK, Jenner LB. 2017. Structural analysis of ribosomal RACK1 and its role in translational control. *Cell Signal* **35**:272–281. doi:10.1016/j.cellsig.2017.01.026
- Nishiyama T, Yamamoto H, Uchiumi T, Nakashima N. 2007. Eukaryotic ribosomal protein RPS25 interacts with the conserved loop region in a dicistroviral intergenic internal ribosome entry site. *Nucleic Acids Res* **35**:1514–1521. doi:10.1093/nar/gkl1121
- O'Donohue MF, Choismel V, Faublader M, Fichant G, Gleizes PE. 2010. Functional dichotomy of ribosomal proteins during the synthesis of mammalian 40S ribosomal subunits. *J Cell Biol* **190**:853–866. doi:10.1083/jcb.201005117
- O'Leary MN, Schreiber KH, Zhang Y, Duc ACE, Rao S, Hale JS, Academia EC, Shah SR, Morton JF, Holstein CA, Martin DB, Kaeberlein M, Ladiges WC, Fink PJ, MacKay VL, Wiest DL, Kennedy BK. 2013. The Ribosomal Protein Rpl22 Controls Ribosome Composition by Directly Repressing Expression of Its Own Paralog, Rpl22l1. *PLoS Genet*. doi:10.1371/journal.pgen.1003708
- Olbrich T, Mayor-Ruiz C, Vega-Sendino M, Gomez C, Ortega S, Ruiz S, Fernandez-Capetillo O. 2017. A p53-dependent response limits the viability of mammalian haploid cells. *Proc Natl Acad Sci U S A* **114**:9367–9372. doi:10.1073/pnas.1705133114
- Ooi YS, Majzoub K, Flynn RA, Mata MA, Diep J, Li JK, van Buuren N, Rumachik N, Johnson AG, Puschnik AS, Marceau CD, Mlera L, Grabowski JM, Kirkegaard K, Bloom ME, Sarnow P, Bertozzi CR, Carette JE. 2019. An RNA-centric dissection of host complexes controlling flavivirus infection. *Nat Microbiol*. doi:10.1038/s41564-019-0518-2
- Osowski CM, Urano F. 2011. Measuring ER stress and the unfolded protein response using mammalian tissue culture system, 1st ed, Methods in Enzymology. Elsevier Inc. doi:10.1016/B978-0-12-385114-7.00004-0
- Otto GA, Puglisi JD. 2004. The pathway of HCV IRES-mediated translation initiation. *Cell* **119**:369–380. doi:10.1016/j.cell.2004.09.038
- Peña C, Hurt E, Panse VG. 2017. Eukaryotic ribosome assembly, transport and quality control. *Nat Struct Mol Biol*. doi:10.1038/nsmb.3454
- Perera N, Miller JL, Zitzmann N. 2017. The role of the unfolded protein response in dengue virus pathogenesis. *Cell Microbiol* **19**:1–9. doi:10.1111/cmi.12734
- Petrov A, Grosely R, Chen J, O'Leary SE, Puglisi JD. 2016. Multiple Parallel Pathways of Translation Initiation on the CrPV IRES. *Mol Cell* **62**:92–103. doi:10.1016/j.molcel.2016.03.020
- Petrova E, Gracias S, Beauclair G, Tangy F, Jouvenet N. 2019. Uncovering flavivirus host dependency factors through a genome-wide gain-of-function screen. *Viruses* **11**. doi:10.3390/v11010068
- Pisareva VP, Pisarev A V., Fernández IS. 2018. Dual tRNA mimicry in the cricket paralysis virus IRES uncovers an unexpected similarity with the hepatitis C virus IRES. *Elife* **7**:1–15. doi:10.7554/eLife.34062
- Robledo S, Idol RA, Crimmins DL, Ladenson JH, Mason PJ, Bessler M. 2008. The role of human ribosomal proteins in the maturation of rRNA and ribosome production. *RNA*. doi:10.1261/rna.1132008
- Shannon P, Markiel A, Ozier O, Baliga NS, Wang JT, Ramage D, Amin N, Schwikowski B, Ideker T. 2003. Cytoscape: A software Environment for integrated models of biomolecular interaction networks. *Genome Res*. doi:10.1101/gr.1239303
- Sheikh MH, Solito E. 2018. Annexin A1: Uncovering the many talents of an old protein. *Int J Mol Sci*. doi:10.3390/ijms19041045
- Shi Y, Yang Y, Hoang B, Bardeleben C, Holmes B, Gera J, Lichtenstein A. 2016. Therapeutic potential

- of targeting IRES-dependent c-myc translation in multiple myeloma cells during ER stress. *Oncogene* **35**:1015–1024. doi:10.1038/onc.2015.156
- Shi Z, Fujii K, Kovary KM, Genuth NR, Röst HL, Teruel MN, Barna M. 2017. Heterogeneous Ribosomes Preferentially Translate Distinct Subpools of mRNAs Genome-wide. *Mol Cell* **67**:71–83.e7. doi:10.1016/j.molcel.2017.05.021
- Song Y, Mugavero J, Stauft CB. 2019. Dengue and Zika Virus 5' Untranslated Regions Harbor Internal Ribosome Entry Site Functions. *MBio* **10**:1–16.
- Steffen KK, McCormick MA, Pham KM, Mackay VL, Delaney JR, Murakami CJ, Kaeberlein M, Kennedy BK. 2012. Ribosome deficiency protects against ER stress in *Saccharomyces cerevisiae*. *Genetics* **191**:107–118. doi:10.1534/genetics.111.136549
- Stephens SB, Dodd RD, Lerner RS, Pyhtila BM, Nicchitta C V. 2008. Analysis of mRNA partitioning between the cytosol and endoplasmic reticulum compartments of mammalian cells. *Methods Mol Biol.* doi:10.1007/978-1-59745-033-1_14
- Sundaramoorthy E, Leonard M, Mak R, Liao J, Fulzele A, Bennett EJ. 2017. ZNF598 and RACK1 Regulate Mammalian Ribosome-Associated Quality Control Function by Mediating Regulatory 40S Ribosomal Ubiquitylation. *Mol Cell* **65**:751–760. doi:10.1016/j.molcel.2016.12.026
- Tai AW, Benita Y, Peng LF, Kim SS, Sakamoto N, Xavier RJ, Chung RT. 2009. A Functional Genomic Screen Identifies Cellular Cofactors of Hepatitis C Virus Replication. *Cell Host Microbe* **5**:298–307. doi:10.1016/j.chom.2009.02.001
- Tesina P, Lessen LN, Buschauer R, Cheng J, Wu CC, Berninghausen O, Allen R, Becker T, Beckmann R, Green R. 2019. Molecular mechanism of translational stalling by inhibitory codon combinations and poly(A) tracts. *bioRxiv* 1–24.
- Tiwary AK, Cecilia D. 2017. Kinetics of the association of dengue virus capsid protein with the granular component of nucleolus. *Virology* **502**:48–55. doi:10.1016/j.virol.2016.12.013
- Tuladhar R, Yeu Y, Piazza JT, Tan Z, Clemenceau JR, Wu X, Barrett Q, Herbert J, Mathews D, Kim J, Hwang TH, Lum L. 2019. CRISPR/Cas9-based mutagenesis frequently provokes on-target mRNA misregulation. *bioRxiv* 583138. doi:10.1101/583138
- Tyanova S, Temu T, Sinitcyn P, Carlson A, Hein MY, Geiger T, Mann M, Cox J. 2016. The Perseus computational platform for comprehensive analysis of (prote)omics data. *Nat Methods*. doi:10.1038/nmeth.3901
- Tye BW, Commins N, Ryazanova L V., Wühr M, Springer M, Pincus D, Churchman LS. 2019. Proteotoxicity from aberrant ribosome biogenesis compromises cell fitness. *Elife* **8**:1–29. doi:10.7554/eLife.43002
- Van De Waterbeemd M, Tamara S, Fort KL, Damoc E, Franc V, Bieri P, Itten M, Makarov A, Ban N, Heck AJR. 2018. Dissecting ribosomal particles throughout the kingdoms of life using advanced hybrid mass spectrometry methods. *Nat Commun* **9**:e2493. doi:10.1038/s41467-018-04853-x
- Walczak CP, Leto DE, Zhang L, Riepe C, Muller RY, DaRosa PA, Ingolia NT, Elias JE, Kopito RR. 2019. Ribosomal protein RPL26 is the principal target of UFMylation. *Proc Natl Acad Sci* **116**:1299–1308. doi:10.1073/pnas.1816202116
- Wang J, Zhou J, Yang Q, Grayhack EJ. 2018. Multi-protein bridging factor 1(Mbf1), Rps3 and Asc1 prevent stalled ribosomes from frameshifting. *Elife* **7**:1–26. doi:10.7554/eLife.39637
- Welsch S, Miller S, Romero-Brey I, Merz A, Bleck CKE, Walther P, Fuller SD, Antony C, Krijnse-Locker J, Bartenschlager R. 2009. Composition and Three-Dimensional Architecture of the Dengue Virus Replication and Assembly Sites. *Cell Host Microbe* **5**:365–375. doi:10.1016/j.chom.2009.03.007
- Xue S, Barna M. 2012. Specialized ribosomes: A new frontier in gene regulation and organismal biology. *Nat Rev Mol Cell Biol.* doi:10.1038/nrm3359
- Yamada SB, Gendron TF, Niccoli T, Genuth NR, Grosely R, Shi Y, Glaria I, Kramer NJ, Nakayama L, Fang S, Dinger TJI, Thoeng A, Rocha G, Barna M, Puglisi JD, Partridge L, Ichida JK, Isaacs AM, Petrucelli L, Gitler AD. 2019. RPS25 is required for efficient RAN translation of C9orf72 and other neurodegenerative disease-associated nucleotide repeats. *Nat Neurosci.* doi:10.1038/s41593-019-

0455-7

- Yamamoto H, Unbehaun A, Loerke J, Behrmann E, Collier M, Bürger J, Mielke T, Spahn CMT. 2014. Structure of the mammalian 80S initiation complex with initiation factor 5B on HCV-IRES RNA. *Nat Struct Mol Biol* **21**:721–727. doi:10.1038/nsmb.2859
- Yang K, Yang J, Yi J. 2018. Nucleolar Stress: hallmarks, sensing mechanism and diseases. *Cell Stress* **2**:125–140. doi:10.15698/cst2018.06.139
- Yu C-Y, Hsu Y-W, Liao C-L, Lin Y-L. 2006. Flavivirus Infection Activates the XBP1 Pathway of the Unfolded Protein Response To Cope with Endoplasmic Reticulum Stress. *J Virol* **80**:11868–11880. doi:10.1128/jvi.00879-06
- Yu Y, Ji H, Doudna JA, Leary JA. 2009. Mass spectrometric analysis of the human 40S ribosomal subunit: Native and HCV IRES-bound complexes. *Protein Sci* **14**:1438–1446. doi:10.1110/ps.041293005
- Zhang X, Wang W, Wang H, Wang MH, Xu W, Zhang R. 2013. Identification of ribosomal protein S25 (RPS25)-MDM2-p53 regulatory feedback loop. *Oncogene* **32**:2782–2791. doi:10.1038/onc.2012.289
- Zhang Y, O’Leary MN, Peri S, Wang M, Zha J, Melov S, Kappes DJ, Feng Q, Rhodes J, Amieux PS, Morris DR, Kennedy BK, Wiest DL. 2017. Ribosomal Proteins Rpl22 and Rpl22l1 Control Morphogenesis by Regulating Pre-mRNA Splicing. *Cell Rep* **18**:545–556. doi:10.1016/j.celrep.2016.12.034
- Zhu JF, Huang W, Yi HM, Xiao T, Li JY, Feng J, Yi H, Lu SS, Li XH, Lu RH, He QY, Xiao ZQ. 2018. Annexin A1-suppressed autophagy promotes nasopharyngeal carcinoma cell invasion and metastasis by PI3K/AKT signaling activation. *Cell Death Dis* **9**. doi:10.1038/s41419-018-1204-7

Supplementary Figures for “A memory of RPS25 loss drives resistance phenotypes”

Authors

Alex G. Johnson^{1,2,6}, Ryan A. Flynn³, Christopher P. Lapointe¹, Yaw Shin Ooi⁴, Michael L. Zhao², Shizuka B. Yamada⁵, Julien Couthouis⁵, Aaron D. Gitler⁵, Jan E. Carette⁴, and Joseph D. Puglisi^{1,6}

Affiliations

¹ Department of Structural Biology, Stanford University School of Medicine, Stanford, CA 94305

² Department of Chemical and Systems Biology, Stanford University School of Medicine, Stanford, CA 94305

³ Department of Chemistry, Stanford University, Stanford, CA 94305

⁴ Department of Microbiology & Immunology, Stanford University, Stanford, CA 94305

⁵ Department of Genetics, Stanford University, Stanford, CA 94305

⁶ Corresponding authors: algejohn@stanford.edu, puglisi@stanford.edu

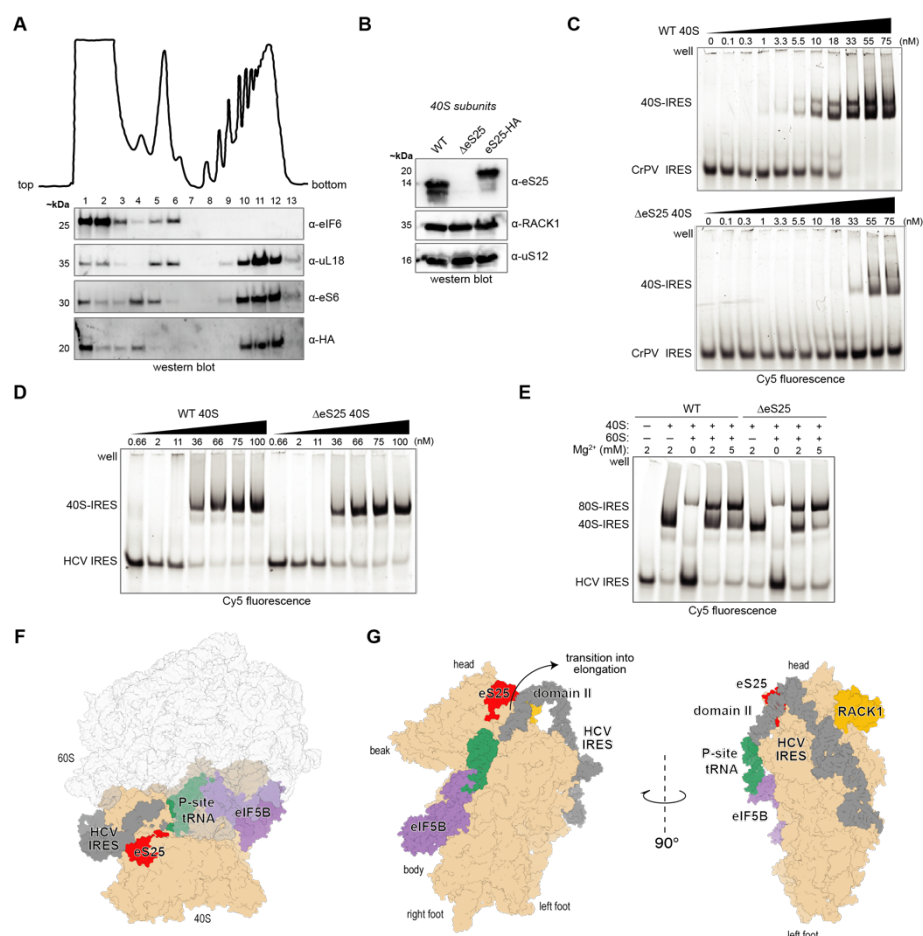
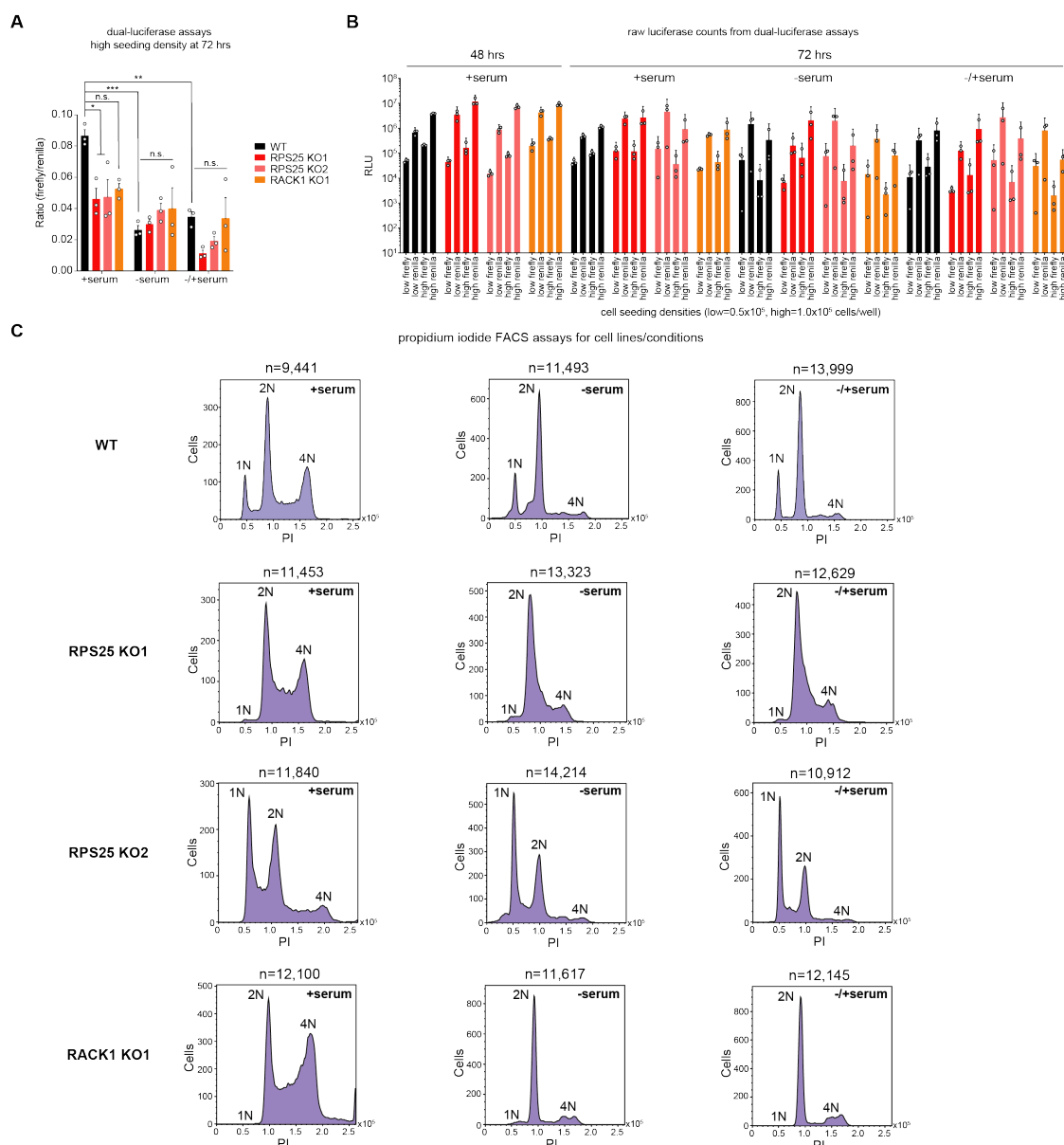


Figure 1—Figure Supplement 1. eS25 is not required for direct recruitment to the HCV IRES nor subsequent large subunit joining under magnesium-driven conditions. **A.** Polysome profile trace from RPS25 KO HAP1 cells that have been transduced with a lentiviral vector encoding the RPS25-HA cDNA (eS25-HA addback (AB)). Post-nuclear lysate was sedimented in 10-60% sucrose gradients, the top and bottom of the gradients are indicated, and the height of peaks is proportional to the absorbance at 254 nm. Fractions were probed for various translation proteins by immunoblotting analysis. The HA antibody used here is from Abcam. **B.** Western blot of purified 40S ribosomal subunits confirms successful incorporation of eS25-HA into human ribosomes. The same ribosome samples were used for gel shifts in Figure 1B. **C.** Binding of WT and Δ eS25 40S ribosomes to the CrPV IGR IRES by native gel electrophoresis. All binding reactions included 30 nM fluorescently labeled IRES RNA. **D.** Binding of WT and Δ eS25 40S ribosomes to the HCV IRES by native gel electrophoresis. Gels as in (C) but with fluorescently labeled HCV IRES RNA. **E.** Formation of 80S-HCV IRES complexes under high magnesium concentrations. Complexes were formed using 60 nM 40S with or without 120 nM 60S and resolved on an acrylamide-agarose composite gel. **F.** Structural model depicting the position of eS25 with respect to the large and small ribosomal subunits in the 80S-HCV IRES-eIF5B-Met-tRNAi-GMPPNP complex (PDB 4ujd). The small subunit is colored tan, the large subunit white, eS25 red, RACK1 is orange, the HCV IRES gray, P-site Met-tRNAi green, and eIF5B purple. **G.** Reorientation of the 80S-IRES model from (F) omitting the 60S subunit to show a similar 40S orientation as in Figure 1A. Left orientation shows the 40S subunit interface, indicating factor and tRNA positions and the rearrangement of HCV IRES domain II during the transition to elongation. The right panel shows the solvent-exposed surface of the 40S subunit (or backside) with the position of RACK1 at the head region making no direct contacts to the HCV IRES.



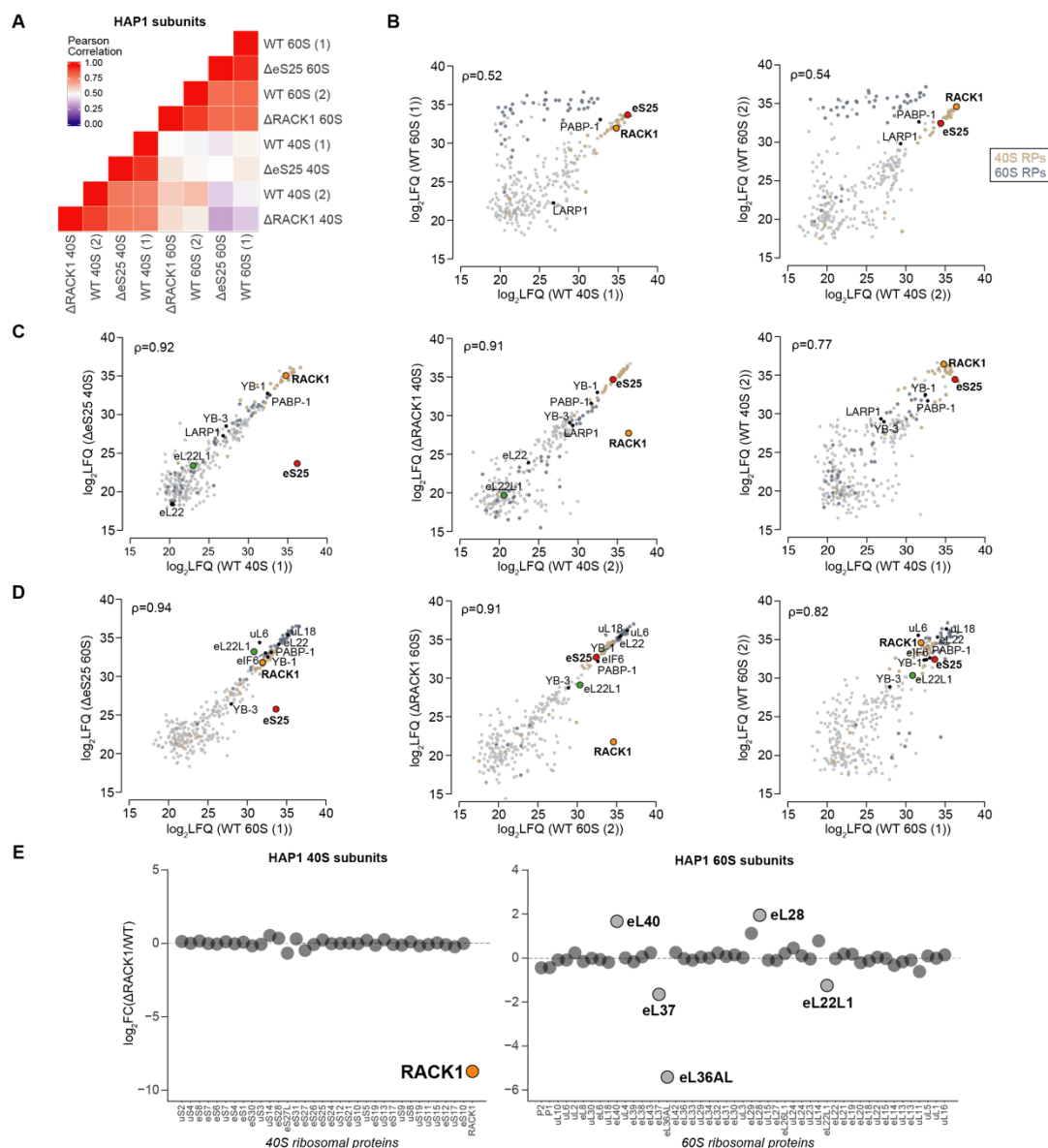


Figure 3—Figure Supplement 1. Mass spectrometry of eS25 and RACK1-deficient ribosomes. **A.** Heatmap of Pearson correlation coefficients (ρ) for log₂LFQ intensities from each HAP1 ribosomal subunit samples. WT (1) was purified in parallel (paired) with the ΔeS25 sample, while WT (2) was paired to the ΔRACK1 sample. **B.** Plot of log₂ LFQ intensities of 60S versus 40S subunits for WT (1) and (2) samples. **C.** Plots of log₂ LFQ intensities from mutant versus WT 40S subunit samples isolated from RPS25 KO1 (ΔeS25) and RACK1 KO1 (ΔRACK1) cell lines in paired experiments. **D.** Plots of log₂ LFQ intensities from mutant versus WT 60S subunit samples isolated from RPS25 KO1 (ΔeS25) and RACK1 KO1 (ΔRACK1) cell lines in paired experiments. For B-D, RPs are colored as indicated and select ribosomal and non-ribosomal proteins are annotated. **E.** Plot of the log₂ fold-change in LFQ intensities between ΔRACK1 and WT ribosomal subunits. Plot is as in Figure 3A with select outlier RPs annotated.

40

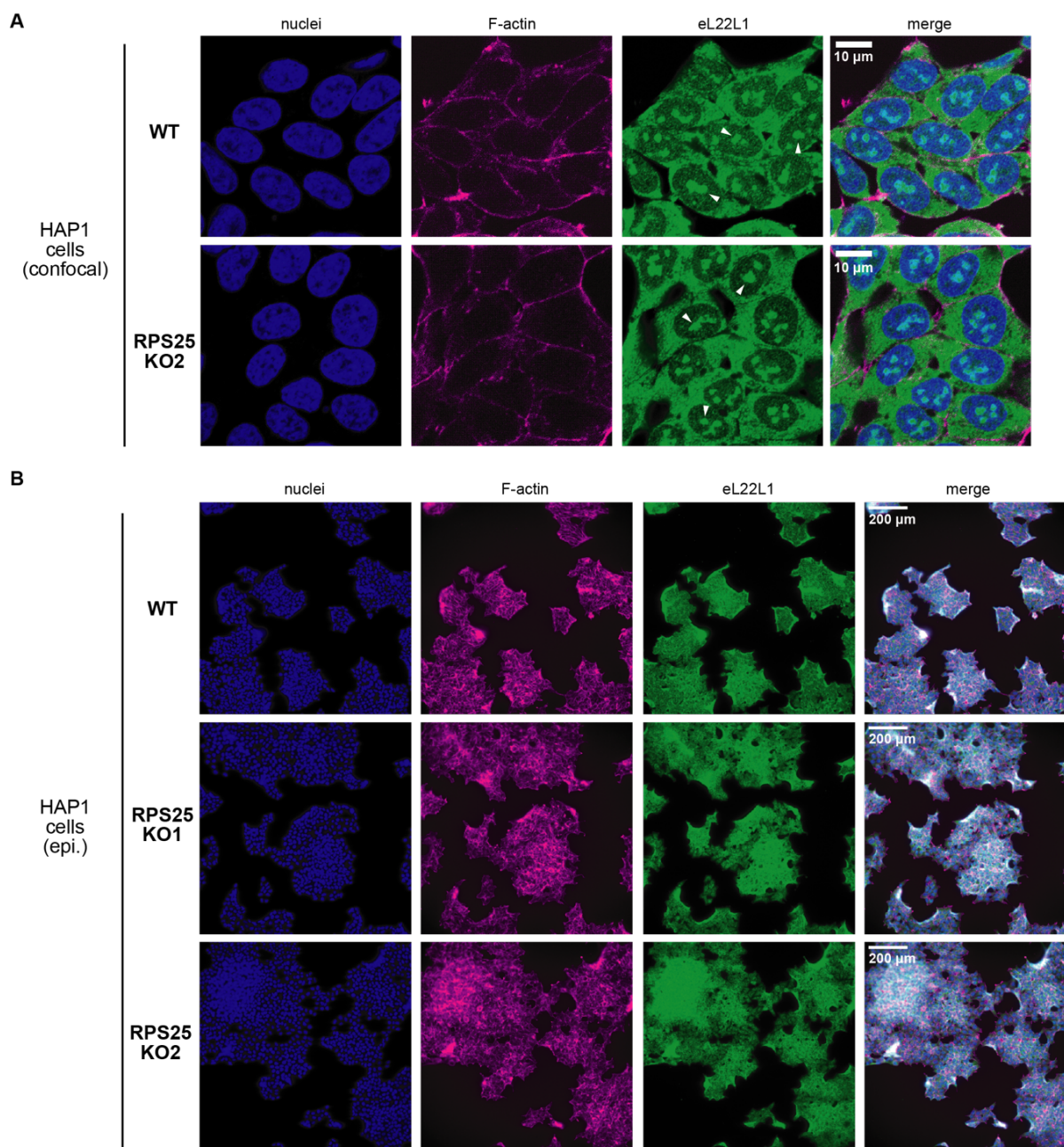


Figure 3—Figure Supplement 3. Immunofluorescent imaging of WT and RPS25 KO HAP1 cells for eL22L1. Cells were fixed and then stained with an antibody targeting eL22L1, as well as the Hoescht stain for nuclei and Phalloidin 660 for F-actin. **A.** Confocal imaging of WT and RPS25 KO2 HAP1 cells (to complement images in Figure 1 of RPS25 KO1 cells). White arrows point to the nucleolar staining of eL22L1 within cells. **B.** Epi-fluorescent imaging of WT and RPS25 KO cells to demonstrate widefield images of the same samples imaged by confocal microscopy.

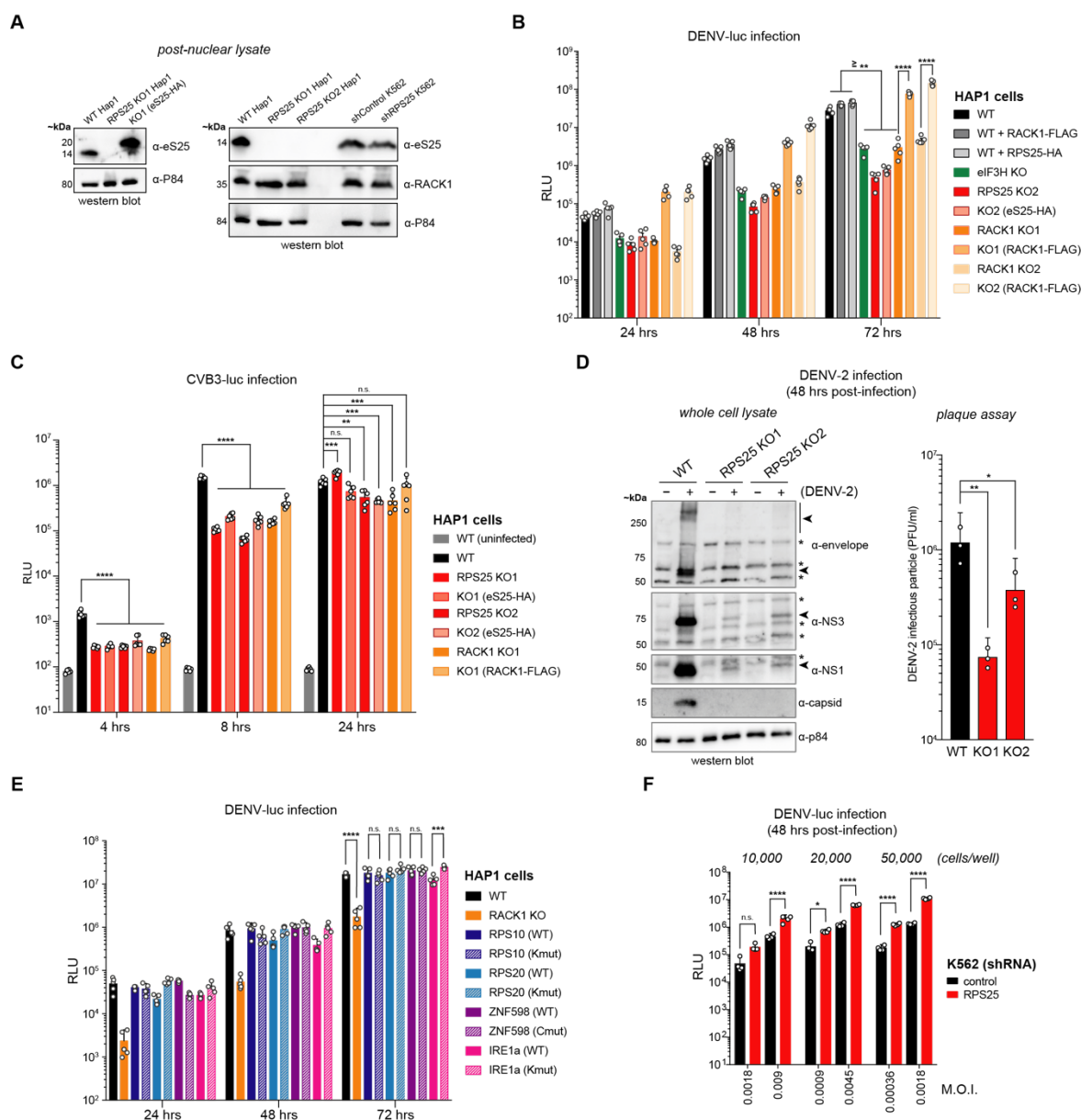


Figure 4—Figure Supplement 1. Viral infections of cells lines demonstrate that the RPS25 KO effect is robust and specific to the HAP1 cell lines and flaviviruses. **A.** Western blot analysis of HAP1 and K562 post-nuclear lysate samples to confirm eS25 depletion or restoration under various conditions. The post-nuclear lysate samples were isolated during the purification of “crude 80S” ribosomes. **B.** Additional example of a DENV-luc infection experiment assayed at 24, 48, and 72 hours post-infection with the DENV-luc virus at a MOI of 0.018 (similar to Figure 4C). Example shows that the RACK1 KO effect is consistent in two clonal KOs and that a loss in cell fitness (eIF3H KO) may also contribute to a loss in infectivity. Error bars represent the 95% CI of n=5 biological replicates and a one-way ANOVA was performed for each time point, correcting for multiple comparisons with a Tukey test. For simplicity, plot only shows significance values for 72 hrs post-infection. P-values: ≥ 0.05 (n.s.), 0.01-0.05 (*), 0.001-0.01 (**), 0.0001-0.001 (***), and <0.0001 (****). **C.** CVB3-luc infection of HAP1 cells lines at multiple time points detects a modest decrease in luciferase activity at early time points. To mitigate issues from cell death at later time points, the 24-hour time point received MOI=0.1, while the 4 and 8-hour time points received MOI=1. Error bars represent the 95% CI of n=6 biological replicates and statistical significance was determined with a one-way ANOVA and Tukey test for each time point. **D.** Western blot analysis (left) and plaque assay (right) from infection with DENV-2 at MOI=0.1 and harvest at 48 hours post-infection. Whole cell lysates were harvested with RIPA buffer and used in blots that probed with

antibodies targeting DENV proteins. * indicates likely nonspecific protein bands. Plaque assay was performed using the virion-containing supernatant as described in the Methods section. The error bars in the plaque assay represent the 95% CI of three biological replicates. The number of infectious particles was compared between WT and KO cell lines using a one-way ANOVA with a Dunnett test to account for multiple comparisons. **E.** DENV-luc infection of HAP1 cell lines with perturbations to RP ubiquitination and the UPR. WT and RACK1 KO1 HAP1 cell lines were used in this assay, as well as WT cells that had been transduced with various lentiviruses. Error bars represent the 95% CI of n=5 biological replicates and statistical significance was determined with a one-way ANOVA and Tukey test for each time point. **F.** DENV-luc infection of K562 cells harboring lentiviral integrated constructs encoding shRNA guides targeting RPS25 or a non-targeting control. Cells were infected at multiple seeding densities and with multiple MOIs as indicated above and below the plot, respectively. Error bars represent the 95% CI and statistical significance was determined with a one-way ANOVA and Tukey test for each time point. This exact experiments in B-F were each performed on one occasion.

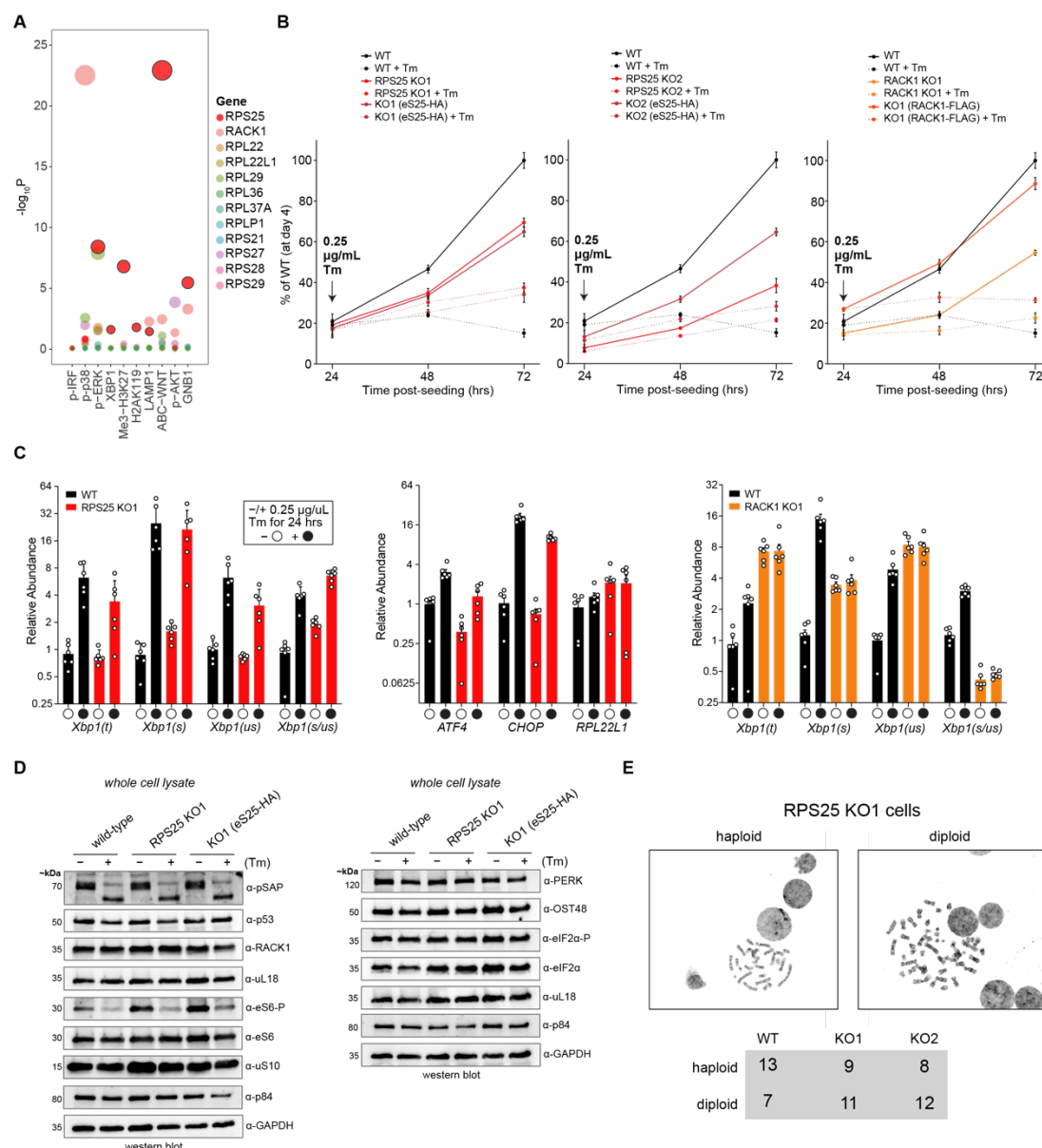


Figure 4—Figure Supplement 2. RPS25 loss promotes pleiotropic phenotypes that include resistance to tunicamycin-mediated cell death. **A.** Plot of significance scores (negative log₁₀ FDR-corrected P-values, $-\log_{10}P$) for RP genes with low essentiality scores from ten published HAP1 FACS-based genetic screens (Blomen et al., 2015; Brockmann et al., 2017). **B.** MTT proliferation assays of WT HAP1 cells versus RPS25 KO1, RPS25 KO2, and RACK1 KO1 with their respective ABs. Data from the left two panels represents the data that was modified for Figure 4E. Error bars for all panels represent the 95% CI of $n=5$ biological replicates. **C.** The RPS25 KO has a responsive UPR. RT-qPCR assays of WT, RPS25 KO1, and RACK1 KO1 HAP1 cells assayed for Xbp1 splicing, other UPR markers (ATF4 and CHOP), and RPL22L1 (primer set 2). Markers were normalized to 18S rRNA expression and y-axis expression is represented on a log₂ scale. Left plot represents a biologically independent example of the same experiment performed in Figure 4F, middle plot represents the amplification of the same RNA samples for other markers, and the right plot represents the amplification of WT and RACK1 KO1 samples with Xbp1 splicing probes. The left and right plots relative abundances are normalized to WT Xbp1(us) at 1, while the middle panel relative abundance is normalized to WT ATF4 at 1. The RACK1 KO1 displays an observably distinct Xbp1 splicing response to the Tm stimulus, but in all cases statistical significance was not detected. Error bars represent the 95% CI of $n=5$ biological replicates. **D.** Western blots of cellular lysates treated with or without 0.25 $\mu\text{g/mL}$ Tm as in Figure 4G, now probed for other ribosomal proteins (RACK1, RPL5/uL18, RPS6/eS6, RPS6-P/eS6-P, RPS20/uS10), the p53 tumor suppressor, an STT3A-specific

glycosylated protein (pSAP), an OST complex protein (OST48), another UPR marker (PERK), as well as phosphorylated and total alpha subunit of eIF2 (eIF2 α -P and eIF2 α). The blotting results indicate little evidence of ribosome level alterations in the RPS25 KO, stable levels of p53, intact OST and STT3A-specific glycosylation, and relatively unaltered PERK branch of the UPR. The consistently high levels of p53 and eIF2 α -P in all cell lines was surprising and was not rigorously evaluated to confirm specificity. **E.** Karyotyping of WT and RPS25 KO cells by the UCSF Cytogenetic Core Laboratory. Twenty single cells from each cell lines were evaluated and the number of haploid and diploid cells in each population are tabulated in the bottom gray box. The upper microscope viewfields are representative images of haploid and diploid cells from the RPS25 KO1 cell line.

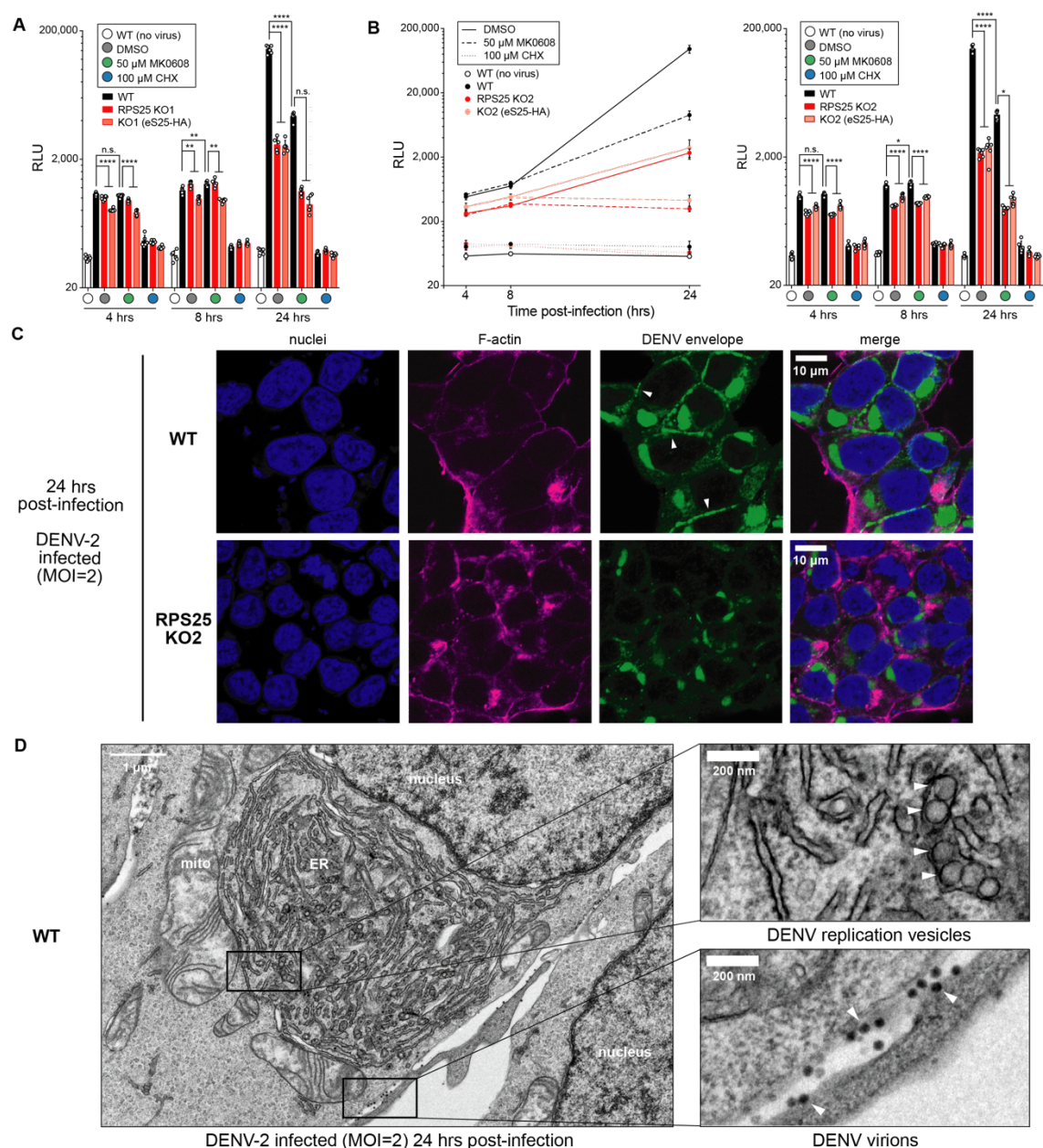


Figure 5—Figure Supplement 1. DENV resistance of the RPS25 KO acts at a late stage of infection when translation and replication are coupled. **A.** Full data for the time course of DENV-luc infection shown in Figure 5A, now showing individual data points and statistical significance for all time points. Error bars represent the 95% CI of $n=6$ biological replicates and data were analyzed with a two-way ANOVA with Tukey test as in Figure 5A. **B.** Time course of DENV-luc infection in WT, RPS25 KO2, and eS25-HA AB cells. Experiment performed for RPS25 KO2 cells as in Figure 5A. P-values: ≥ 0.05 (n.s.), 0.01-0.05 (*), 0.001-0.01 (**), and <0.0001 (****). **C.** Confocal images from IF staining of WT and RPS25 KO2 HAP1 cells infected with DENV-2 at MOI=2. Fixed cells were stained as in Figure 5C. White arrows point to bead-like structures of the E protein within the cell periphery of infected WT cells that is largely absent from KO cells. **D.** TEM images of a WT HAP1 cell section prepared following infections with DENV-2 at MOI=2. Upper right panels is an inset showing the appearance of ER membrane-derived replication vesicles (same image as Figure 5D, white arrows). The bottom right panel represents another inset of the left panel, with white arrows pointing to virions at the cell membrane.

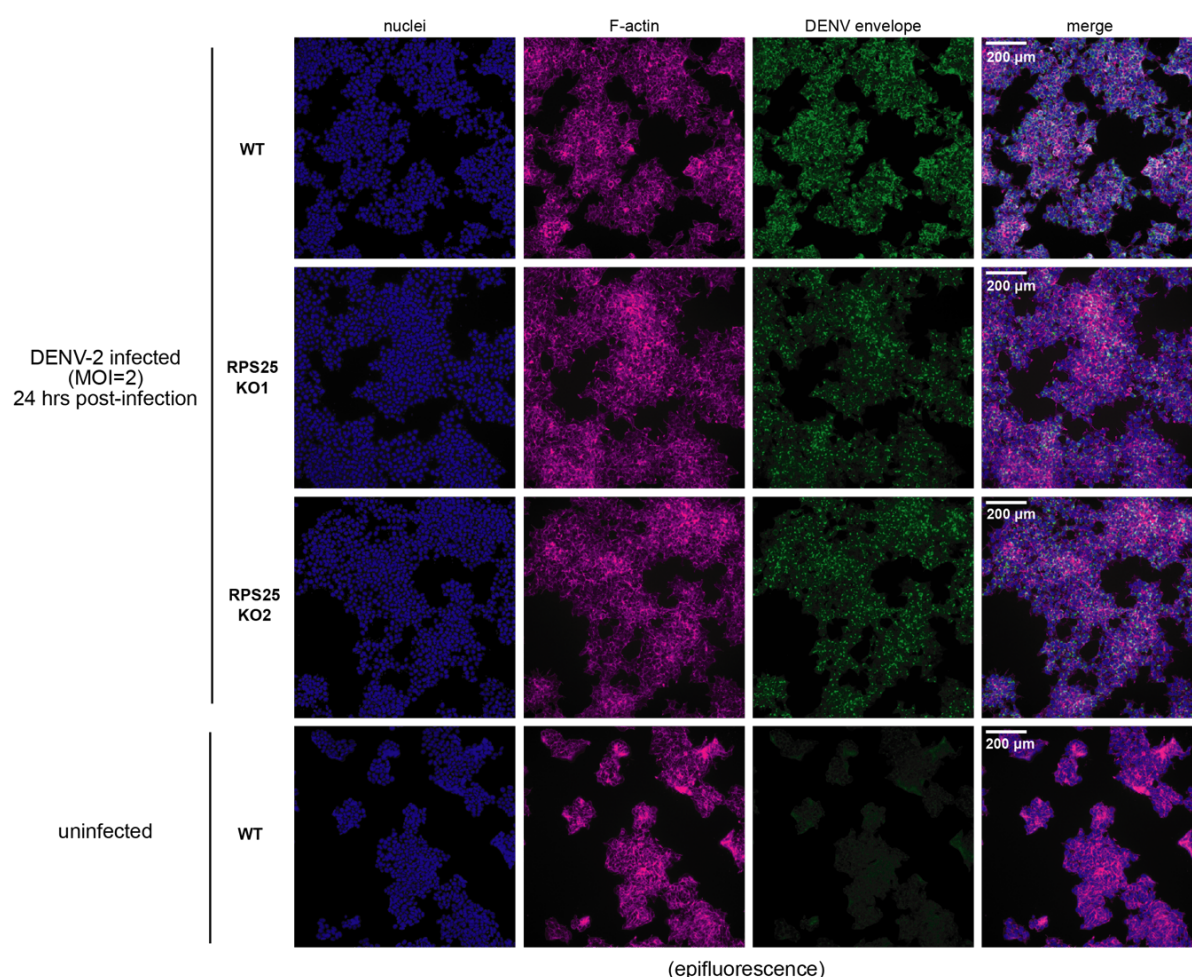


Figure 5—Figure Supplement 2. Epi-fluorescent imaging of fixed WT and RPS25 KO HAP1 cells for the DENV envelope protein following infection with DENV-2 at MOI=2. Same samples as in Figure 5C and Figure 5—Figure Supplement 1C, showing widefield images so as to demonstrate the trend for staining across many cells. The uninfected control (bottom) is included to demonstrate the specificity of the antibody.

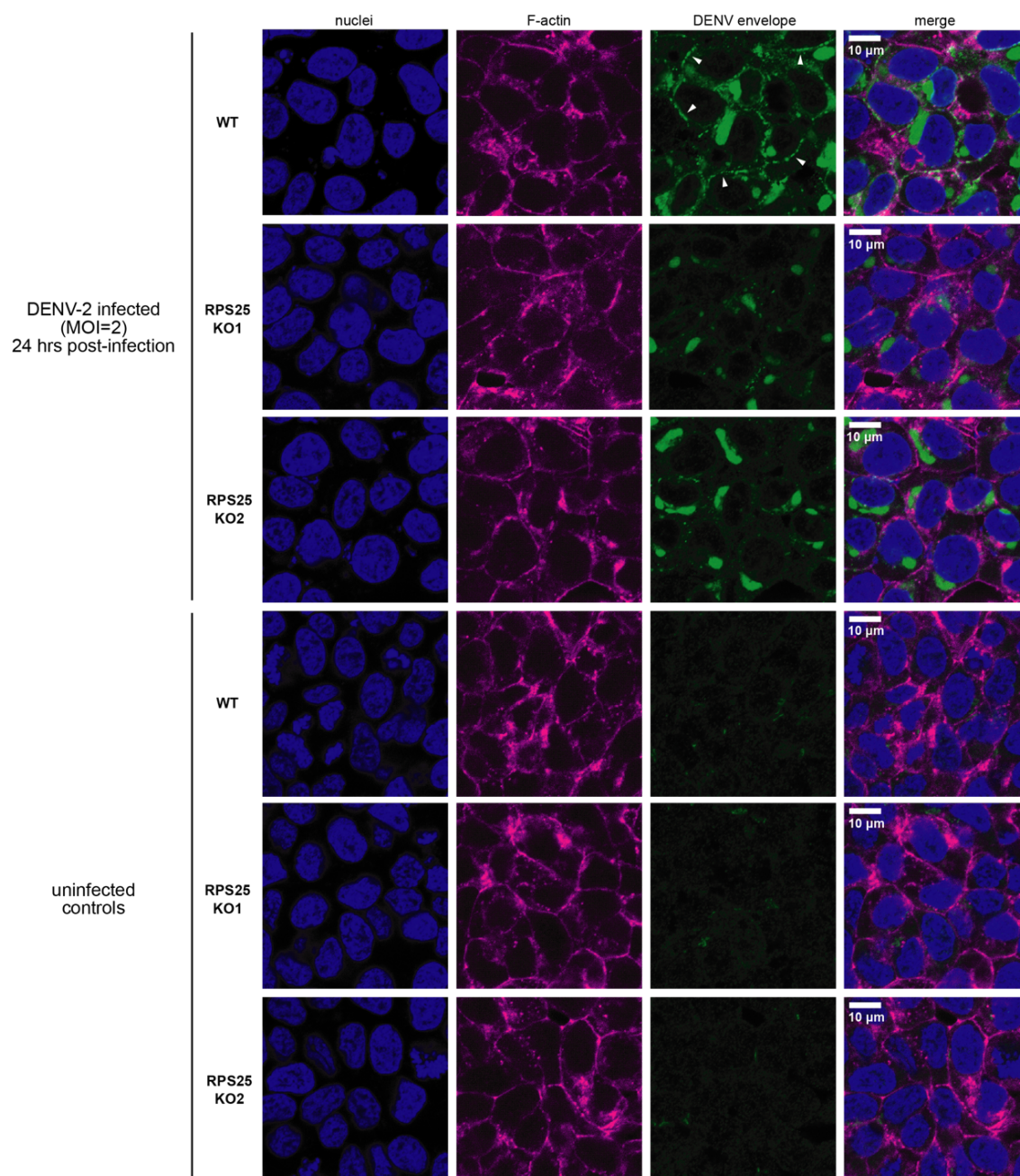


Figure 5—Figure Supplement 3. Additional confocal images of fixed HAP1 cells with IF staining for the envelope protein following DENV-2 infection, as in Figure 5C and Figure 5—Supplementary Figure 1. Both infected (MOI=2) and uninfected cells are shown to demonstrate the specificity of the antibody, and white arrows point to bead like structures in WT cells.

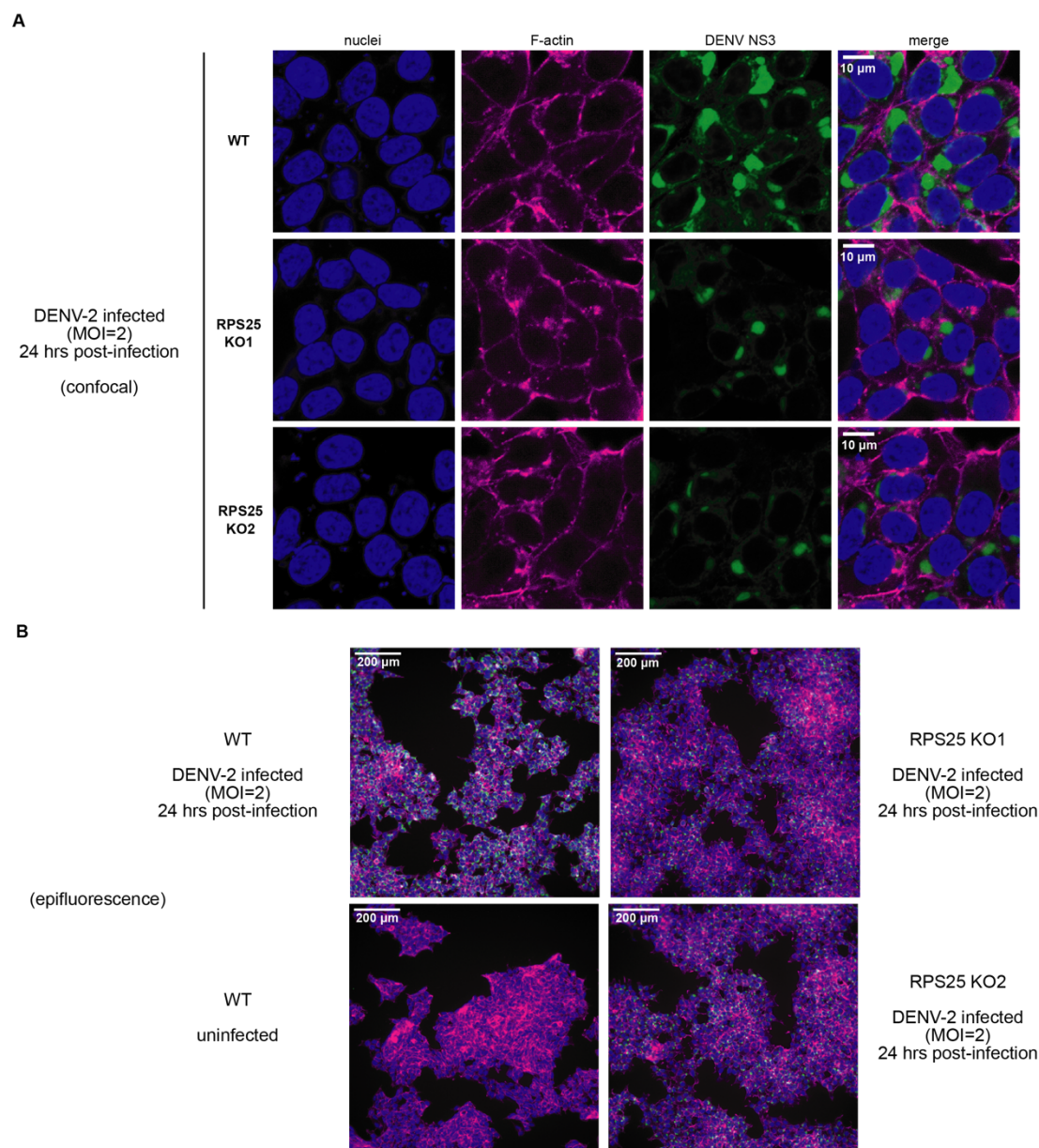


Figure 5—Figure Supplement 4. IF imaging of DENV-2 infected HAP1 cells (MOI=2) for the DENV NS3 protein. Fixed cells were stained with an antibody against the DENV NS3 protein alongside staining of nuclei with Hoescht and F-actin with Phalloidin 660. Unlike the staining for the DENV E protein, bead like structures are not observed at the cell periphery. **A.** Confocal images of DENV-2 infected WT and RPS25 KO HAP1 cells. **B.** Epifluorescent imaging of DENV-2 infected and uninfected HAP1 cells. Merged widefield images included alongside uninfected WT control to demonstrate specificity of NS3 staining. Nuclei, F-actin, and NS3 staining are colored the same as in (A).

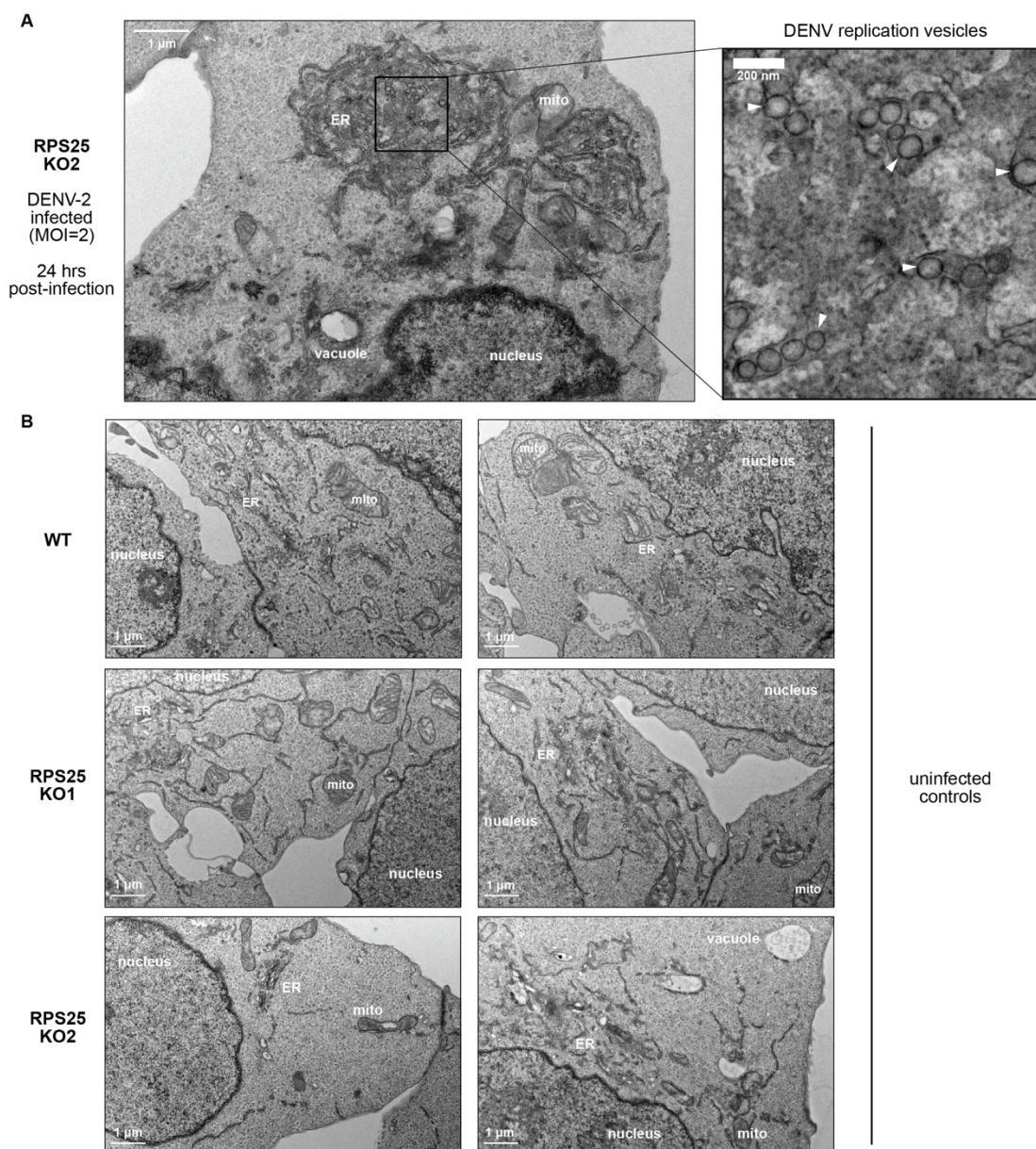


Figure 5—Figure Supplement 5. Transmission electron microscopy of WT and RPS25 KO HAP1 cells. **A.** A fixed and embedded cell slice from infection of RPS25 KO2 HAP1 cells with DENV-2 at MOI=2. As in Figure 5D, white arrows point to the appearance of ER membrane-derived replication vesicles within the inset on the right. **B.** Example cell slices from uninfected WT and RPS25 KO HAP1 cells, wherein no replication vesicle-like structures are observed.

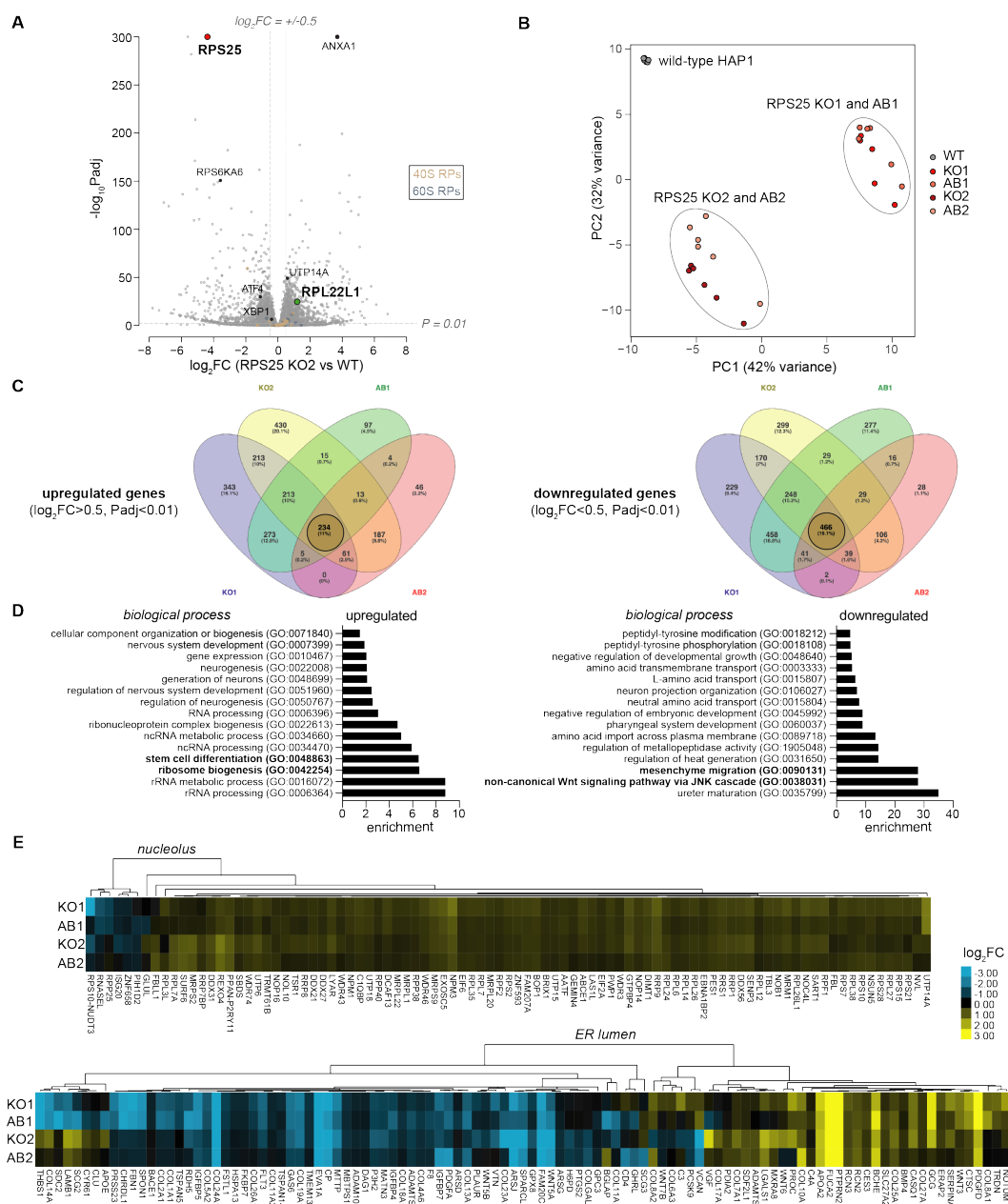


Figure 6—Figure Supplement 1. RNA-seq of WT, RPS25 KO, and e25-HA AB cells demonstrates a shared transcriptional response from RPS25 loss. **A.** Volcano plot of significant fold-changes between RPS25 KO2 and WT HAP1 cells as in Figure 6A. **B.** Principal component analysis (PCA) of all samples from DESEQ2. Each bubble represents a biological replicate with n=6 per cell line. The percent variance for each principal component is indicated in the axis label. **C.** Venn diagrams for the shared fold-changes ($\log_2FC < -0.5$ or > 0.5 , $P_{adj} < 0.01$) of both the RPS25 KOs and ABs ($\log_2FC < -0.5$ or > 0.5 , $P_{adj} < 0.01$). Plot is similar to Figure 6B, but without proportional scaling. Shared genes for all conditions were used for ontology analysis. **D.** GO analysis showing fold enrichment for upregulated and downregulated genes as in Figure 6C, but based on searching against Biological Process GOs. The top 15 GOs are shown (all with FDR-corrected P-value < 0.05). **E.** Heatmaps from hierarchical clustering of \log_2FC s for each condition by genes within the nucleolus gene ontology (GO:0042254) and ER lumen gene ontology (GO:0005788). Only genes with $\log_2FC > 0.5$ in at least two conditions are shown.

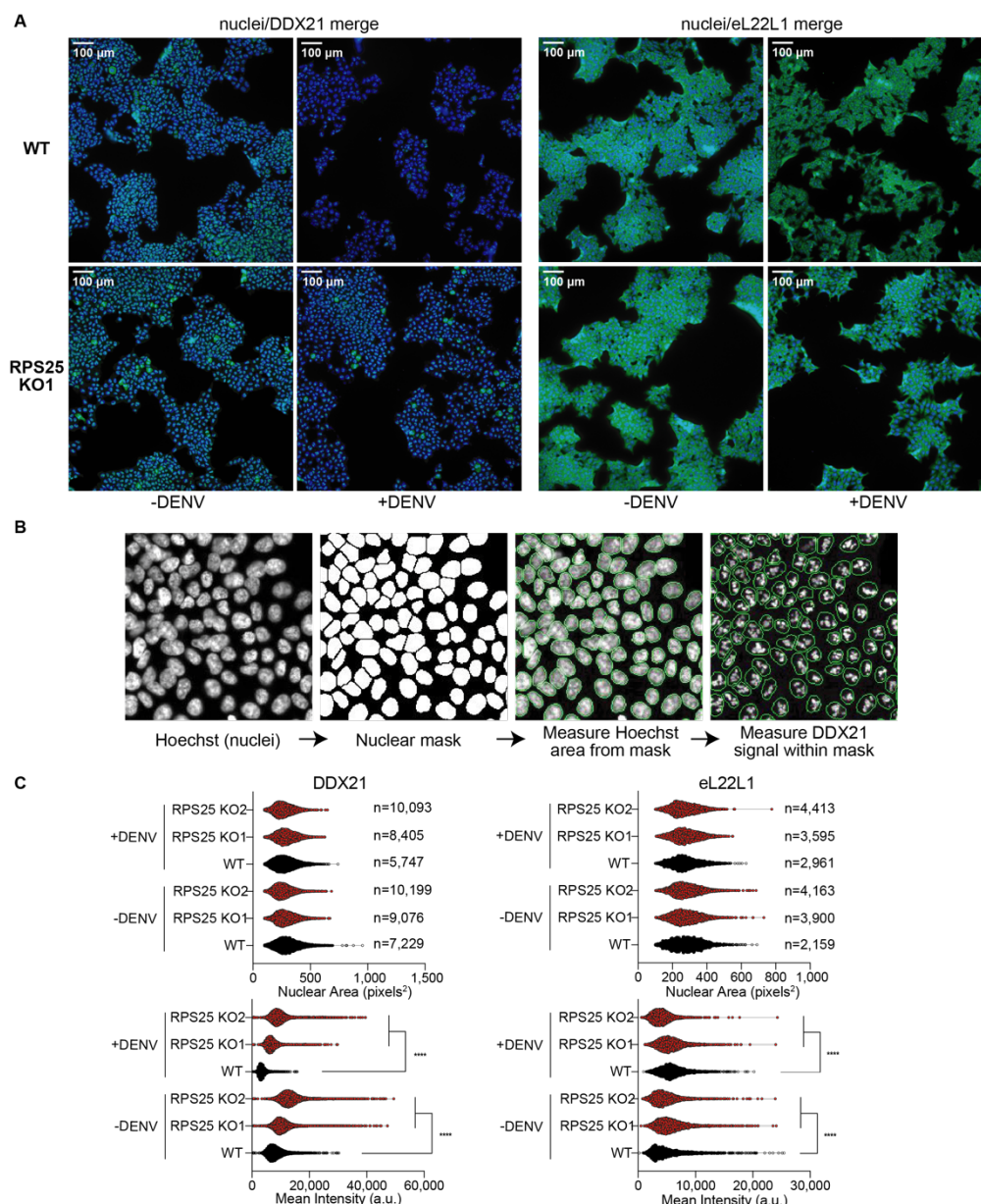


Figure 6—Figure Supplement 2. Quantitative image analysis of WT and RPS25 KO for nucleolar markers. **A.** Example IF images of WT and RPS25 KO cell lines stained for the nucleolar proteins DDX21 and eL22L1. Images are as in Figure 3—Figure S2, only including images from epi-fluorescent imaging, which were the ones used for analysis. Representative images are from WT and RPS25 KO1 HAP1 cell lines with or without (+/-) DENV at MOI=2, fixed and stained 24 hours post-infection. **B.** Example of automated nuclear boundary identification for use in image analysis in (D). Images are from viewfields of WT cells stained for Hoescht and DDX21 as in (A). **C.** Violin plots depicting parameters from image analysis of cell nuclei with antibody markers. DDX21 (left) and eL22L1 (right) mean intensity values (bottom panels) were determined by measurements from within nuclear regions (upper panels). For each cell line, the number of cells analyzed (n) is indicated next to bars in top upper panels. Statistical significance represents the results of a two-way ANOVA for each cell line and condition (-/+ DENV), correcting for multiple comparisons with a Tukey test. P-value: <0.0001 (****).

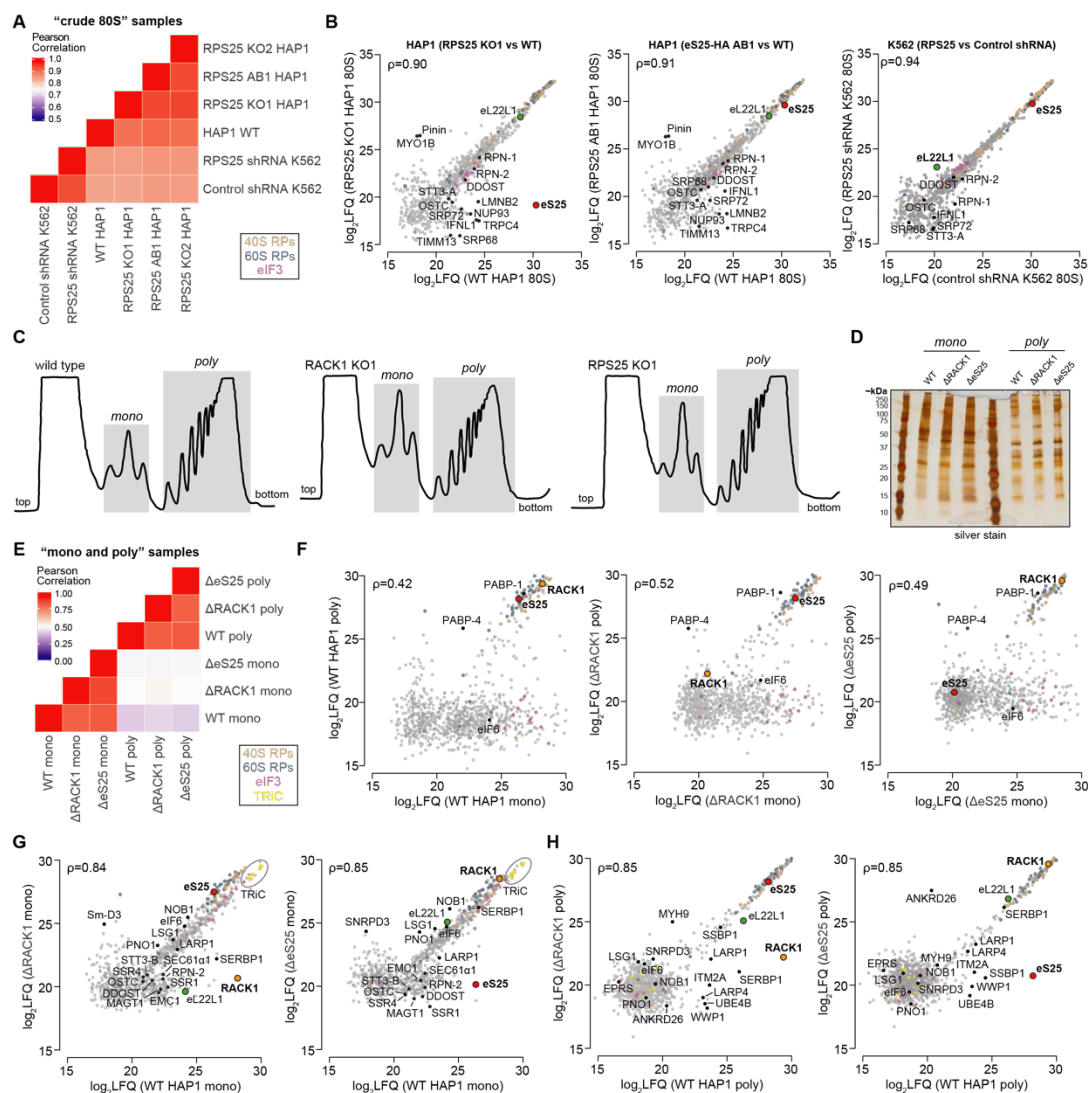


Figure 7—Figure Supplement 1. Mass spectrometry of eS25- and RACK1-deficient "crude 80S" ribosomes, monosome, and polysome samples. **A.** Heatmap of Pearson correlation coefficients (ρ) for \log_2 LFQ intensities from each HAP1 or K562 "crude 80S" ribosome sample. **B.** Plot of \log_2 LFQ intensities of crude 80S ribosomal samples. RPs and eukaryotic initiation factor 3 (eIF3) subunits are colored as indicated and select ribosomal and non-ribosomal proteins are annotated. A clear elevation of eL22L1 in the HAP1 RPS25 KO crude 80S was not observed here, possibly due to the differing complexity of these versus other ribosome samples. **C.** Example polysome profiles of WT, RACK1 KO, and RPS25 KO HAP1 cells that were used for isolating monosomes ("mono") and polysomes ("poly") for mass spectrometry. Post-nuclear lysate was sedimented in 10-60% sucrose gradients, the height of peaks is proportional to absorbance at 254 nm, and the top and bottom of gradients are indicated. Mono and poly were isolated from fractions under respective gray highlighted regions for two polysome profiles for each cell line. **D.** Silver stain of SDS-PAGE gel with equal amounts (2.5 μ g) of each mono and poly sample. **E.** Heatmap of Pearson correlation coefficients (ρ) for each HAP1 or K562 "crude 80S" ribosome sample. **F.** Plot of \log_2 LFQ intensities of "poly" versus "mono" samples from WT and mutant cells. RPs and eIF3 subunits are colored as indicated and select ribosomal and non-ribosomal proteins are annotated. **G.** Plot of \log_2 LFQ intensities of mutant versus WT "mono" and "poly" samples. RPs, eIF3 subunits, and TRiC chaperonin complex subunits are colored as indicated. Select ribosomal and non-ribosomal proteins are annotated.

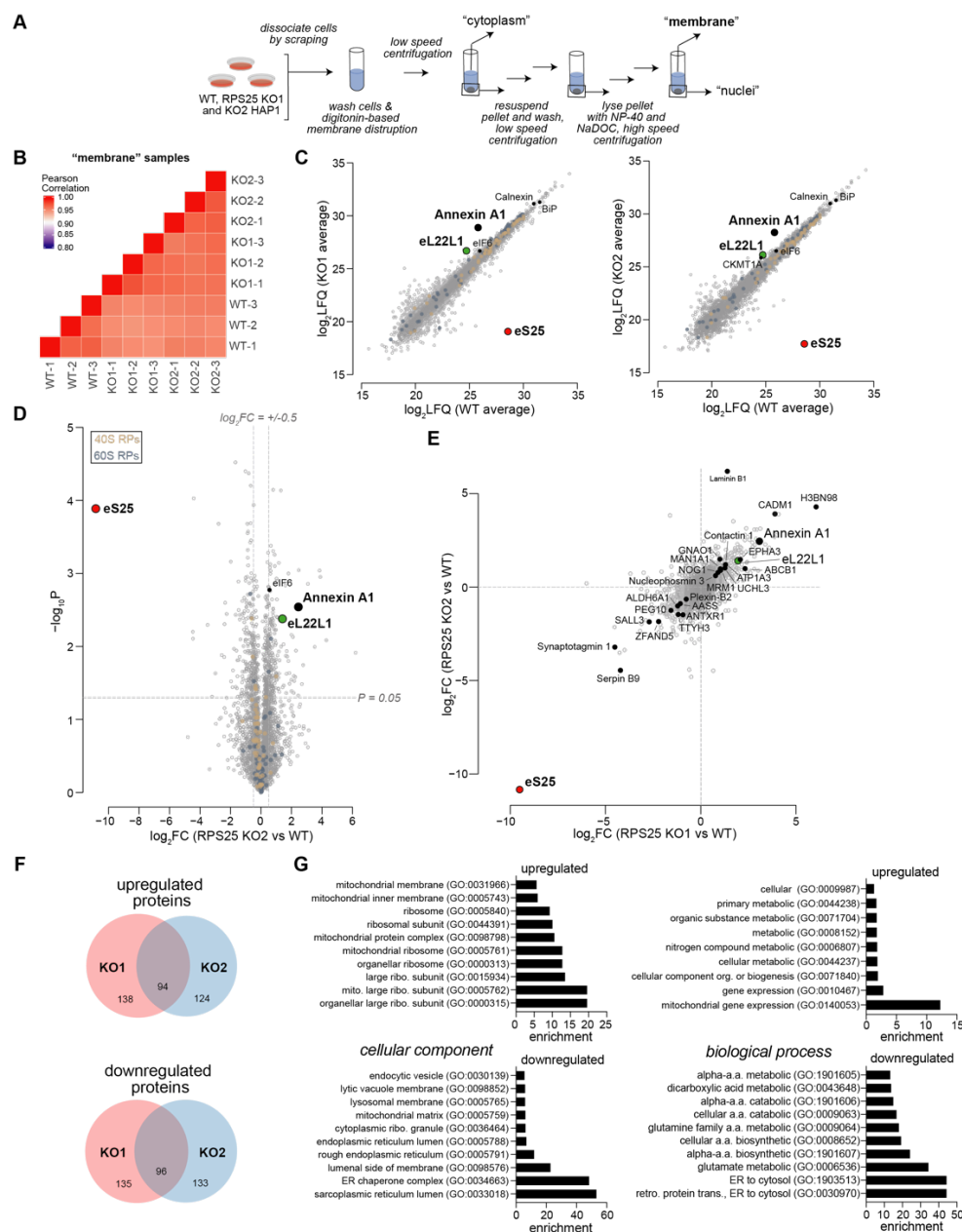


Figure 7—Figure Supplement 2. Membrane mass spectrometry of WT and RPS25 KO HAP1 cells. **A.** Schematic for purification of the “membrane” fraction from WT and RPS25 KO HAP1 cell lines. The membrane fraction as indicated was subsequently used for mass spectrometry analysis. **B.** Heatmap of Pearson correlation coefficients (p) for \log_2 LQ intensities from each membrane sample. **C.** Average \log_2 LQ values for RPS25 KO1 and KO2 versus WT membranes. Plot demonstrates the enrichment of ER proteins such as Calnexin and BiP in addition to other notable alterations. **D.** Volcano plot for significant fold-changes from LFQ intensities of membrane fractions. Plot as in Figure 7A. **E.** Common shared significant fold-changes for RPS25 KO1 and KO2 versus WT. Select ribosomal and non-ribosomal proteins are annotated. **F.** Venn diagrams of upregulated and downregulated membrane proteins for RPS25 KO1 and KO2 versus WT samples. Proteins with \log_2 FC<-0.5 and >0.5, and $P<0.05$ were compared for KO1 and KO2 versus WT. **G.** Ontology analysis of changing membranes proteins with \log_2 FC <-0.5 and >0.5, and $P<0.05$. Analysis from cellular component (left) and biological process (right) ontology categories is shown. Fold-enrichment is shown for each ontology, selecting the top 10 (or less) with FDR-corrected P -values<0.05.

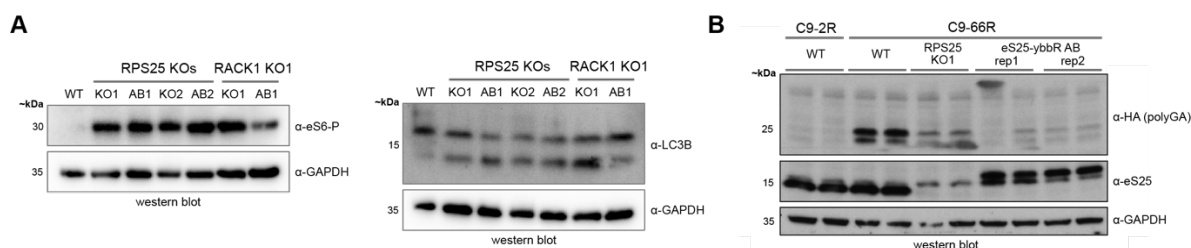


Figure 7—Figure Supplement 3. Western blot analyses of WT, RPS25 KO, RACK1 KO, and respective AB cells for markers related to phenotypes of the RPS25 KO. **A.** Western blots of WT, KO, and AB HAP1 cell lines for eS6 phosphorylation and LC3B lipidation. Blots were performed with the same whole cell lysate samples used in Figure 7C. **B.** Western blots of WT, RPS25 KO1, and KO1 (eS25-ybbR AB) transfected with RAN translation constructs encoding different numbers of C9orf72 (GGGGCC) repeats (C9-2R and C9-66R: 2 and 66 repeats, respectively). Technical duplicates were run in side-by-side lanes and two transfection replicates (rep1 and rep2) of the eS25-ybbR AB are shown. In these blots, the eS25 antibody detects a likely non-specific band in all samples that migrates above the expected eS25 molecular weight (MW). There is also a higher MW band detected in the first technical replicate of the eS25-ybbR AB rep1 that arose for unknown reasons. Note that the eS25-ybbR AB construct was used instead of the eS25-HA AB construct due to interference of the eS25-HA tag with that of the HA-tagged polyGA. The HA antibody used here is from Cell Signaling, the GAPDH antibody for (A) is from Genetex (GAPDH-HRP), while the GAPDH antibody used for (B) is from Sigma.

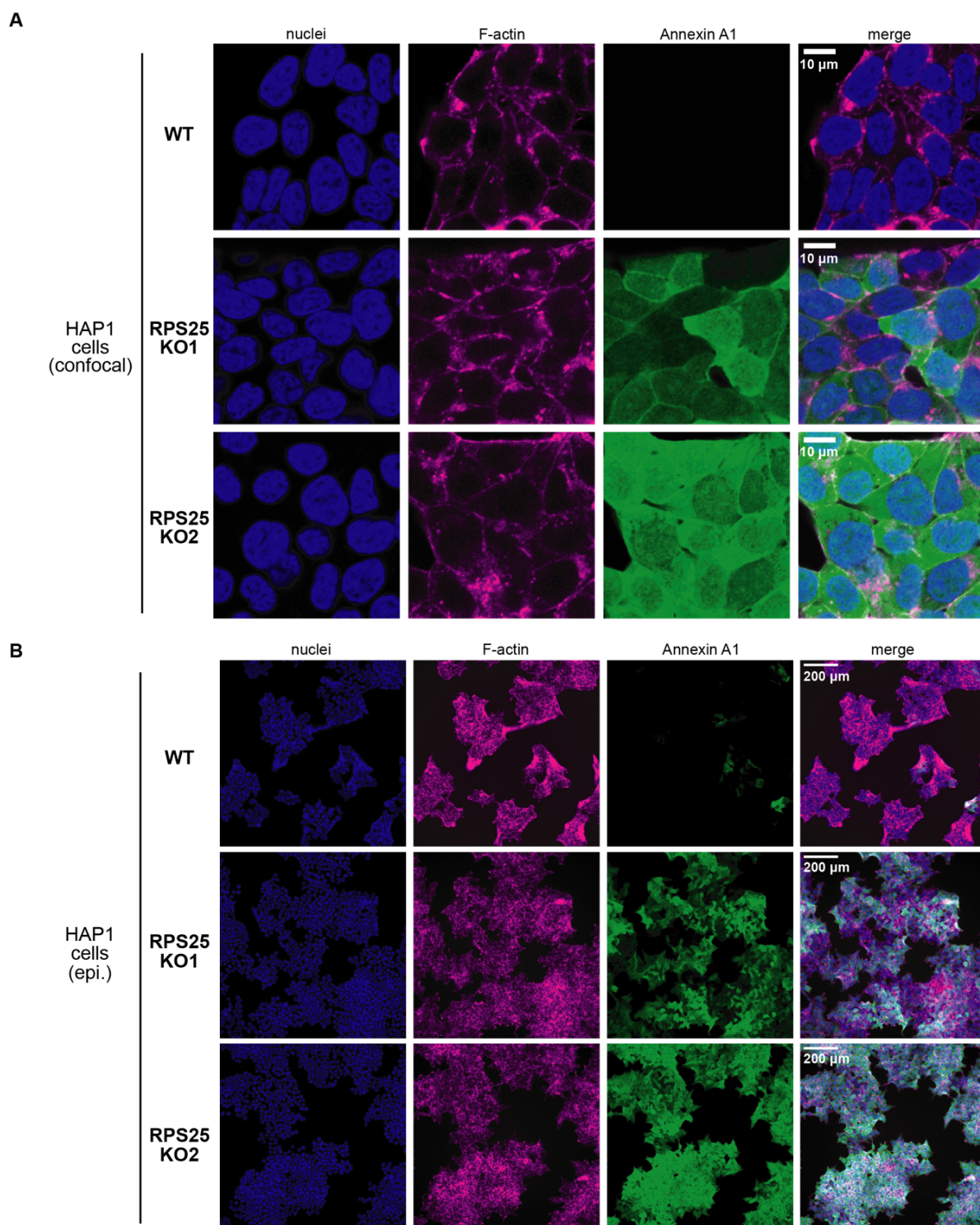


Figure 7—Figure Supplement 4. Immunofluorescent imaging of WT and RPS25 KO cells for Annexin A1. **A.** Confocal images of fixed WT and RPS25 KO HAP1 cells for Annexin A1 alongside staining of nuclei with Hoescht and F-actin with Phalloidin 660. **B.** Epi-fluorescent imaging of WT and RPS25 KO HAP1 cells to demonstrate widefield images of the same samples imaged by confocal microscopy in (A) and Figure 7D.

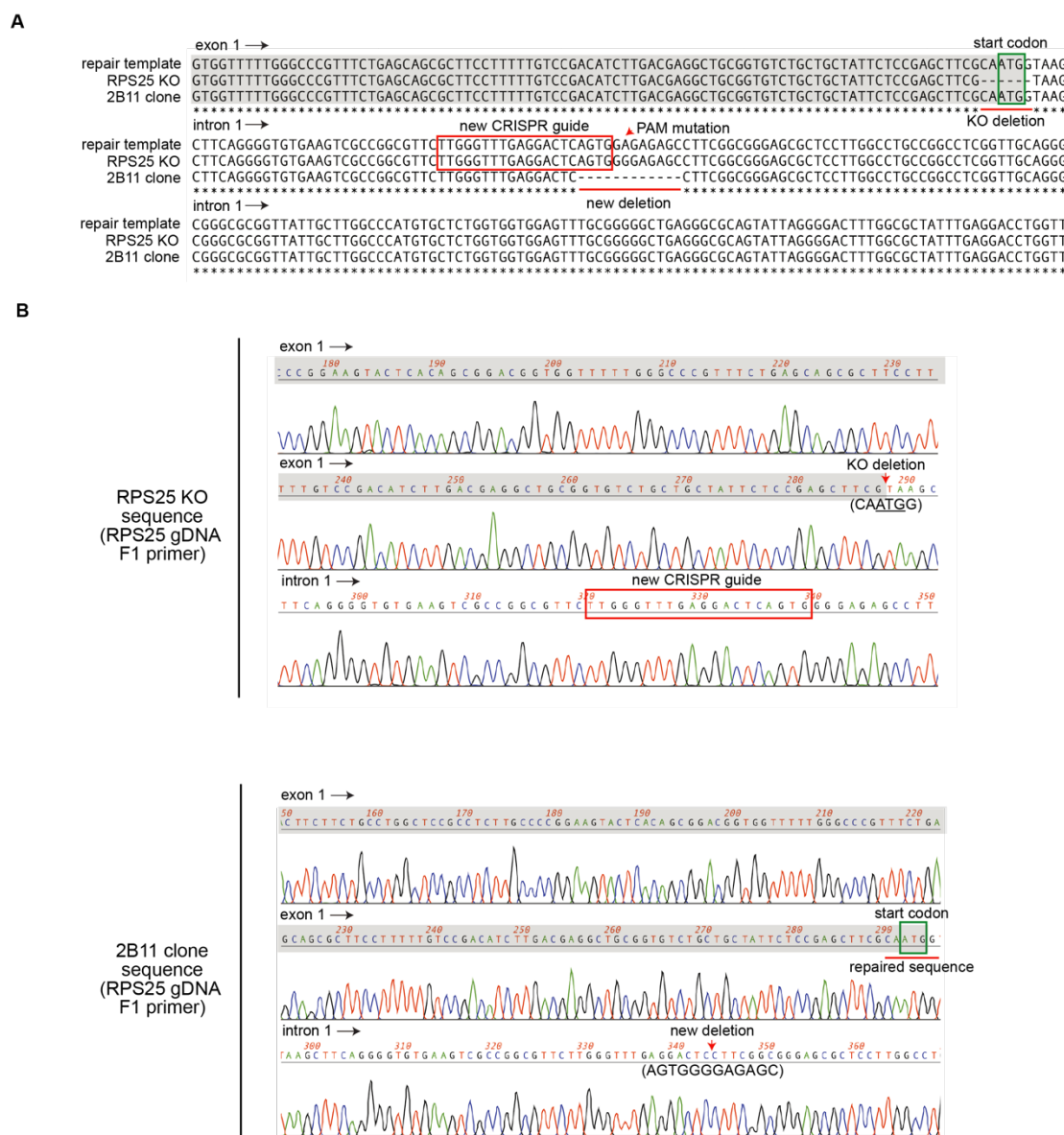


Figure 8—Figure Supplement 1. Homology-directed repair of the RPS25 KO1 genomic locus and sequence validation of the first repair clone HDR1 (2B11). **A.** Sequence alignment of a region of the designed repair template with that of the of the RPS25 KO1 genomic sequence and the sequence of the HDR1 (2B11) clone. Alignment is annotated to show the exon (gray highlight) and intron (no highlight) as well as the start codon (green box) at the site of the original CRISPR/Cas9 deletion. **B.** Sequence chromatograms from sequencing the RPS25 KO1 cell line (top) and the RPS25 HDR repair cell line 2B11 (bottom). Sequences are from priming an amplified genomic DNA fragment with the RPS25 gDNA F1 primer, which initiates upstream at the 5' end of the RPS25 genomic locus. Regions of interest are annotated for both chromatograms to indicate modified sites in the context of the exon and intron sequences.

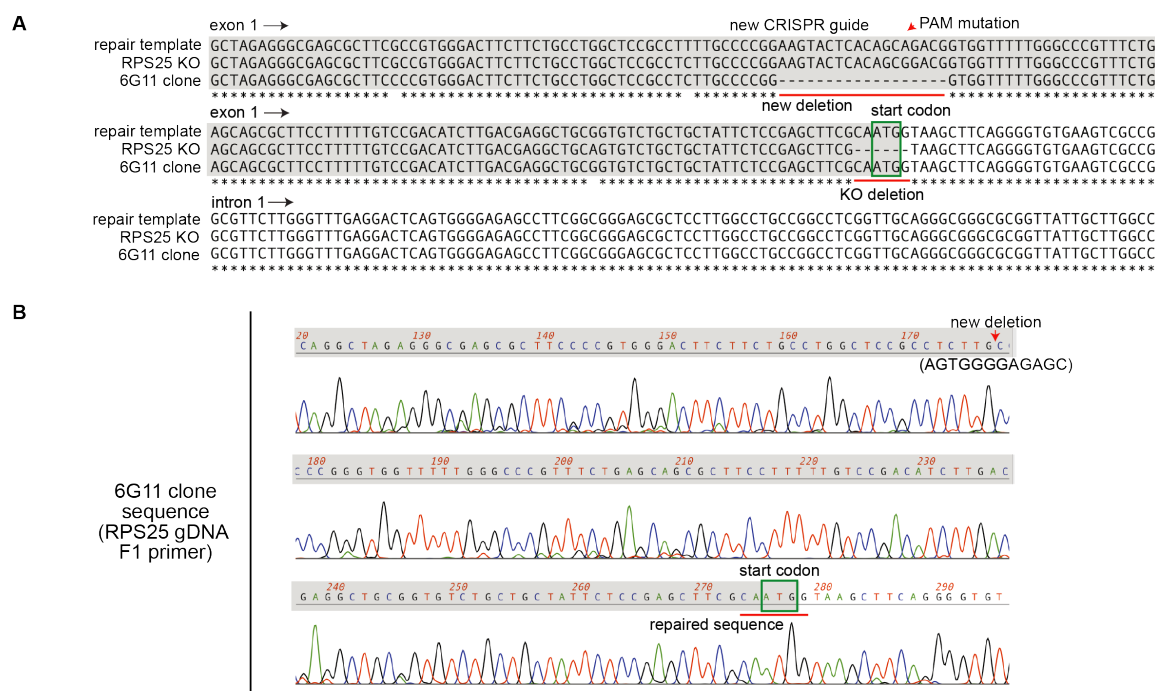


Figure 8—Figure Supplement 2. Homology-directed genome repair of the RPS25 KO1 genomic locus and sequence validation of the second repair clone HDR2 (6G11). **A.** Sequence alignment of a region of the designed repair template with that of the RPS25 KO1 genomic sequence and the sequence of the HDR2 (6G11) clone. Alignment is annotated to show the exon (gray highlight) and intron (no highlight) as well as the start codon (green box) at the site of the original CRISPR/Cas9 deletion. **B.** Sequence chromatograms from sequencing the RPS25 KO1 cell line (top) and the RPS25 HDR repair cell line 6G11 (bottom). Sequences are from priming an amplified genomic DNA fragment with the RPS25 gDNA F1 primer, which initiates upstream at the 5' end of the RPS25 genomic locus. Regions of interest are annotated for both chromatograms to indicate modified sites in the context of the exon and intron sequences.